Politecnico di Milano

SCHOOL OF INDUSTRIAL AND INFORMATION ENGINEERING

Master of Science – Energy Engineering

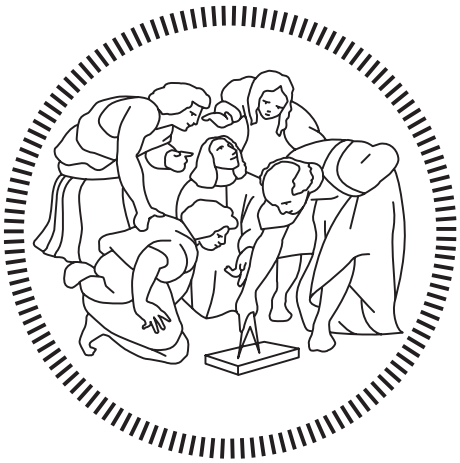

Synthesis and characterization of manganese dioxide cathodes for Zn-ion batteries

Supervisor

Prof. Benedetto Bozzini

Co-Supervisor

Francesca Rossi

Candidate

A. Safa OKŞAŞ - 915862

Academic Year 2020 – 2021

“Our true mentor is science.”

M. Kemal Atatürk

Acknowledgements

There are a number of people without whom this thesis might not have been written, and to whom I want to express my sincere gratitude. First, I wish to express my appreciation to my supervisor, Prof. Benedetto Bozzini, for all his help. This work may not have been completed successfully without the continued guidance I received from him. It has simply been an honor to work and learn from his knowledge. I also owe many thanks to my co-supervisor Francesca Rossi who helped me to learn all the new techniques and concepts in the lab that I needed to finish my project.

I must also thank Prof. Marco Boniardi from the Dept. of Mechanics of Politecnico di Milano for FESEM and XRD analyses, Prof. Claudio Mele from the Department of Innovation Engineering of the University of Salento for his Micro-Raman measurements, and Dr. Emanuele Marini from ZSW Ulm, for help with the synthesis of active material (crpytomelane) and related slurries.

And last, but not least, I have to thank my loving parents, Hakan and Ayşenur, for all the support they have provided me with throughout the years, both emotionally and financially. I could not have done the great things I have done or seen the world as I have without you both. I could not have completed this work without the love and support of my girlfriend, Gloria, thanks for the caring and patience during these nine months of intensive study and work. Many thanks are also owed to my friends: those who have been with me for years, and those I have made all over Europe in the past two years. I hope to maintain contact and meet you all again somewhere. Without you, I might have graduated a year sooner.

Sommario

Le batterie Zn/MnO_2 ad elettrolita acquoso, neutro o alcalino, stanno vivendo negli ultimi decenni un rinnovato interesse a causa dei loro componenti sicuri, facilmente reperibili e sostenibili. In particolare, i catodi a base di biossido di manganese (MnO_2) risultano essere promettenti nell'ambito della tecnologia agli ioni di zinco grazie alla loro elevata capacità teorica e alla loro presunta capacità di intercalare lo ione zinco in maniera analoga ai catodi delle batterie agli ioni di litio. Tuttavia, essi mostrano ancora oggi un notevole degrado nelle prestazioni dopo aver subito prolungati cicli di carica e scarica e non possono essere sfruttati in una produzione su larga scala.

Questa tesi tratta di due importanti aspetti legati ai catodi a base MnO_2: in primo luogo si parlerà della sintesi del biossido di manganese, ottenuto tramite un processo idrotermico a microonde e un processo elettrochimico; in seguito si tratterà della caratterizzazione strutturale ed elettrochimica del catalizzatore sintetizzato.

Nella prima sezione della tesi si tratterà della sintesi di strati sottili di MnO_2 tramite elettrodeposizione, sfruttando la voltammetria ciclica. Nella fase iniziale del lavoro sono stati riprodotti diversi esperimenti di letteratura per validare il protocollo di elettrodeposizione; successivamente sono stati cambiati sia i parametri di elettrodeposizione sia le composizioni delle soluzioni elettrolitiche per studiare il ruolo di diversi cationi nel dibattuto processo di intercalazione. Data la mancanza di letteratura specifica sull'argomento, sono stati presi come riferimento degli esperimenti svolti in ambiente acido con un elettrodo di platino. Dopo aver caratterizzato elettroanaliticamente i processi di elettrodeposizione e di intercalazione, i film di biossido di manganese elettrodepositato potenziostaticamente hanno subito vari cicli di carica e scarica, in presenza o meno di Zn^{2+}, per verificare le loro prestazioni in condizioni applicative. Le misure nella cella a tre elettrodi sono state infine confrontate con i test svolti in una split-cell, confermando la reversibilità dell'intercalazione dello ione zinco; inoltre, è stata verificata anche la buona stabilità dell'elettrodo a base di MnO_2 in ambiente neutro.

Nella seconda parte della tesi sono state studiate le prestazioni di un elettrodo a base di criptomelano (α-MnO_2) sintetizzato tramite un processo idrotermico. L'evoluzione morfologica e strutturale del catalizzatore è stata studiata usando la diffrazione ai raggi X (XRD), la spettroscopia Raman e la microscopia elettronica a scansione (SEM-EDS). Dato che il criptomelano è un materiale sfruttato anche nei catodi per le batterie zinco-aria, la caratterizzazione elettrochimica è stata svolta sia in ambiente alcalino che neutro, ma in assenza di ossigeno dato che l'obiettivo di questa tesi è studiare il catalizzatore nell'ambito dei catodi ad intercalazione per tecnologie Zn-ione.

Abstract

The chemistry of rechargeable aqueous Zn/MnO_2 batteries in a neutral or mildly acidic electrolyte has drawn great attention recently due to the fact that all of the components of a Zn/MnO_2 battery are safe, abundant, and sustainable. MnO_2-based cathodes are promising for zin ion battery (ZIB) applications due to their high theoretical capacity and voltage. However, they suffer from severe capacity fading after prolonged charge-discharge cycles, and the reaction mechanism of the MnO_2 cathode remains a topic of discussion. This thesis concerns two important subject matters: synthesis of manganese dioxide catalyst with the micro-wave-assisted hydrothermal method and electrodeposition methods, followed by electrochemical characterization of the synthesized active manganese-based material by various electrochemical and structural analysis.

The first section of this thesis examined the basic electrodeposition mechanism of MnO_2 films on different electrodes using the cyclic voltammetry technique, beginning by reproducing previously published experiments and then varying the chemical composition of aqueous electrodeposition solutions to provide meaning for the potential role of cations in the intercalation mechanisms. In the following section, we conducted a systematic exploration of a subset of the electrodeposition parameter space in order to lay the groundwork for our next work on the effect of Zn^{2+} in neutral electrolytes. Due to the scarcity of electroanalytic work in neutral electrolytes, work in an acidic environment at a Pt electrode was chosen as a benchmark case. Finally, we conducted cycling tests in the operating potential range to determine the effect of Zn^{2+} on the electrochemical behavior of MnO_x-based ZIB cathodes. We specifically carried out battery-like tests in electrolytes without and with added Zn^{2+}, for MnO_x films electrodeposited potentiostaticaly from the electrolytes. To confirm the importance of $MnSO_4$ and $ZnSO_4$ co-presence in the electrolyte, we performed split-cell experiments in 0.1 M Na_2SO_4 and 1 M $ZnSO_4$ neutral solutions. Finally, birnessite-type MnO_2 films appear to be a viable cathode material for ZIB applications, as they exhibit reversible Zn^{2+} intercalation and good stability in a moderate $ZnSO_4$ aqueous electrolyte containing a $MnSO_4$ additive that inhibits irreversible cathode deactivation.

In the second part of this work, we examine the electrochemical performance of drop-cast α-MnO_2 electrodes, prepared by the hydrothermal method. We explored the structural and morphological evolution of α-MnO_2 electrodes in detail using XRD, Raman spectroscopy, and SEM-EDS mapping. This material is commonly used for ZAB cathodes, thus we investigated cyclic voltammetry tests in KOH solution, which is typically used for electrocatalytic ORR tests, but here in the absence of O_2, as is the case in ZIBs. Then, we also conducted cycle voltammetry measurements in the operating potential range in various near neutral solutions, as in the previous section, to examine electrochemical behavior of α-MnO_2 for ZIB applications. In the end, cycling behavior of hydrothermally produced cryptomelane-type α-MnO_2 is better in Zn solutions as compared to Zn-alone solutions, but rapid capacity loss is still observed in both cases.

Extended Abstract

One of the primary advancements needed for present-day technology advancement is electrical energy storage, the most promising approach to which is electrochemical energy storage (EES), based on rechargeable batteries [1, 2]. In fact, we can easily appreciate the significant role batteries are playing in modern life and in our daily life. Taking a look into recent history, among other key influences, the 2007 release of the iPhone permitted the extensive technological and cultural changes we are currently seeing. But only decades of developments in battery technology made this viable.

When it comes to future impact, we can anticipate how future battery advancements and economies of scale will aid in the reduction of CO2 emissions in transportation. Battery-powered vehicles may be able to replace internal combustion engines in the transportation sector as EES technology advances. Although some are concerned about the use of coal in these electric vehicles, improved batteries can actually integrate environmental benefits by effectively storing energy and thus aid in the transition to renewables to replace coal and other fossil-fuel based energy plants.

Despite the emphasis on Li-ion rechargeable batteries, more attention has been paid to the investigation of other promising EES systems. Aqueous zinc ion batteries (ZIBs) are particularly appealing because of the intrinsic benefits of Zn metal among "beyond lithium-ion" battery techniques:

- Low cost due to natural abundance and large production.
- Nontoxic and easy processing.
- High volumetric energy density (5851 mAh cm^{-3}).
- High stability and compatibility in aqueous electrolytes.
- Two-electron redox properties offer a high theoretical anode capacity.

The MSs Thesis is devoted to synthesis and characterization of manganese dioxide cathodes for Zn-ion batteries. Methodology, goals and results of each Chapter are briefly listed below.

Chapter 1 A theoretical description of batteries and their inner electrochemical processes is presented, followed by an insight into the ZIB, and finally the use of manganese di oxide as an active cathode material in these batteries with their advantages and disadvantages, as well as their Zn ion storage mechanisms, electrochemical performance, current issues, and modification strategies.

- Despite the material's low specific capacity and poor cycle performance, Kang et al. discovered the intercalation and deintercalation properties of Zn2+ ions in aqueous ZIBs using MnO2 as the cathode material. This proposed intercalation mechanism sparked numerous studies to create new types of electrode materials and electrolytes, as well as to improve the electrochemical performance of ZIB applications.
- ZIBs have an inner structure similar to rechargeable metal ion batteries, with Zn metal as the anode, Zn-intercalating materials as the cathode, and neutral or slightly acidic Zn-

containing solutions as the electrolyte. Because of its low redox potential (-0.76 V vs. SHE) and high overpotential for hydrogen evolution, metallic zinc is unique in aqueous electrolytes. Furthermore, metallic Zn has a theoretical capacity of 820 mA h g-1, which is greater than the capacity of aqueous electrolyte-compatible intercalation type anode materials. The working principle and storage mechanisms of ZIBs differ depending on different polymorphic phases of manganese-based cathodes, which is the primary focus of this thesis.

- α-MnO_2 has received the most attention among the numerous polymorphs. α-MnO_2 can provide a high specific capacity (more than 200 mA h g^{-1}) with a low discharge voltage (around 1.3 V vs Zn/Zn^+) by taking advantage of the structural advantage. α-MnO_2, on the other hand, frequently exhibits rapid capacity fading during cycling and poor high-rate performance. The complex Zn^{2+} ion storage mechanism is another difficult issue with the -MnO2 cathode. To date, four reaction mechanisms have been proposed: Zn2+ ion insertion/extraction, H^+ and Zn^{2+} co-insertion, chemical conversion reaction, and dissolution-deposition mechanisms.
- The epsilon polymorph of manganese dioxide (ε-MnO_2) is an intergrowth of pyrolusite and ramsdellite domains. A dense packing of the MnO_6 octahedra in ε-MnO_2 makes it unfavorable for the fast metal ion intercalation/deintercalation in the energy storage process. This cathode material can be synthesized through potentiostatic electrodeposition process in the 1 M $ZnSO_4$ + 1 M $MnSO_4$ electrolyte.
- Birnessite (δ -MnO_2) is a poorly crystallized form of manganese dioxide with a two-dimensional layered structure formed by edge-sharing MnO6 octahedra, generally with hydrated cations (e.g., Na^+, K^+, Ca^{2+}, Zn^{2+}) in the interlayers compensating for the small overall negative charge. Birnessite-type compounds readily undergo cation-exchange reactions due to their very open structure, resulting in a high adsorption capacity for heavy metal cations. Furthermore, because of their microporous nature and/or an irregular stacking of these layers, birnessite-type compounds readily participate in oxidation–reduction reactions.

Chapter 2 Experimental methodology is presented. Relevant experimental procedures are briefly explained: potentiostatic technique, linear sweep voltammetry, cyclic voltammetry, galvanostatic technique, Raman spectroscopy, X-ray diffraction and scanning electron microscopy. Testing and fabricating protocols are reported in details: preparation of the cathodes by electrodeposition, hydrothermal synthesis of α-MnO_2, and preparation of drop cast and spray coated electrodes. The full list of specifics for each tested and mentioned sample is reported.

Chapter 3 An in-depth analysis of anodic electrodeposition of manganese dioxide (MnO_2) on CP, Platinum, and glassy carbon electrodes is presented, as well as ex-situ measurements provided by other researchers in the field. The effect of electrode material on the adhesion and electrocatalytic activity of the resulting MnO_2 thin films is investigated. The mechanism of the formation of MnO_2 thin films on a working electrode has been widely discussed, several mechanisms have been proposed, but it is difficult to define one single route because it is influenced by different factors such as the ion concentration, pH and deposition techniques.

Platinum electrode was used as a substrate for MnO_2 electrodeposition before investigating the electrochemical behavior of MnO_2 in conjunction with intercalation Zinc ions: a process that has been rather accurately described in the literature in the case of highly acidic electrolytes. It could be observed whether acid strength has a discernible effect on both oxidation and reduction of manganese. Due to water oxidation, there was significantly more anodic charge passed than cathodic charge on all the voltammograms. The charge ratio increased when both Zn^{2+} and H^+ ions were added into the 0.1 M $MnSO_4$ solution separately. This is indicating that each ion has

a similar impact on the charge ratio even if the electrodeposition mechanism is different for both cases. The presence of Zn^{2+} ions inhibit anodic charge in the acidic electrolyte, while there is an opposite situation in the neutral electrolyte. In the following section, the CV results are examined from the carbon paper electrodes. Following conclusions can be listed after comparing findings to those of previous studies:

- If CV is the first one after electrochemical deposition, the anodic/cathodic charge decrease with each cycle.
- Both anodic and cathodic charges tend to stabilize in the sequent CVs.
- In every cycle studied so far, the cathodic charge is greater than the anodic charge.

While the electrodeposited MnO_x is discharged at cathodic sweep, the reduction of managanese allows the coinsertion of H^+ and Zn^{2+} ions through the deposited MnO_2. This sequential redox reaction increases reproducibility in a split cell, which is quite faster to be reached than in three electrode cell setup applications.

The effect of cell setup and different electrolyte concentrations on capacity fading during cycling is investigated in the following section. Capacity has tendency to decrease approximately 5 percent per cycle in the mixed $MnSO_4$:$ZnSO_4$ electrolyte. However, capacity fade increases up to 10 percent per cycle in the $ZnSO_4$-only solution. Together, these findings support the view that presence of Mn2+ ions in the electrolyte change the equilibrium of reducing Mn^{2+} ions from the MnO_2 electrode, and thus prevent continuous Mn^{2+} dissolution.

In the last section, electrochemical activity of micro-wave synthesized α-MnO_2 (cryptomelane), which is drop cast on glassy carbon substrate as described in Chapter 2, is investigated by using cyclic voltammetry in alkaline and near neutral electrolytes. We observed that the anodic and cathodic current averages are quite high in Na^+-alone solution, and the voltammogram has a more rectangular shape which is the same trend observed on the measurements applied on the electrodeposited MnO_2 samples in Na^+-alone solution.

Using XRD, Raman, and SEM-EDS mapping, we investigated the structural and morphological evolution of α-MnO_2 electrodes in depth. The XRD pattern of pristine spray coated sample is perfectly indexed into the cryptomelane-type α-MnO_2 (JCPDS: 44-0141). FESEM was used to image the surface of the α-MnO_2 film, which had been spray-coated onto carbon paper, both in its pristine state and after electrochemical treatments in Na_2SO_4 and $ZnSO_4$/Na_2SO_4 solutions. The EDS results highlight the potential of the Na^+ intercalation/deintercalation mechanism, but more research is needed to better understand it. After adding Zn^{2+} to Na^+ solution, the patterns of flaky/platelet phase were observed when the reduction potential alone was applied, as well as when the reduction and oxidation potentials were applied sequentially. This flaky/platelet porous substance is linked to the formation of ZHS, which contains Zn as well as a high proportion of S. This new phase is highly irreversible, as evidenced by the fact that it remains detectable after successive polarizations at 0.1 and 0.9 V. Ex-situ Raman analysis were acquired in order to better understand the nature of the cryptomelane-like manganese dioxide film, spray-coated onto carbon paper, after electrochemical and/or ion-exchange reactions. The same batch of spray coated samples prepared for SEM, were also investigated through Raman microscopy. The features in Raman spectrum of pristine sample can attributed to the tunnel cation K^+ intercalated in α-MnO_2. Furthermore, after polarizing first at 0.1 V then at 0.9V in Na_2SO_4 solution, there are slight changes in Raman spectra, denoting that potential switch might have triggered structural change from α-Mn_2O_3 to γ-Mn_2O_3. The electrodeposited carbon papers in different solutions are also investigated through Raman microscopy. After introducing Zn^{2+} into Mn^{2+} solution, a new pattern is most closely associated with a coexistence of $ZnMn_2O_4$ nanoparticles and birnessite type δ-MnO_2.

Chapter 4 – Section 1

The electrochemistry of MnO_x is varied and complex, particularly in the near-neutral aqueous solutions relevant to ZIBs, and is strongly dependent on the crystal structure, the details of the electrolyte composition, the solubility of Mn species, and the surface conditions, and conducting a critical and exhaustive review of the available literature would be a monumental task. Nonetheless, certain fundamental and ubiquitous aspects of MnO_x electrochemistry lend themselves to a simple sequence of redox reactions involving progressive valence changes. To address this issue concretely, we will refer to the particular case of cyclic voltammetry during the electrodeposition of birnessite (δ-MnO_2). We referred to this particular set of experimental data in the following discussion because it embodies the complexity and logic of MnO_x redox, but we will modify and generalize the interpretation presented in this paper in order to provide a sufficiently broad platform for discussion of electrochemical measurements, particularly voltammetric measurements. It is worth noting at this point that the redox scenario we will discuss is compatible with the Pourbaix diagram for Mn in aqueous systems, but contains additional information, most notably regarding the redox of mixed-valent oxides. Finally, it is important to note that, since most of the electrochemical reactions involving Mn-species include exchanges of protons, in the absence of buffering agents, potential-dependent changes in pH is an important point that ought to be address explicitly in future work on neutral electrolytes.

Additionally, as Larabi et al. emphasize, the presence of untransformed birnessite Mn_7O_{13} and groutite α-MnOOH in films exposed to anodic polarizations where MnO_2 is the stable form indicates that slow kinetics may result in the retention of out-of-equilibrium phases in MnO_x films subjected to electrochemical polarization. O_2 saturation of $Mn(II)_{aq}$ solutions does not modify the voltammetric pattern, but has been reported to lead to complete oxidation of MnOOH formed at C1 back to Mn(IV).

A large number of studies have been published regarding the electrodeposition of MnO_2 in strong acidic sulphate media, owing to the interest of the preparation of electrochemical manganese dioxide (EMD) for alkaline battery cathodes and supercapacitors. Apart from details, that can be retrieved e.g. in [Clarke 06], the key point with strongly acidic solutions is that Mn(III) is soluble and readily disproportionate according to the scheme: $2Mn(III)_{aq} \rightarrow Mn(II)_{aq} + Mn(IV)_{solid}$. This mechanism is suitable for alkaline battery cathodes and supercapacitors, but more complex structures, possibly containing a fraction of Mn(III), enabled by neutral solutions, may be more suitable for intercalating or electrocatalytic Mn compounds, which are of interest for ZIB and ZAB applications, respectively.

Work on the electrochemistry of MnO_x in alkaline aqueous ambient has main focussed on γ-MnO2, owing to its interest for commercial alkaline batteries. Several classical papers have addressed the reduction reaction mechanisms, highlighting strong dependence on operating conditions, such as: c.d., additives and oxide. More recently, renewed interest in secondary alkaline batteries has also brought back into the spotlight mechanistic issues regarding the reoxidation of MnO2 reduction products in alkaline electolytes. Despite the complexity of the scenario, when all details are considered, and following the line of reasoning discussed previously, it is still possible to rationalize the redox of MnO_x in an alkaline environment using a reasonably broad class of simple processes. In general, two types of reactions occur during the reduction of γ-MnO2: I a homogeneous solid-solution reaction that results in the continuous voltage variation characteristic of intercalation processes without phase changes; and (ii) a heterogeneous, multi-phase reaction that results in a characteristic voltage plateau.

We investigated the interaction of Zn with redox processes of MnO_x in alkaline and near neutral solutions. Hetaerolite ZnMn2O4 has been reported to form as an irreversible phase at the cathode of alkaline batteries. This side product is the result of the chemical reaction between

$Zn(OH)_4^{2-}$ and MnOOH: the anodic and cathodic reactions products, respectively. $ZnMn_2O_4$ is highly resistive and notably electrochemically inert, thus impairing the recharge process.

In near neural solutions, the most commonly reported mechanism is reversible Zn ion intercalation/deintercalation, which involves a reversible phase transition from tunnel-structured -MnO_2 to layer-structured Zn-birnessite, spinel $ZnMn_2O_4$, or layered Zn-buserite. A layer-type MnO_2(δ-MnO_2), where Zn^{2+} can intercalate into the structure, showing different structural evolution patterns because of the diversity of δ-MnO_2 phases (e.g chalcophanite, birnessite, buserite, and vernadite), which results in joint incorporation of cations and water molecules within the interlayer. For example, spinel-type $ZnMn_2^{3+}O_4$ was observed when nano-flake δ-MnO_2 was used in an aqueous electrolyte, while a reversible variation of MnO_2/$ZnMnO_2$ was observed for hydrated δ-MnO_2 in a non-aqueous solution. At variance with this approach, Sun et al. proposed H^+ and Zn^{2+} cointercalation in akhtenskite-structure MnO_2 (ε -MnO_2). The consecutive formation of the MnOOH and $ZnMn^2O^4$ strongly promotes this mechanism of insertion of H^+ followed by Zn^{2+}. In addition to redox-related intercalation and phase transition, an accompanying precipitation process was recognized, which leads to the formation of inactive $Zn_4(OH)_6(SO_4)\cdot 5H_2O$ (ZHS) on the surface of α-MnO_2, that could be removed by rinsing. On the contrary, a new study revisited the effect of ZHS formation, proposing a complex reversible dissolution-deposition mechanism that contributes to capacity.

At the end of first subsection, we wish to emphasize that the above-reported mechanistic considerations are mainly based on integral electrochemical measurements and thermodynamic calculations, complemented by a limited number of ex situ structural studies. Needless to say that notably more insight could be achieve by in situ measurements, sensitive to chemical state and structure.

Chapter 4 – Section 2

In ZIBs, as well as, to some extent in ZABs, the redox of MnO_x occurs in the presence of Zn^{2+} solution species. In view of gaining fundamental understanding of this process, this section addresses the role of the interaction of Zn^{2+} with birnessite, δ-MnO_2 films, electrochemically grown onto glassy carbon by voltammetric cycling in a potential range encompassing the Mn(II)-Mn(IV) redox.

Our interpretation of voltammetric features is based on the overview of Section 1, the key results of which are summarized. As a calibration run, and in order to address the potential role of Na^+ intercalation, we repeated the experiments of Larabi-Gruet et al., under nominally identical conditions, but increasing the number of voltammetric cycles, in order to attain a proved steady-state condition. The chemical composition of the electrodeposition solution greatly affects the electrodeposition process of MnO_2 films. H^+-intercalation process of features is energetically more favoured and less extensive reduction of the electrodeposit to Mn(II) takes place in electrolytes with added Na^+. In addition, full oxidation of the film requires higher potentials in Na^+-free electrolyte, possibly owing to the progressive growth of poorly conducting material. When Zn^{2+} was added to the Mn^{2+} solution, significant changes in the electrochemical behavior of Mn occurred during electrodeposition. The CVs do not tend to diminish, and the anodic and cathodic charges consumed are quite equivalent. This situation is consistent with Zn^{2+} intercalation/deintercalation without the formation of layers that would tend to inhibit the process.

Since electroanalytic work in neutral electrolytes are limited, work in an acidic environment at a Pt electrode was set as a benchmark before the further investigation of Zn^{2+} effects. First, the influence of pH on both the initiation of Mn^{2+} oxidation and subsequent redox processes is fully consistent with thermodynamics. Our CV results are similar in many respects those from previous studies accomplished by Larabi et al. The presence of Zn^{2+} has a negligible effect on

the reduction of MnO_2 at both ambient and elevated temperatures, indicating that H^+ intercalation is the process controlling. The effect of Zn^{2+} has been also observed on the initial stage of MnO_x electrodeposition on Pt electrode. Furthermore, the electrode material has a distinct impact on the initial stages of MnO_x electrodeposition. In comparison to a glassy carbon electrode, platinum has a higher electrocatalytic activity in a neutral electrolyte, promoting the oxidation of Mn^{2+}.

We conducted cycling tests in the operating potential range to determine the effect of Na+ and Zn2+ on the electrochemical behavior of MnOx-based ZIB cathodes. While the CV patterns measured in Na^+ solutions yields pseudocapacitive behaviour, the ones in Zn^{2+} solutions were dominated by distinct an anodic and a cathodic current peak, corresponding to Zn(II) intercalation and deintercalation into and from MnO_2. It appears that some form of regeneration of the MnO_x structure is needed, making use of solution Mn^{2+}, in order to stabilize redox cycling in the presence of Zn^{2+}. This is consistent with the view that more stable cycles could be obtained only if $ZnSO_4$ and $MnSO_4$ are simultaneously present in the solution. Instead, the interaction of the MnO_x film solution Zn^{2+}-alone leads to irreversible transformation correlated with drastic loss of the initial capacity. In the case of δ-MnO_2, the anodic processes are suppressed after the first cathodic-going scan. Owing to the specific peak positions found with δ-MnO_2, the ZIB operating range lies a range of limited redox activity.

Though sharing some common aspects, the redox of electrodeposited MnO_x and hydrothermally grown α-MnO_2 undergo different types of processes upon voltammetric cycling in the presence of Zn^{2+}. Electrodeposited MnO_x supports, reversible intercalation of Zn^{2+} if Mn^{2+} is present in the solution, suppressing irreversible modifications leading to cathode deactivation. With α-MnO_2, the cycling behaviour is improved in Zn^{2+}/Mn^{2+} solutions with respect to pure Zn^{2+} ones, but rapid capacity loss occurs in any case.

Table of Content

List of Figures

List of Tables

Chapter 1 Introduction

One of the primary advancements needed for present-day technology advancement is electrical energy storage, the most promising approach to which is electrochemical energy storage (EES), based on rechargeable batteries [1], [2]. In fact, we can easily appreciate the significant role batteries are playing in modern life and in our daily life. Taking a look into recent history, among other key influences, the 2007 release of the iPhone permitted the extensive technological and cultural changes we are currently seeing. But only decades of developments in battery technology made this viable.

When it comes to future impact, we can foresee how future battery advances and economies of scale will help to reduce CO_2 emissions in transportation. Technological developments in EES can allow battery-powered vehicles to replace internal combustion engines in the transportation sector. Although coal usage for these electric vehicles is apprehensive [3], improved batteries can in fact integrate the environmental benefits by storing the energy effectively and, therefore help to move towards renewables to substitute for coal and other fossil-fuel based energy plants [4].

Batteries are also quite applicable with off-grid systems thanks to their response times (in seconds) and relatively long discharge time (for hours). Storing the energy through batteries also helps frequency regulation, which balances generation and load in real-time and increases grid reliability [5]. In addition, batteries provide previously stored electricity at peak demand times (load leveling) and alleviate the need for additional power on the grid. In the long term, utilities can save the cost of new substations and transmission lines by reducing the load [6].

Lithium-ion batteries (LIB) have been by far the most attractive and commonly utilized EES systems in recent decades, particularly in the communication and transport sector, benefiting from high gravimetric energy densities, longer cycle life, and lightweight [7]. However, their high cost, safety and environmental problems hinder the implementation of LIBs as large-scale energy storage devices. Highly toxic and flammable organic electrolytes are utilized on LIBs and they also imply further threats regarding possible reactions between electrodes and electrolytes. Furthermore, the cost of LIBs is relatively high, not only due to the price of materials but also to the restrictive cell assembly requirements (rigorously moisture-free manufacturing conditions) [8].

Despite the focus on Li-based rechargeable batteries, more attention has been paid to the study of other promising EES systems. Aqueous zinc ion batteries (ZIBs) are compelling in particular because of the following intrinsic benefits of Zn metal among the "beyond lithium-ion" battery techniques:

- Low cost due to natural abundance and large production.
- Nontoxic and easy processing.
- High volumetric energy density (5851 mAh cm^{-3}) [9].
- High stability and compatibility in aqueous electrolytes.
- Two-electron redox properties offer a high theoretical anode capacity.

Consequently, the aqueous ZIBs with Zn metal as the anode, Zn-intercalating materials as the cathode, and neutral or slightly acidic Zn-containing solutions as the electrolyte, are attractive alternative battery systems for large-scale application. The research on aqueous ZIBs was focused strongly on the investigation of suitable cathode materials and the clarification of their electrochemical mechanisms.

As with LIBs, the gravimetric energy and power density of ZIBs, as well as their cost, are strongly influenced by the cathodic materials. In the development of high-performance ZIBs, designing and manufacturing cathode materials with a large storage capacity, a high discharge potential, and a robust crystal structure with simple insertion and extraction paths has been a significant challenge. Only a few materials have been investigated as viable Zn ion host materials to date, including mainly manganese-based compounds, vanadium-based compounds, Prussian blue and its analogs, and organic redox-active compounds.

In this chapter, a theoretical description of batteries and their inner electrochemical processes is presented, followed by an insight into the ZIB, and then usage of manganese di oxide as an active cathode material in these batteries with their strong points and disadvantages, and their Zn ion storage mechanisms, electrochemical performance, current issues, and modification strategies is deepened.

1.1 Batteries and electrochemical processes

This part summarizes the major aspects of electrochemistry to familiarize the reader with the subject and facilitate their reading of this thesis. The majority of the information comes from [10], [11].

Electrochemistry is the study of reactions that occur when charged particles (ions or electrons) pass through the interface between two phases, often a metallic phase (the electrode) and a conductive solution (the electrolyte). Half-cell is the name given to this metal-solution interface. Half-cell reactions occur at the electrode surface, resulting in an imbalance between the electrode and the solution's electric charges: this imbalance generates a potential difference (the half-cell potential), which is hardly measurable due to the charge transfer occurring very close to the electrode surface and this potential can be detected only by sophisticated in situ techniques.

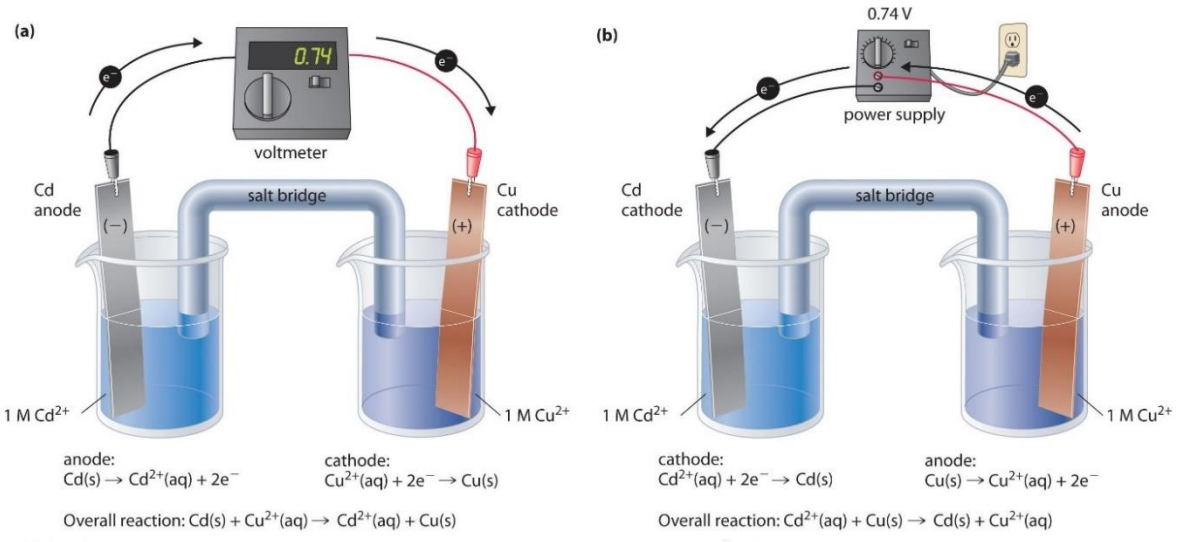

Figure 1.1 Galvanic (a) and Electrolytic (b) Cell

Despite the fact that individual half-cell potentials are not directly measurable, we can still define and operate with them. When two half-cells are connected via an external circuit, the potential difference between them can be measured; this configuration is referred to as an electrochemical cell. When no current is flowing through the cell, the potential difference Eeq is referred to as the cell's open circuit potential (OCP). The two half-cells that comprise the overall cell are referred to as anodic and cathodic electrodes, respectively, on which oxidations (the loss of electrons) and reductions (the acquisition of electrons) occur. Electrochemical cells are classified into two types:

- Galvanic cell (Figure 1.1a): energy released by spontaneous redox reaction is converted to electrical energy. The anode has a negative charge, while the cathode has a positive charge.
- Electrolytic cell (Figure 1.1b): an electrochemical cell in which non-spontaneous redox reactions can be driven by external electrical energy. In this scenario, the anode is positive, and the cathode is negative.

Electrochemical cells, often known as batteries, are devices that convert chemical energy to electrical energy. Batteries are categorized into two categories:

- Primary batteries (non-rechargeable): single-use batteries whose materials undergo irreversible transformation during discharge, converting chemical energy to electrical energy.
- Secondary batteries: rechargeable batteries that can be used for both discharging and charging. Electrical work is performed during charging to supply the free energy required to push the reaction in a non-spontaneous direction. Chemical work is performed when discharging, lowering the available free energy to generate the current required to operate an electrical load.

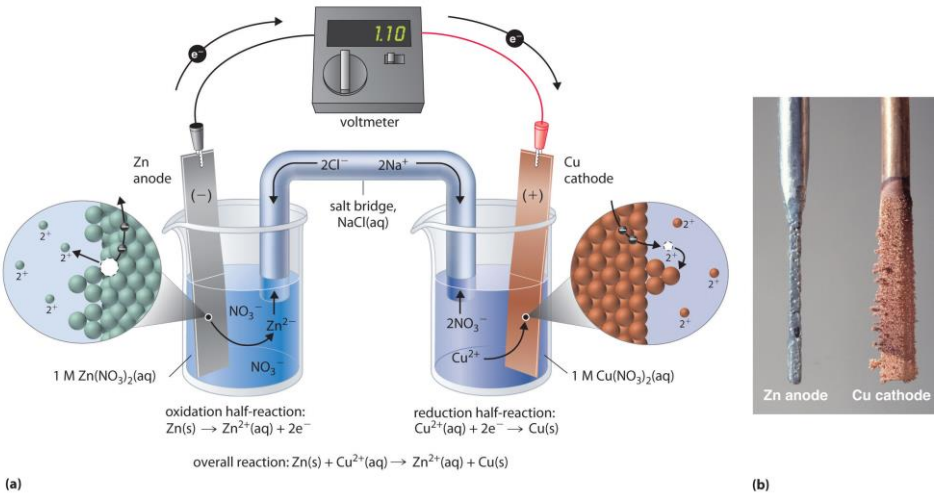

Figure 1.2 (a) A zinc-copper galvanic cell (b) Pictures of Zn anode and Cu cathode.

A typical galvanic cell consists of a zinc strip into a beaker that contains an aqueous 1 M solution of Zn2+ ions, and a copper strip into a different beaker that contains an aqueous 1 M solution of Cu2+ ions (Figure 1.2a). The two metal strips are connected by a wire that allows electricity to flow. When the switch is closed to complete the circuit, electrons will flow from the Zn electrode to the Cu electrode. The reactions (or half-reactions) for both electrodes can be written as follows:

$$Zn(s) \rightarrow Zn^{2+} + 2e^{-} \quad (1.1)$$

$$Cu^{2+} + 2e^{-} \rightarrow Cu(s) \quad (1.2)$$

The oxidation reaction is described by Eq. (1.1), whereas the reduction reaction is given by Eq. (1.2). To ensure that the cell continues to function once the half-cells are connected, the charge carried by the electrons must be compensated for by the movement of ions between the two cells. Thus, if the half-cells are separated, or if there is a single material cell, a salt bridge or a porous membrane must be inserted between the two electrolytes to ensure that the ions have a path to go. As the reaction progresses, the Zn anode loses mass as it dissolves to give Zn^{2+} ions, while Cu cathode gains mass as Cu^{2+} ions are reduced to copper metal that is deposited on the cathode (see Figure 1.2b).

As mentioned earlier, it is difficult to determine the absolute potential difference of a single half-cell. However, we can use the configuration of an electrochemical cell to evaluate its relative potential in relation to a half-cell whose potential is arbitrarily defined as zero: this half-cell is referred to as a reference electrode or standard reference electrode if it is assembled and operating at standard conditions (25 °C, 1 atm). The standard hydrogen electrode (SHE) is universally used for this purpose. It consists of a strip of platinum wire stripped into an aqueous solution containing 1 M H^+. H^+ in solution is in equilibrium with H_2 gas at Pt-solution interface. Protons are reduced or hydrogen molecules are oxidized at the Pt surface based on the following equation:

$$2H^{+}_{(aq)} + 2e^{-} \rightarrow H_{2(g)} \quad (1.3)$$

	Reduction Half-Reaction		E° (V)	
Stronger oxidizing agent	$F_2(g) + 2\,e^-$	$\longrightarrow 2\,F\,(aq)$	2.87	Weaker reducing agent
	$H_2O_2(aq) + 2\,H^+(aq) + 2\,e^-$	$\longrightarrow 2\,H_2O(l)$	1.78	
	$MnO_4^-(aq) + 8\,H^+(aq) + 5\,e^-$	$\longrightarrow Mn^{2+}(aq) + 4\,H_2O(l)$	1.51	
	$Cl_2(g) + 2\,e^-$	$\longrightarrow 2\,Cl^-(aq)$	1.36	
	$Cr_2O_7^{2-}(aq) + 14\,H^+(aq) + 6\,e^-$	$\longrightarrow 2\,Cr^{3+}(aq) + 7\,H_2O(l)$	1.33	
	$O_2(g) + 4\,H^+(aq) + 4\,e^-$	$\longrightarrow 2\,H_2O(l)$	1.23	
	$Br_2(l) + 2\,e^-$	$\longrightarrow 2\,Br^-(aq)$	1.09	
	$Ag^+(aq) + e^-$	$\longrightarrow Ag(s)$	0.80	
	$Fe^{3+}(aq) + e^-$	$\longrightarrow Fe^{2+}(aq)$	0.77	
	$O_2(g) + 2\,H^+(aq) + 2\,e^-$	$\longrightarrow H_2O_2(aq)$	0.70	
	$I_2(s) + 2\,e^-$	$\longrightarrow 2\,I^-(aq)$	0.54	
	$O_2(g) + 2\,H_2O(l) + 4\,e^-$	$\longrightarrow 4\,OH^-(aq)$	0.40	
	$Cu^{2+}(aq) + 2\,e^-$	$\longrightarrow Cu(s)$	0.34	
	$Sn^{4+}(aq) + 2\,e^-$	$\longrightarrow Sn^{2+}(aq)$	0.15	
	$2\,H^+(aq) + 2\,e^-$	$\longrightarrow H_2(g)$	0	
	$Pb^{2+}(aq) + 2e^-$	$\longrightarrow Pb(s)$	−0.13	
	$Ni^{2+}(aq) + 2\,e^-$	$\longrightarrow Ni(s)$	−0.26	
	$Cd^{2+}(aq) + 2\,e^-$	$\longrightarrow Cd(s)$	−0.40	
	$Fe^{2+}(aq) + 2\,e^-$	$\longrightarrow Fe(s)$	−0.45	
	$Zn^{2+}(aq) + 2\,e^-$	$\longrightarrow Zn(s)$	−0.76	
	$2\,H_2O(l) + 2\,e^-$	$\longrightarrow H_2(g) + 2\,OH^-(aq)$	−0.83	
	$Al^{3+}(aq) + 3\,e^-$	$\longrightarrow Al(s)$	−1.66	
	$Mg^{2+}(aq) + 2\,e^-$	$\longrightarrow Mg(s)$	−2.37	
	$Na^+(aq) + e^-$	$\longrightarrow Na(s)$	−2.71	
Weaker oxidizing agent	$Li^+(aq) + e^-$	$\longrightarrow Li(s)$	−3.04	Stronger reducing agent

Figure 1.3 Standard reduction potentials table. Positive potentials indicates that reduction is the spontaneous process; on the contrary, the oxidation is favored process for negative potentials.

Consequently, the SHE provides us the table of the standard reduction potentials or standard half-cell potentials (Figure 1.3):

$$E^{\circ}_{cell} = E^{\circ}_{cathode} - E^{\circ}_{anode} = E^{\circ}_{cathode} - 0 = E^{\circ}_{cathode} \quad (1.4)$$

Where ° indicates the potential at standard conditions. The list of the standard half-potentials are obtained by means of the following cell setup:

$$\mathrm{Pt} \mid \mathrm{H_{2(g)}} \mid \mathrm{H^{+}_{(aq)}} \parallel \mathrm{M^{n+}_{(aq)}} \mid \mathrm{M_{(s)}} \quad (1.5)$$

Due to its difficulty in preparation, the SHE is rarely preferred in electrochemical experiments. Other reference electrodes such as silver-silver chloride and calomel are more commonly used, but their potentials are required to be calibrated periodically against the SHE.

Electrochemical processes proceed thermodynamically according to a decrease in the available free energy. However, the OCP of a cell is also a measure of the cell's tendency to undergo a reaction. Therefore, the Gibbs free energy and the cell potential difference are related as below:

$$\Delta G^{\circ} = -n\,F\,E^{\circ} \quad (1.6)$$

Where F is the Faraday constant and n is the number of electrons has been exchanged. Moreover, starting from Eq.1.6 and considering both standard and non-standard operating conditions, as illustrated in [11], one can obtain the expression for the theoretical cell potential, or Nernst equation, in real temperature and pressure conditions:

$$E = E^{\circ} - \frac{RT}{nF} lnQ \quad (1.7)$$

where R is the universal gas constant and Q represents the reaction quotient (i.e., a function of the activity or concentrations of the chemical species participating in a reaction). Please keep in mind that Eq. 1.7 holds true only under equilibrium conditions.

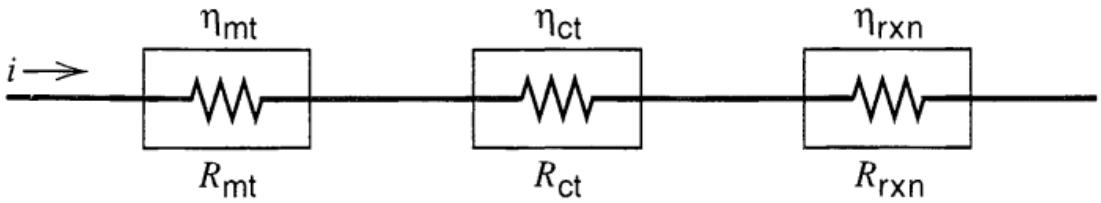

Figure 1.4 Processes in an electrode reaction represented as resistances [11].

According to empirical observation, more energy than Eq. 1.7 is required to maintain a finite rate of cell reactions in an electrolytic cell. The term "overpotential" refers to the potential difference between a thermodynamically determined reduction potential and the experimentally measured reaction potential [10]:

$$\eta = E - E_{eq} \tag{1.8}$$

This energy surplus occurs since the entire electrode reaction is comprised of multiple steps, which contributes as resistances with the related overpotentials. They can be sketched, as shown in Fig. 1.4, as a series of resistances, where η_i is the related overpotential. So, the total overpotential can be also evaluated as the sum of terms associated with the different reaction steps:

$$\eta = E - E_{eq} = \sum_i \eta_i \tag{1.9}$$

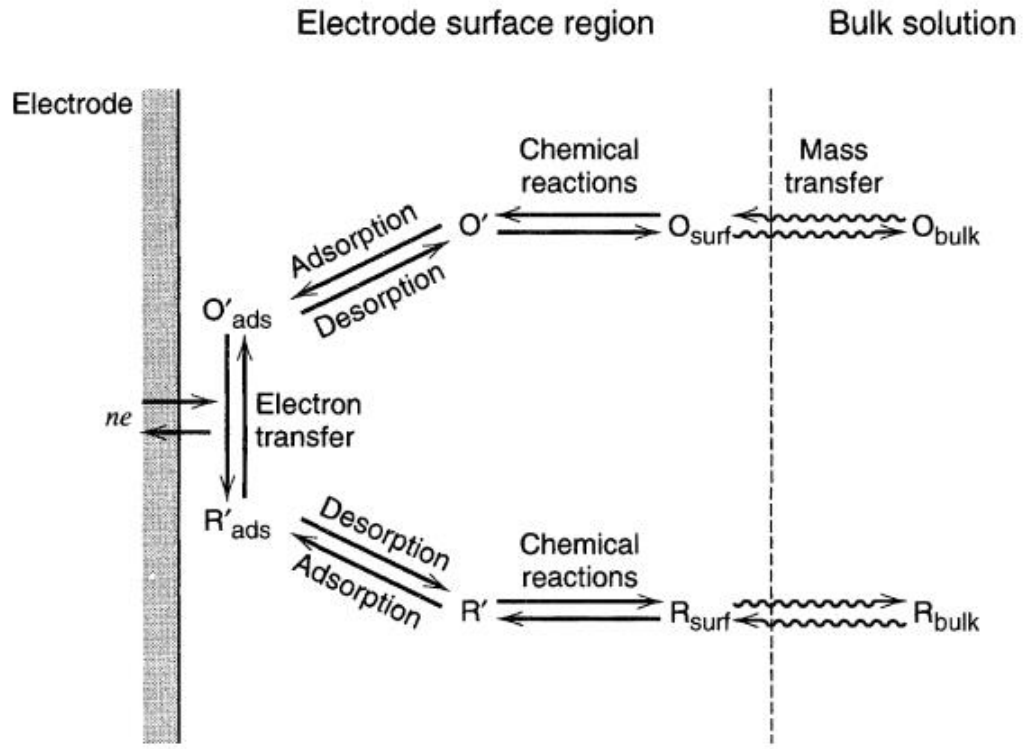

Figure 1.5 A typical electrode reaction's pathway.

In particular, the electrode reaction rate is governed by the rate of processes such as (Figure 1.5):

- Mass transfer.
- Electron transfer at the electron surface
- Chemical reactions that occur before and after the electron transfer.
- Other surface reactions such as adsorption, desorption, or crystallization.

1.2 Introduction to zinc-ion battery

Despite the focus on Li-based rechargeable batteries, more attention has been paid to the study of other promising EES systems. Aqueous rechargeable batteries have gained considerable interest in recent years due to their abundant supply, safety, and environmental friendliness. Additionally, these batteries operate in aqueous electrolytes, which have a higher ionic conductivity and a lower viscosity than organic or solid-state electrolytes. Additionally, the typical mild neutral electrolyte requires little maintenance and requires no additional protection during operation.

Aqueous ZIBs emerged from the previous non-rechargeable alkaline zinc-MnO_2 batteries. The Zn-MnO_2 batteries with neutral electrolytes were proposed and fabricated in 1986. In 2011, Kang's group discovered the intercalation and deintercalation properties of Zn^{2+} ions in aqueous ZIBs using MnO_2 as the cathode material, despite the material's low specific capacity and poor cycle performance [12]. This proposed intercalation mechanism pioneered numerous of research to develop new type of electrode materials and electrolytes and improve electrochemical performance of ZIB applications (see Figure 1.6).

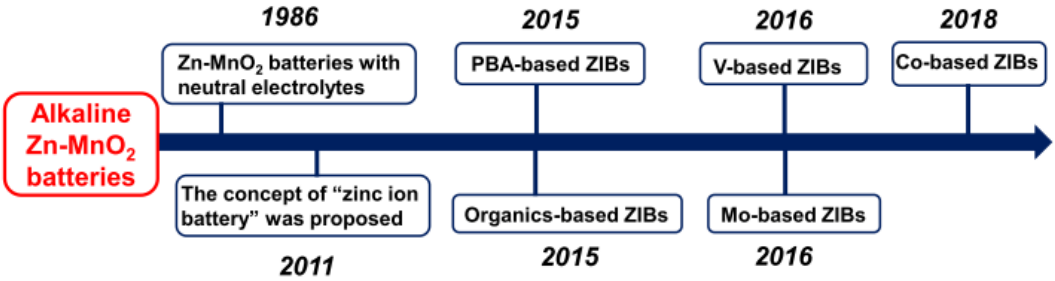

Figure 1.6 A brief history of ZIB's development [13].

1.2.1 Configuration of rechargeable ZIB

Metallic zinc is unique in aqueous electrolytes due to its low redox potential (-0.76 V vs. SHE) and high overpotential for hydrogen evolution. Additionally, metallic Zn has a theoretical capacity of 820 mA h g-1, which is greater than the capacity of intercalation type anode materials suitable for use in aqueous electrolyte. Thus, Zn is a very promising material for aqueous batteries due to its low redox potential, high capacity, abundance, and nontoxicity. As for the configuration of ZIB, they have a similar inner structure to rechargeable metal ion batteries, Zn metal as the anode, Zn-intercalating materials as the cathode, and neutral or slightly acidic Zn-containing solutions as the electrolyte (See Fig. 1.7) [14].

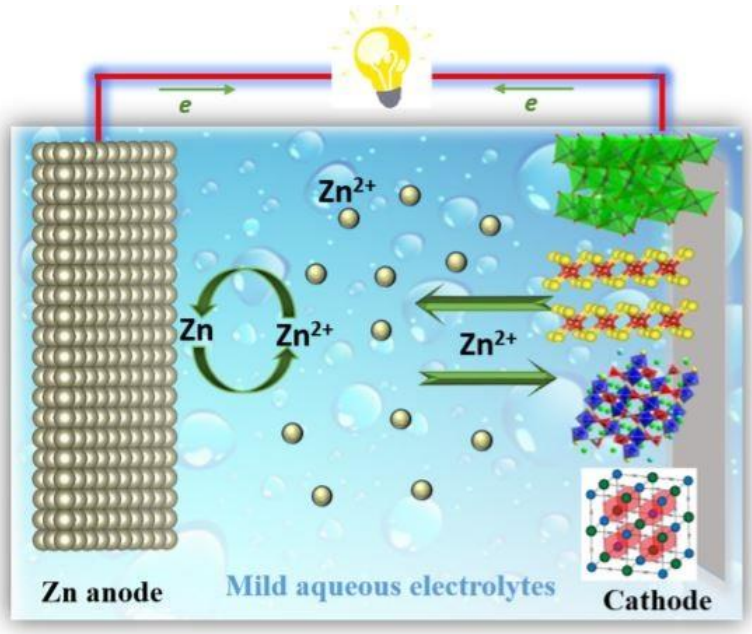

Figure 1.7 Schematic representation of a ZIB application [14].

However, since its working potential (usually 2V) is lower than either LIB or SIB, it is impractical for portable energy storage. Regarding large-scale energy storage systems, they require steady cycles hundreds of times, which is currently an issue for ZIB. As with LIBs, the gravimetric energy and power density of ZIBs, as well as their cost, are strongly influenced by the cathodic materials. In the development of high-performance ZIBs, designing and manufacturing cathode materials with a large storage capacity, a high discharge potential, and a robust crystal structure with simple insertion and extraction paths has been a significant challenge. Only a few materials have been investigated as viable Zn ion host materials to date, including mainly manganese-based compounds, vanadium-based compounds, Prussian blue and its analogs, and organic redox-active compounds [15].

The working principle and storage mechanisms of ZIBs differ according to the cathode material used. The following subchapter will also discuss the reaction mechanisms in ZIBs that have been determined so far, depending on different polymorphic phases of manganese-based cathodes, which is the primary focus of this thesis.

1.3 Manganese-based cathode materials

Manganese-based oxides have several advantages that make them ideal electrode material for energy storage and conversion applications [16]:

- It is the 12th most abundant element on earth.
- MnO_2 is a thermodynamically stable compound int contact with air and in daily operating conditions.
- It is non-toxic material.
- It is not a rare compound, and it can be easily extracted from sores.
- It can be synthesized in several cheap methods (i. e. electrodeposition).

- It shows good performance as a cathode material for different energy storage devices even if it suffers from cyclability issues.
- Theoretical specific capacity is 308 Wh/kg for a single electron transfer.

In addition, owing to their low point of zero charge, large surface area, strong acid sites and easily changeable valence states, participate readily in a variety of oxidation–reduction, catalytic and cation-exchange reactions. In particular, redox process may occur at the surface of the solid, which is not stoichiometric, and typically contains several defects [17].

1.3.1 Manganese dioxide polymorphs

Manganese-based oxides exist in a variety of phases with a wide range of open crystal structures. The basic unit in the MnO_2 structure is composed of one Mn^{4+} ion coordinated by six hexagonally close-packed O^{2-} ions [18]. By altering the connections between these MnO_6 units, a different type of tunnel- or layer-structured polymorphs are formed. Figure 1.8 illustrates the crystallographic formation of various MnO_2 polymorphs. The microstructure and morphology of MnO_2 influence its reaction mechanism and electrochemical properties as a ZIB cathode, as will be discussed in more detail in the next subchapters, where we focused on hollandite (α -MnO_2), epsilon (ε-MnO_2) and birnessite types (δ-MnO_2), which are possible manganese dioxide structures we have synthesized.

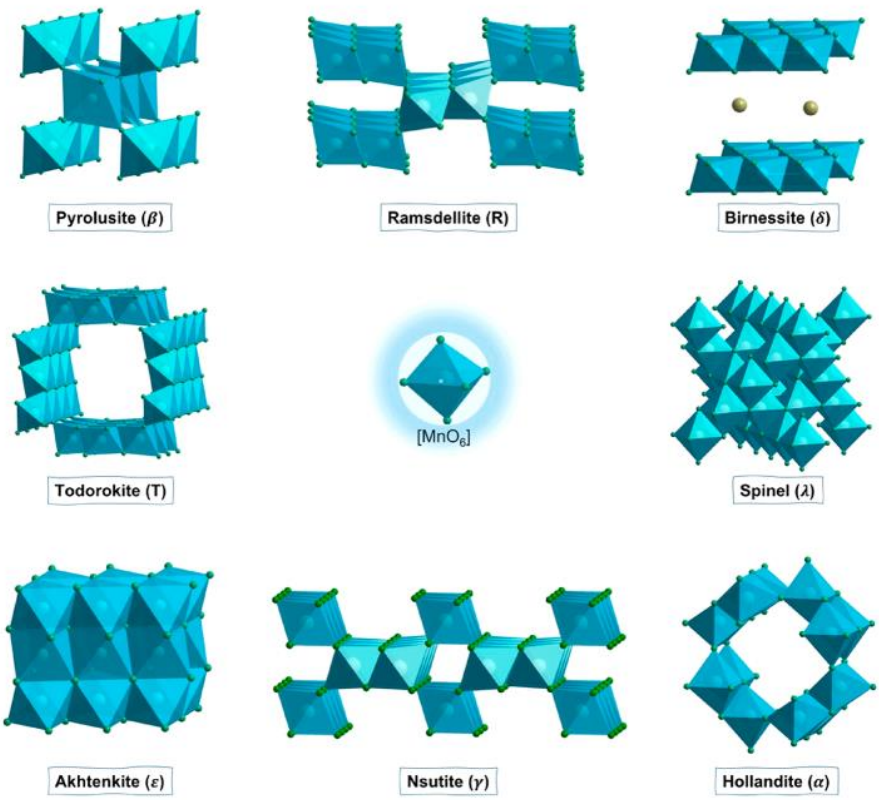

Figure 1.8 Crystallographic formation of different MnO_2 polymorphs characterized by their tunnel (m × n) structures, including β - MnO_2 (1 × 1), R- MnO_2 (1 × 2), δ - MnO_2 (1 × ∞), T- MnO_2 (3 × 3), λ - MnO_2 (1 × 1), ε - MnO_2 (dense), γ - MnO_2 (1 × 1) + (1 × 2), and α - MnO_2 (2 × 2) [15].

1.3.1.1 Hollandite (α -MnO_2)

Among the numerous polymorphs, α-MnO_2 has received the greatest attention due to its large tunnel size (~ 4.6 Å). Taking advantage of the structural advantage, α-MnO_2 can provide a large specific capacity (more than 200 mA h g^{-1}) with a moderate discharge voltage (around 1.3 V vs Zn/Zn^{+}) [12]. However, α-MnO_2 often exhibits rapid capacity fading during cycling and poor high rate performance. Another challenging issue with the α-MnO_2 cathode is the complex Zn^{2+} ion storage mechanism. Until recently, four reaction mechanisms have been proposed, as discussed below.

Zn^{2+} Ion insertion/extraction mechanism

The reversible Zn ion intercalation/deintercalation, which involves a reversible phase shift from tunnel-structured α-MnO_2 to layer-structured Zn-birnessite [19], spinel $ZnMn_2O_4$, or layered Zn-buserite, is the most widely accepted mechanism.

Taking Zn-birnessite as an example, during the discharge, Zn^{2+} ions are electrochemically intercalated into the α-MnO_2 structure, accompanied by a partial reduction of manganese from +4 to +3 valence. The unstable Mn(III) ions subsequently undergo a disproportionation reaction which forms Mn^{4+} and Mn^{2+}, and dissolving nearly one-third of Mn ions into the electrolyte. We present the stoichiometric equations for this disproportionation reaction while examining birnessite type MnO_2. Mn ion dissolution breaks the chains between the layers of α-MnO_2, resulting in a phase transition to the layer-structured Zn-birnessite [19]. While charging, the dissolved Mn^{2+} ions will be intercalated back, forming the interlayer bridges, and recovering the original α-MnO_2 structure (see Fig. 1.9).

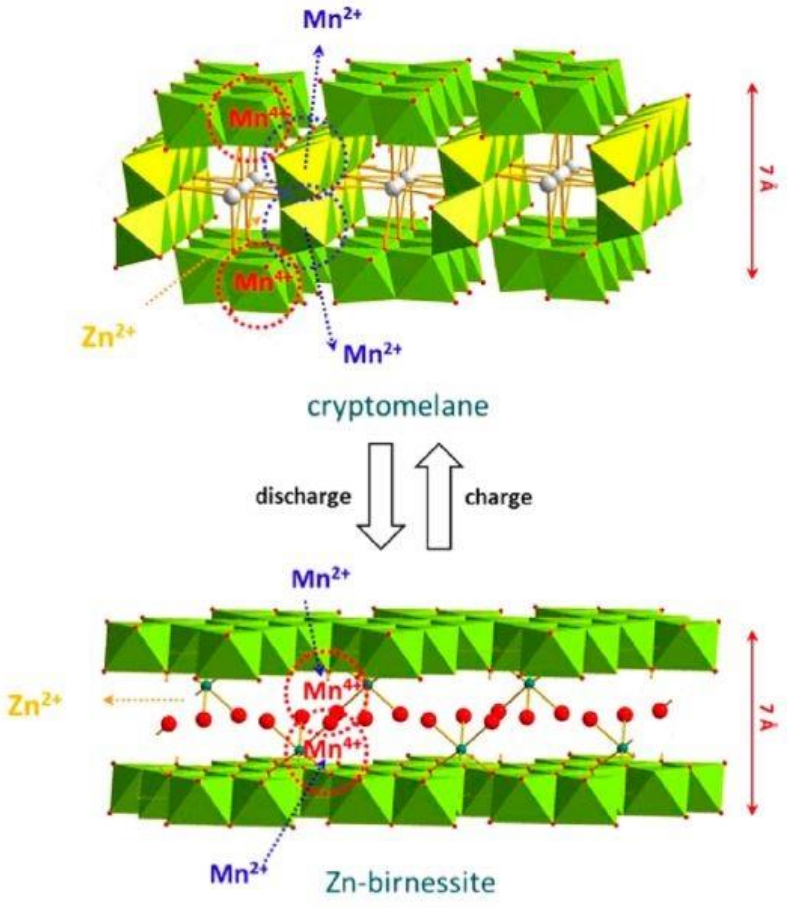

Figure 1.9 Zinc intercalation/deintercalation mechanism in α-MnO_2 illustrated schematically [19].

H^+ and Zn^{2+} co-insertion mechanism

Sun et al. proposed the H^+ and Zn^{2+} cointercalation process for the first time[20] . The galvanostatic intermittent titration technique (GITT) profiles of the Zn/-MnO_2 battery (Figure 1.10) show two unique plateaus during discharge, indicating the presence of two distinct types of ion insertion.

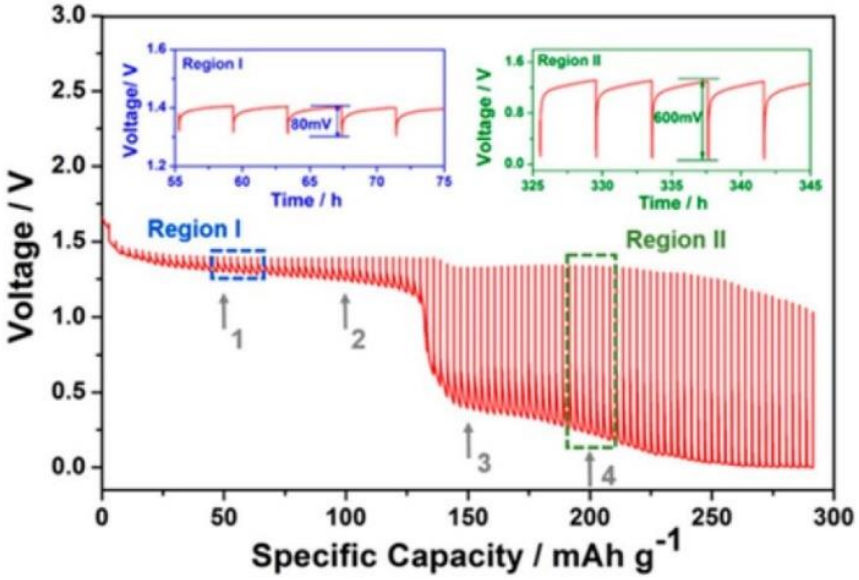

Figure 1.10 GITT profiles of the Zn/MnO_2 battery, illustrating that the two distinct plateaus, region I and region II [20].

Given the large size of Zn^{2+} ions and their strong interactions with the host structure, the high overpotential in region II should be attributed to the slow Zn^{2+} insertion process, whereas the small overpotential in region I should be attributed to the fast H^+ insertion. This hypothesis is supported by the fact that the electrochemical behavior of MnO_2 cathode in a 0.2 M $MnSO_4$ electrolyte without $ZnSO_4$ is significantly different, with only one voltage plateau between 1.8 V and 1.35 V. Due to the absence of Zn^{2+}, the Zn^{2+} ion insertion that corresponds to the voltage plateau in region II would not occur (see Fig. 1.11).

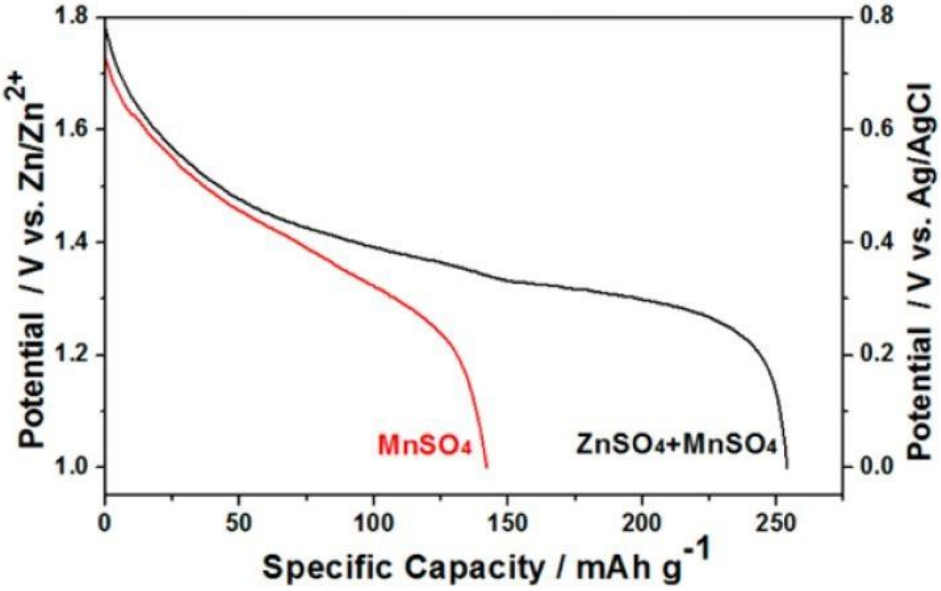

Figure 1.11 Discharge curves of the MnO_2 cathode in a 0.2 M $MnSO_4$ electrolyte with or without $ZnSO_4$ [20].

Chemical Conversion Reaction Mechanism

The extremely reversible chemical conversion process between α-MnO_2 and H^+ was proposed for the first time when MnOOH was detected in discharged products instead of the previously reported intercalated phases, Zn_xMnO_2. According to this mechanism, when water is discharged, H^+ ions from the breakdown of water molecules combine with MnO_2 to generate MnOOH (eq. 1.10); to reach a neutral state, the simultaneously formed OH^- ions react with $ZnSO_4$ and H_2O to form a flakelike phase, $ZnSO_4$ $[Zn(OH)_2]_3$ xH_2O (eq. 1.11) [21].

$$MnO_2 + H^+ + e^- \rightarrow MnOOH \tag{1.10}$$

$$\frac{1}{2}Zn^{2+} + OH^- + \frac{1}{6}ZnSO_4 + \frac{x}{6}H_2O \rightarrow \frac{1}{6}ZnSO_4[Zn(OH)_2]_3 \cdot xH_2O \tag{1.11}$$

STEM-EDS mapping of the fully discharged MnO_2 cathode further supports this mechanism. The presence of Zn is rarer in the short MnO_2 nanorods, implying that Zn does not intercalate into MnO_2. However, Zn is primarily found in the flakelike $ZnSO_4$ $[Zn(OH)_2]_3$ xH_2O, corroborating the chemical conversion reaction process described.

Dissolution-Deposition Mechanism

Mn2+ dissolution and the generation/decomposition of $Zn_4SO_4(OH)_6$ H_2O (ZHS) have been seen in aqueous ZIBs with a Mn-based cathode and a ZnSO4 electrolyte, which are commonly regarded as side reactions and the cause of capacity fading [21]. As a result, $MnSO_4$ additives are frequently added to the $ZnSO_4$ electrolyte to suppress these side reactions through common ion and/or electrostatic shielding effect.

A recent study proposed a dissolution-deposition mechanism in the Zn/MnO_2 battery and confirmed the capacity contribution from the reversibly formed ZHS. In particular, during the first discharge, Mn^{2+} dissolves from the reaction between α-MnO_2 and H_2O molecules. The simultaneously released OH^- ions will react with SO_4^{2-} anions and Zn^{2+} ions, forming the ZHS phase on the cathode surface. While charging, the generated ZHS reacts with the dissolved Mn^{2+} to form birnessite-MnO_2. They could observe similar reversible electrolytic (dissolution-deposition) reactions using the birnessite-MnO_2 host instead of the pristine MnO_2 in subsequent cycles. Interestingly, during the whole energy storage process, Zn^{2+}/H^+ intercalation/deintercalation reaction only happens in the undissolved pristine MnO_2, therefore contributing a limited specific capacity [22]. In the contrary other study proposed a complex dissolution-deposition mechanism for the Zn/MnO_2 battery and confirmed that the reversibly formed ZHS contributes to capacity.

1.3.1.2 ε-MnO_2

The crystal structure is an intergrowth of pyrolusite and ramsdellite domains. It is quite difficult to identify due to its low crystallinity. The epsilon polymorph is the gamma one, but it is more disordered. In particular, it is also difficult to distinguish the gamma modification with the epsilon one. It is a structure full of detects, even [2x2] tunnels are also present. With an increasing number of defects and a decreasing order within the domains, the distribution of manganese in the octahedral voids of hexagonally close packed oxygen atoms becomes more and more statistical [23].

A dense packing of the MnO6 octahedra in ε-MnO_2 (Fig. 1.8) makes it unfavorable for the fast metal ion intercalation/deintercalation in the energy storage process. However, the previously indicated electrolytic (dissolution/deposition) reaction mechanism endows the Zn / / ε -MnO_2 battery with a two-electron redox reaction of Mn^{4+}/Mn^{2+}, a theoretical capacity of 616 mA h g^{-1}, and a theoretical voltage greater than 2 V. This unique electrolytic Zn-MnO_2 battery can be synthesized through potentiostatic electrodeposition process in the 1 M $ZnSO_4$ + 1 M $MnSO_4$ electrolyte. During the first potentiostatic charging at 2.2 V, Zn^{2+} and Mn^{2+} cations in the electrolyte will be deposited on the current collectors of anode (Zn-foam) and cathode (carbon fiber), forming the initial active material of Zn metal and ε-MnO_2, respectively.

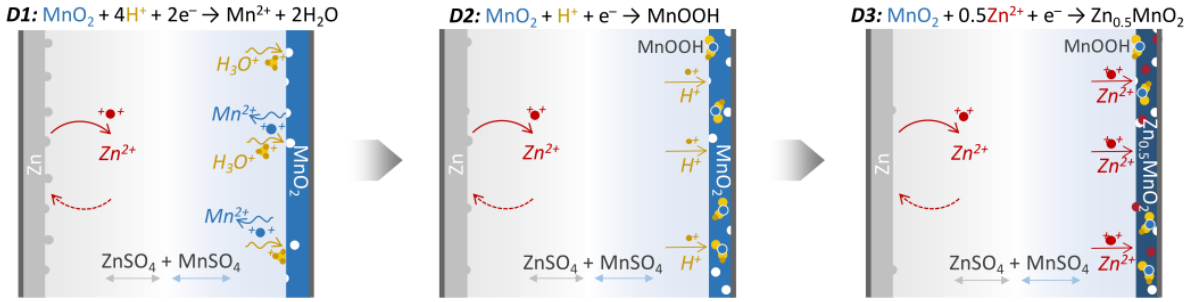

Figure 1.12 A schematic of galvanostatic discharge with 3 steps [24].

The reversible galvanostatic process then continues in three steps: MnO_2/Mn^{2+} electrolytic reaction, followed by H^+ and Zn^{2+} ion intercalation (Fig. 1.12). The electrolytic reaction has the greatest contribution in specific capacity. Adding 0.1 M H_2SO_4 to the electrolyte could further increase the electrochemical window to 2.4 V. Furthermore, the numerous Mn vacancies in the acidic electrolyte deposited MnO_2 would improve the kinetics of proton and electron transport during electrolysis processes. Taking advantage of these benefits, the new electrolytic Zn-MnO_2 battery design has a high discharge voltage of 1.95 V and a huge capacity of 570 mA h g^{-1} [24].

1.3.1.3 δ -MnO_2(Birnessite)

Birnessite-type compounds denote a class of nonstoichiometric Mn oxides in which some Mn(IV) is replaced by Mn(III) or Mn(II). Birnessite is a poorly crystallized form of manganese dioxide, characterized by a two-dimensional layered structure formed by edge-sharing MnO_6 octahedra, generally with hydrated cations (e.g. Na^+, K^+, Ca^{2+}, Zn^{2+}) in the interlayers, compensating the small overall negative charge.

Birnessite is represented by a generalized elemental formula, $A_xMnO_{2-y}(H_2O)_z$ in which A is a cation and the average oxidation state of mixed-valence normally falls between 3.6 and 3.8, which represents a predominance of Mn(IV) with minor amounts of Mn(III) or Mn(II).

Owing to their very open structure, birnessite-type compounds readily undergo cation-exchange reactions, exhibiting a high adsorption capacity for heavy metal cations. Moreover, birnessite-type compounds, due to their microporous nature and/or an irregular stacking of these layers, readily participate in oxidation–reduction reactions.

Mechanism of electrodeposited (ECD) δ -MnO_2

The majority of papers reports the formation of birnessite in by chemical means and in powder form, but a relatively literature corpus described the electrodeposition of birnessite films, incorporating range of cations [25]–[28].

During electrodeposition of birnessite, an intermediary Mn(III) compound, α-MnOOH (groutite), is formed in deaerated solutions leading to mixed thin layers of birnessite and groutite. Thin layers of pure birnessite can be efficiently electrodeposited in aerated solutions due to the oxidation of groutite by dissolved oxygen in such solutions [29].

The majority of literature studies was done in strong acidic sulphate media with the aim of preparing manganese dioxide compounds according to the overall reaction [30]:

$$\mathrm{Mn(II)} + 2\mathrm{H_2O} \rightarrow \mathrm{MnO_2} + 4\mathrm{H^+} + 2\mathrm{e^-} \quad (1.12)$$

Nevertheless, this overall reaction does not reflect the complexity of the mechanism. Some papers have studied the electrodeposition mechanism of MnO_2 compounds and have shown that intermediary reactions occur with Mn(III) species, which play a major role [31]. In acidic solution, Mn(III) species are soluble and may rapidly disproportionate:

$$2\ \mathrm{Mn(III)} \rightarrow \mathrm{Mn(II)} + \mathrm{Mn(IV)} \quad (1.13)$$

In this case, only Mn(IV) compound is formed at electrode. In contrast, in low acidic or neutral solutions, Mn(III) species precipitate rapidly as MnOOH:

$$\mathrm{Mn(III)} + 2\mathrm{H_2O} \rightarrow \mathrm{MnOOH} + 3\mathrm{H^+}\ \mathrm{(fast)} \quad (1.14)$$

This latter compound can be slowly oxidized to Mn(IV):

$$\mathrm{MnOOH} \rightarrow \mathrm{MnO_2} + \mathrm{H^+} + \mathrm{e^-}\ \mathrm{(slow)} \quad (1.15)$$

Therefore, the deposition of pure MnO_2 is more difficult, that is why few studies have reported experimental results in neutral media [30], [32], [33]. However, the use of neutral solutions is certainly of interest as it allows the production of various manganese oxide compounds as illustrated by the Pourbaix diagram [34].

Since all electrochemical reactions include exchanges of proton and the media is neutral and not buffered, it seems interesting to monitor pH of solution during electrochemical measurements (Fig 1.14).

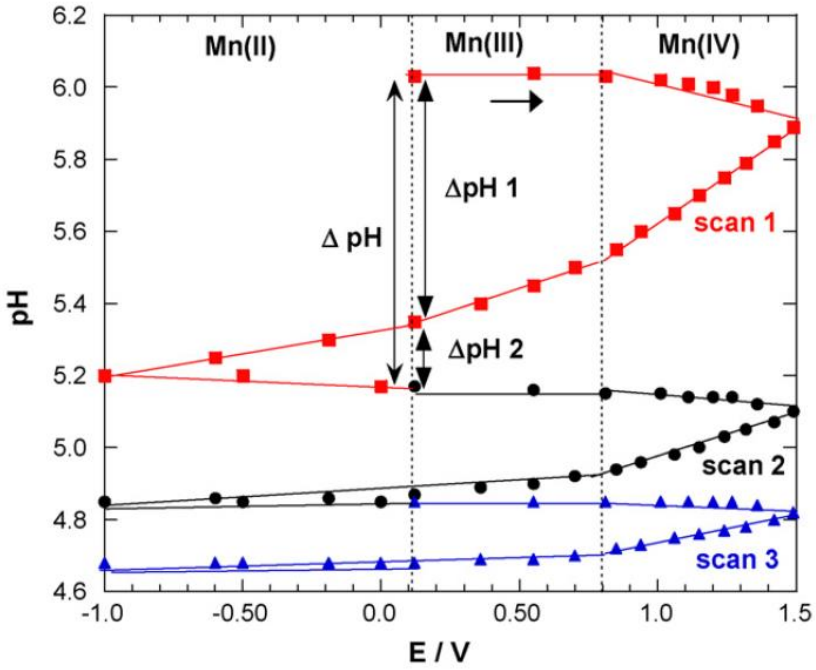

Figure 1.13 pH evolutions of the solution during CV on SnO2 electrode in dearated 0.4 M Na_2SO_4 and 0.004 M $MnSO_4$ solution, $pH_{initial}$ = 6, v = 10 mV/s [Larabi-Gruet_08].

Birnessite's nature is highly dependent on the solution's pH, and its creation is a highly complex process [52,53 of Larabi-Gruet_08]. Therefore, given the experimental conditions, we might consider the possibility of the formation of two birnessite-type compounds, with insertion of Na^+ and H^+.

The production of protons associated to the electronic exchanges induces a significant pH decrease (Figure 1.15), and this may affect the mechanism of synthesis.

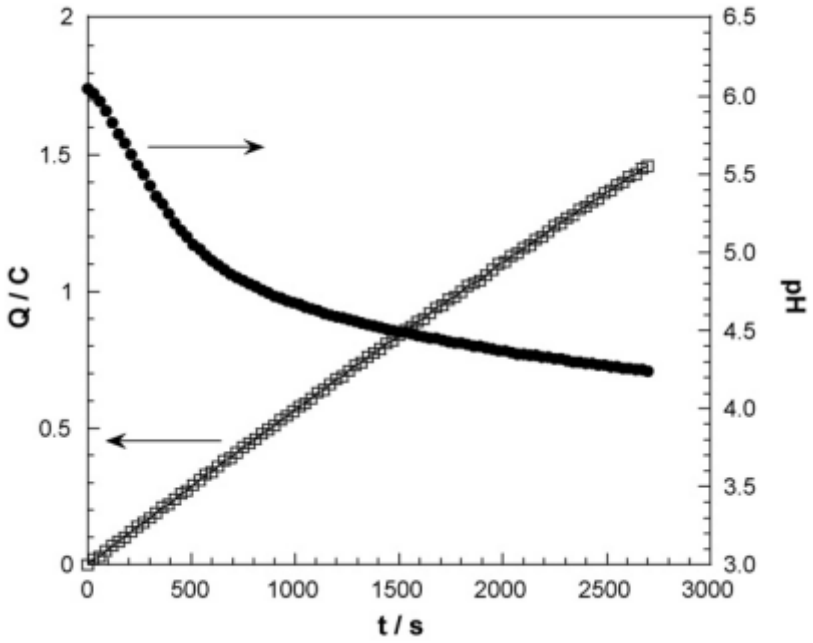

Figure 1.14 Evolutions of charge and pH of the solution during the potenitostatic electrodeposition at E=1 V on SnO_2 electrode in dearated 0.4 M Na_2SO_4 and 0.004 M $MnSO_4$ solution, $pH_{initial}$ = 6 [29].

To prove this point, the potentiostatic electrodeposition was performed at a constant pH by adding NaOH 10^{-2} mol L^{-1} solution during the potential imposition. A very homogeneous black

thin layer with a good adherence was also obtained. XRD pattern shown in Fig. 1.16 curve b, indicates the presence of the same compounds as above, birnessite and groutite. However, examination of curves a and b suggests that Na-birnessite formation was promoted over H-birnessite formation at pH 6, (Na-birnessite: peaks (1) (100%), (4) (27%), (5) (14%) according to JCPDS 43-1456 card), in accordance with literature [52,53 of Larabi-Gruet_08]. XRD pattern also supports the presence of an amorphous compound and/or very small crystallites (broad peak around 20◦) in a larger extent than above. This point can be explained by a quicker precipitation, which does not favor the crystallization of solids and/or a great size of crystallites.

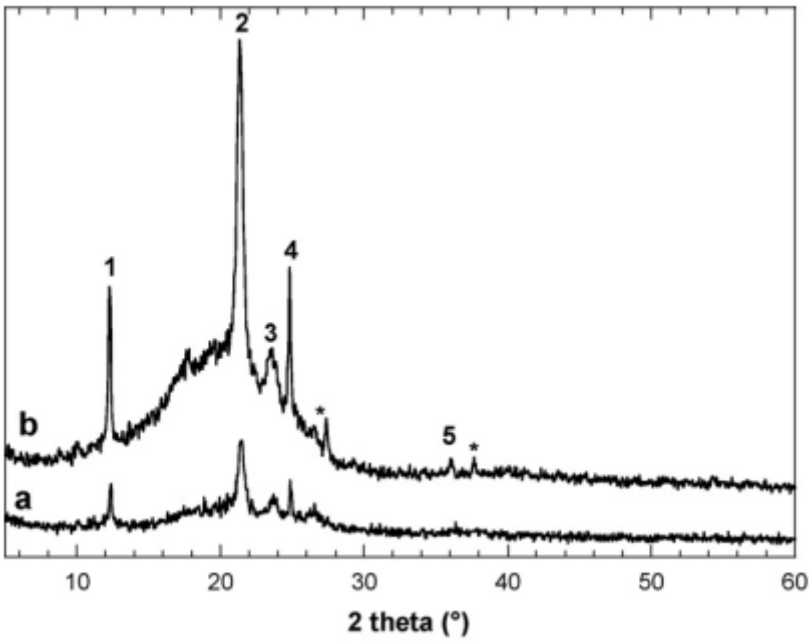

Figure 1.15 XRD patterns of solids electrodeposited at pH free (curve a) and, at pH maintained at 6 during synthesis (curve b). Electrodeposition was done by potentiostatic technique onto SnO_2 electrode in dearated 0.4 M Na_2SO_4 and 0.004 M $MnSO_4$ solution, $pH_{initial}$ = 6, $E_{imposed}$= 1 V, t=2700s [29].

According to the following equations, an intermediary Mn(III) compound is formed during the electrodeposition of birnessite from the oxidation of soluble Mn(II) in neutral sulphate solutions.

Grouite:

$$Mn(II) + 2H_2O \rightarrow \alpha MnOOH + 3H^+ + e^- \quad (1.16)$$

Birnessite (Overall reaction):

$$7Mn(II) + 13H_2O \rightarrow Mn_7O_{13} + 26H^+ + 12e^- \quad (1.17)$$

Reaction from intermediary insoluble Mn(III) species:

$$7Mn(II) + 14H_2O \rightarrow 7\alpha MnOOH + 21H^+ + 7e^- \quad (1.18)$$

$$7\alpha MnOOH \rightarrow Mn_7O_{13} + H_2O + 5H^+ + 5e^- \quad (1.19)$$

The presence of groutite at the end of the electrodeposition process indicates that reaction 1.19 has a slower kinetics than reaction 1.18. In order to identify the electrochemical conditions of electron transfer of Mn(II) in neutral deaerated sulphate solution, cyclic voltammetry (CV) was performed in by Larabi-Gruet et al. [29]. We will provide insight into the general findings of the CV scan in Chapter 4.

Chapter 2 Experimental Techniques and Methods

In this chapter, relevant experimental procedures are briefly explained: potentiostatic technique, linear sweep voltammetry, cyclic voltammetry, galvanostatic technique, Raman spectroscopy, X-ray diffraction and scanning electron microscopy. Testing and fabricating protocols are reported in details: preparation of the cathodes by electrodeposition, hydrothermal synthesis of α-MnO_2, and preparation of drop cast and spray coated electrodes. The full list of specifics for each tested and mentioned sample is reported.

2.1 Electrochemical Techniques

2.1.1 Potentiostatic Technique (PS)

The potentiostatic technique can be used as a polarization experiment to observe anodic and cathodic behaviours of metals on electrodes. In this thesis, anodic electrodeposition has been performed by this technique, which is expected to give appropriate control of the process by applying a suitable potential and thereby limiting the side reactions to a minimum.

Electronic hardware called potentiostat allows control of the voltage across the working electrode (WE) and counter electrode (CE) pair, and it adjusts this voltage to maintain the potential difference between WE and reference electrode (RE). The potential is held constant in a predetermined manner as the current is measured as a function of time or potential. Thus the response from the potentiostat, which is current, actually is the experimental observable. The basic experimental system is illustrated in Figure 2.1 [10].

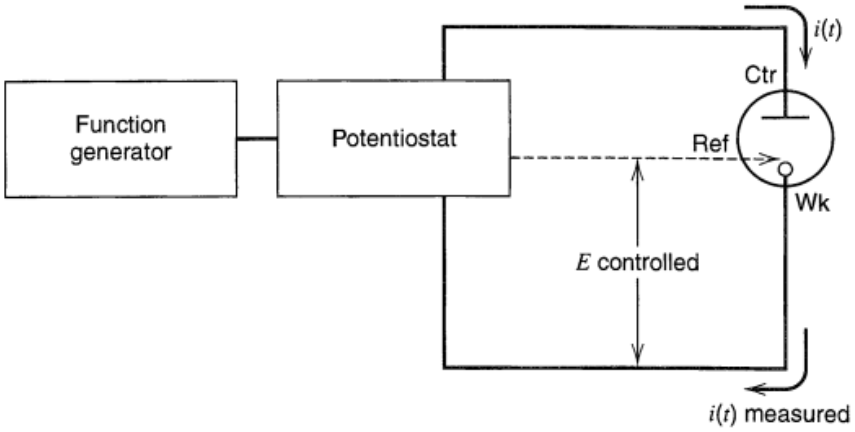

Figure 2.1. Experimental arrangement for controlled -potential experiments. [10]

Chemically, this technique provides the flow of electrons needed to support the active electrochemical processes at rates consistent with the potential. In the most general form, the process can be described as follows:

$$A^{x+} + xe^{-} \rightarrow A \tag{2.1}$$

In order to perform this reaction, by setting the potential at "mass-transfer-limited" conditions, we enhance the kinetics for reduction of A^{x+}, being so rapid that it cannot coexist with the electrode. As a result, the surface concentration goes nearly to zero.

During this process, first, the electrode reduces the nearby cation to the stable anion radical. This event is instantaneous and requires a large amount of current at the beginning. This initial reduction creates a concentration gradient that in return produces a continuing flux of A^{x+} to the electrode surface, where it must be eliminated by reduction. The flux of material, and current as well, is proportional to the concentration gradient at the electrode surface. However, the

continued flux causes the depletion of A to thicken, thus the slope of concentration profile at the surface declines with time, and so does the current (Figure 2.2.b and 2.2.c).

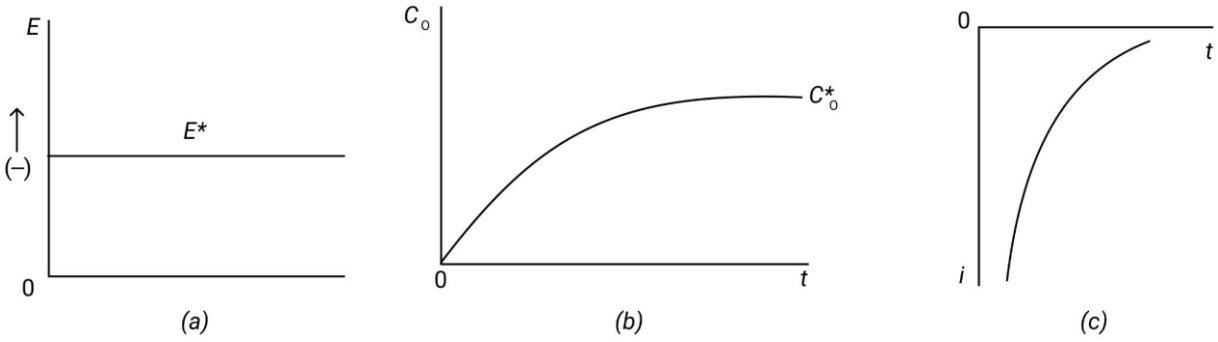

Figure 2.2. (a) Constant potential vs. time. (b) Concentration profile for the experiment. (c) Current flow vs. time.

2.1.2 Linear Sweep Voltammetry (LSV) and Cyclic Voltammetry (CV)

Linear Sweep Voltammetry (LSV) is a potentiodynamic measurement, where the potential is a parameter controlled externally. The potential is changed at a constant rate, and the resulting current is a function of time given by:

$$\nu \equiv dE/dt \tag{2.2}$$

The current is plotted as a function of potential on X-Y coordinates, which is known as 'voltammogram', as shown in Figure 2.3.

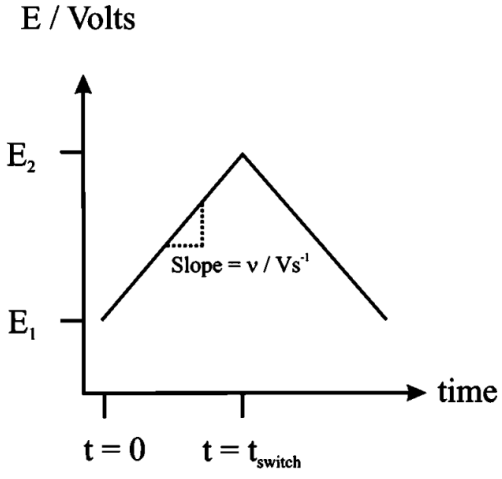

Figure 2.3. Simplified potential waveform applied to the working electrode in the linear sweep voltammetry experiment. [35]

In particular, if the potential is swept forward and backwards between two fixed values, we refer to it as "cyclic voltammetry (CV)" technique. The starting potential of the working electrode is preferably chosen where the chemical species are not initially oxidized or reduced. The second potential is usually selected so that the voltage window can contain these reactions of interest. [35]

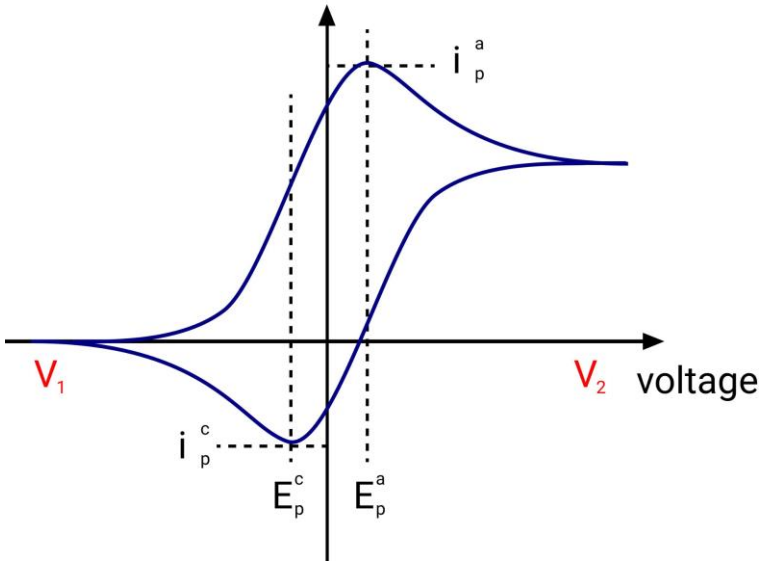

Figure 2.4. Simplified potential waveform applied to the working electrode in the cyclic voltammetry experiment.

After the formation of new chemical species, the catalyst can be checked in an extended voltage window, as it is illustrated on Figure 2.4. CV assures the fundamentals for the approximation of the catalytic performances such as:

- the onset potential of redox reactions
- the peak current of faradaic process being studied at a given potential
- the kinetic performances of the catalytic samples undergo these reactions.

2.1.3 Galvanostatic Technique (GS)

On the previous techniques, the potential of an electrode was controlled, while the current was determined as a function of time. Galvanostatic technique is the case, where the current is controlled and the potential becomes the dependent variable, which is determined as a function of time. This technique is generally called galvanostatic technique, because a small constant current is applied to the working electrode.

The measurement is implemented by applying the controlled current between the working and counter electrodes with a current source (called a galvanostat) and recording the potential between the working and reference electrodes.

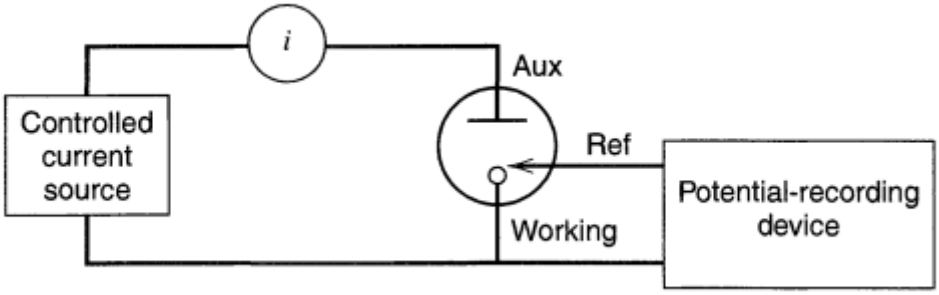

Figure 2.5. Simplified block diagram of apparatus for galvanostatic measurements. [10]

Following the rapid application of a current step, a non-faradaic current is present and leads to the charging of the double-layer capacitance. If $dA/dt = 0$, then i_c is given by:

$$i_c = -AC_d(d\eta/dt) = -AC_d(dE/dt) \tag{2.3}$$

where C_d stands for the differential capacitance of the electrical double layer near the electrode, and η is the overpotential. Thus, of the total applied constant current (i), only a portion, i_f, goes to the faradaic reaction:

$$i_f = i - i_c \tag{2.4}$$

Since dE/dt is a function of time, i_c and i_f also vary with time, even when i is constant. If the explicit form of dE/dt or $d\eta/dt$ is known, this condition can be treated as a case of programmed current chronopotentiometry, in which currents are programmed to vary with time in a particular way rather than remaining constant. [10]

With controlled-current techniques it might not be straightforward to analyze data for multicomponent processes and stepwise reactions, and the waves observed in E-t transients are typically less well-defined than those observed in potential sweep i-E curves. Therefore, it is more reasonable to rely on control-potential methods to ensure the stability of results.

2.2 Synthesis Methods of Manganese Dioxide

This subchapter aims to explain the electrochemical behaviour of Manganese, before presenting further information about protocols used for fabrication and electrodeposition of MnO_2. In this context, Pourbaix diagrams provide thermodynamic information in a compact way.

Pourbaix diagrams plot electrochemical stability as a function of pH for various redox states of an element. These diagrams are basically phase diagrams that map the conditions of potential and pH in aqueous solutions where different redox species are stable. Water redox reactions are also reported. The lines in Pourbaix diagrams represent redox or chemical reactions, and represent the fields of the diagram where couples of species can coexist in equilibrium. For

example, in the diagram for Mn below (Figure 2.4), the tilted line between the Mn^{2+} and MnO_2 regions represents the reaction $Mn^{2+} + 2H_2O \rightarrow MnO_2 + 4H^+ + e^-$, which has a standard potential of 1.0V at pH=2.

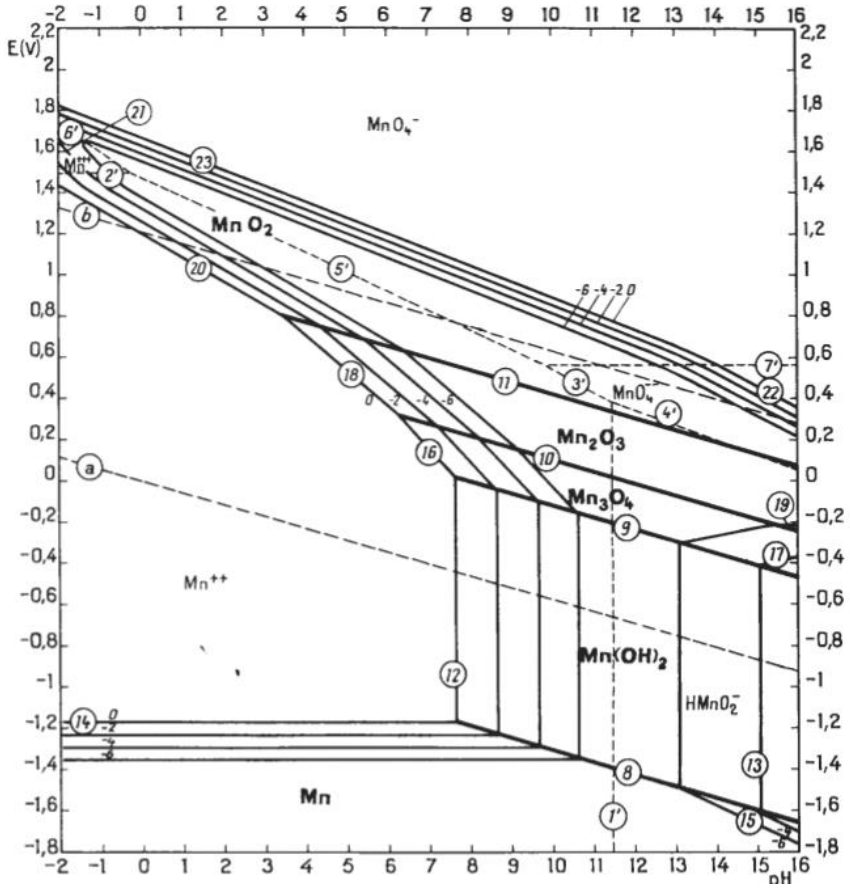

Figure 2.6. Potential-pH equilibrium diagram for the system manganese-water, at 25°C. [34]

The water redox lines have particular meaning in a Pourbaix diagram for Mn. It should be noted that liquid water is stable only in the region between the dotted lines. Below the "*line a"*, water is unstable relative to hydrogen gas, and above the *"line b"*, water is unstable in relation to oxygen. The entire domain of manganese thermodynamic stability lies well below the H_2 line. Manganese, being a very base reducing metal, is thus thermodynamically unstable in the presence of water and appears to react with it, resulting in the evolution of hydrogen. In practice, this reaction is slow, most likely due to the metal's relatively high hydrogen overpotential.

Manganese is readily dissolved in acid or neutral oxidizing solutions, yielding light pink manganese ions Mn^{2+}. A minor oxidizing activity, such as the one of oxygen evolution reaction (OER), can oxidize manganese solutions, resulting in the formation of solid oxides: brown-black Mn_3O_4, black Mn_2O_3, or various brown or black anhydrous or hydrated MnO_2. [34]

As the pH increases, manganese dioxide (MnO_2), rather than permanganate (MnO_4^-), is the form of manganese that is more stable in the presence of water. As a result, MnO_4^- tends to oxidize water with OER and the separation of MnO_2 by the following reactions:

$$4MnO_4^- + 16H^+ + 12e^- \rightarrow 4MnO_2 + 8H_2O \qquad (2.5)$$

$$6H_2O \rightarrow 3O_2 + 12H^+ + 12e^- \quad (2.6)$$

Overall Reaction: $$4MnO_4^- + 4H^+ \rightarrow 4MnO_2 + 3O_2 + 2H_2O \quad (2.7)$$

The domains of stability of the manganese ion Mn^{2+} and the permanganate ion MnO_4^- are separated by a domain of stability of various oxides which, although very important in neutral or slightly acidic solutions, is considerably smaller in strongly acidic ones; hence in slightly acidic, neutral or alkaline solutions, the reduction generally ceases at MnO_2 or at a mixture of lower oxides.

In this work, we have concentrated on the synthesis of MnO_2 and on its electrochemical behaviour under conditions relevant to ZIB operation.

MnO_2 can exist in different structural shapes like, α-, β-, γ-, δ-, ε- and λ-types and so on, when the basic structural unit octahedron [MnO_6] is linked in particular ways [x]. The properties of MnO_2 are essentially influenced by their phases and morphologies; besides, the operating properties for Zn-MnO_2 applications also depend on the phase of MnO_2.

2.2.1 Electrodeposition Method

Electrodeposition, also known as electrolytic deposition, is the traditional method of covering a thin layer of one metal on top of another metal in order to change its surface properties. It is a method that employs electrical current to reduce/oxidize the cations of a desired material in an electrolyte and coat such materials as a thin film on a conductive substrate surface. Therefore, the surface properties of a material can be customized, and new materials for a wide range of applications can be investigated using this technique. Figure 2.5 illustrates a simple electrodeposition system.

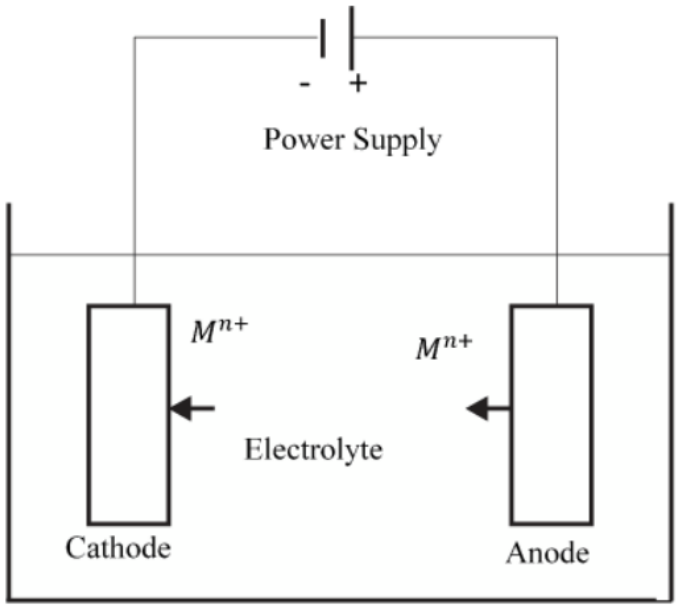

Figure 2.7. Schematic representation of electrodeposition.

In particularly, MnO_2 electrodeposition will be examined in the following chapter by corroborating via the results obtained at the laboratory.

Preparation of the Cathodes by Electrodeposition

Electrodeposited MnO_2 typically forms in the δ-phase (birnessite). For the electrodeposition of MnO_2 thin films, two different techniques were implemented to deposit manganese oxide: potentiodynamic (CV) and potentiostatic (PS). A three-electrode electrochemical cell was set up in a glass beaker of suitable size, connected to a potentiostat (AMETEK VersaSTAT 3F), as shown in Figure 2.8. The VersaStudio software was adopted to control the electrodeposition procedures and to collect the experimental data.

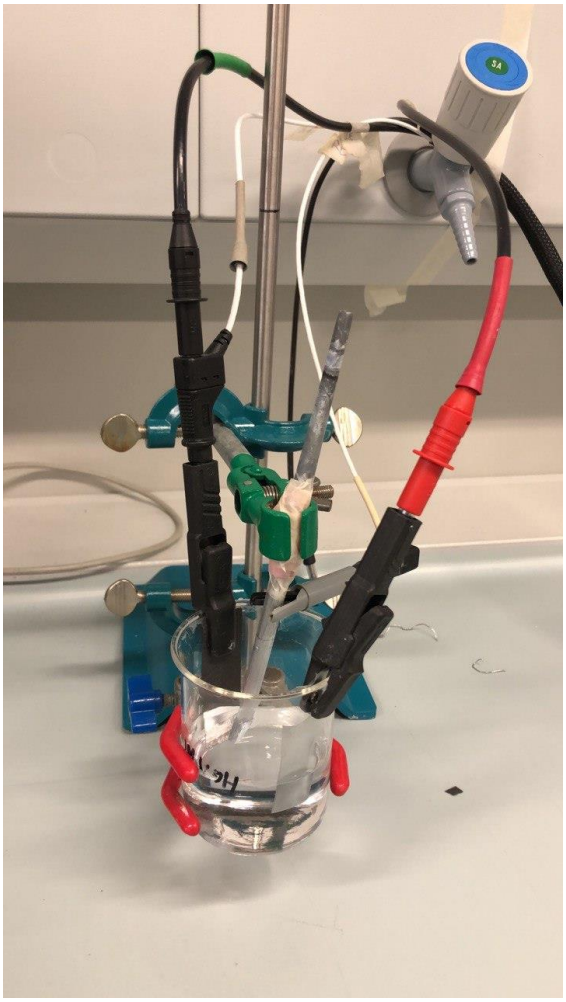

Figure 2.8. Photograph of a three-electrode cell setup connected to the potentiostat.

In this thesis, electrodeposition protocols are divided into four sections. Setup of each section is described in detail under the following subchapters.

2.2.1.1 Setup for Section ECD1

MnO_2@CP_0, MnO_2@CP_1, and MnO_2@CP_3 electrodes were synthesized by electrodeposition that carried out in a three-electrode cell with carbon paper as the working electrode, Zn metal foil/rod as both counter and reference electrodes in the 2 M $ZnSO_4$ + 0.2 M $MnSO_4$ aqueous solution. Firstly, galvanostatic charge is applied on the cell at 0.2 mA cm^{-2} to 1.8 V (vs Zn/Zn^{2+}) and then maintained at 1.8 V by applying PS for 8 hours. Alternatively, MnO_2@CP_2 was prepared with the same protocol in a split cell while both counter and reference electrodes are Zinc and in short circuit with each other. (Figure 2.9)

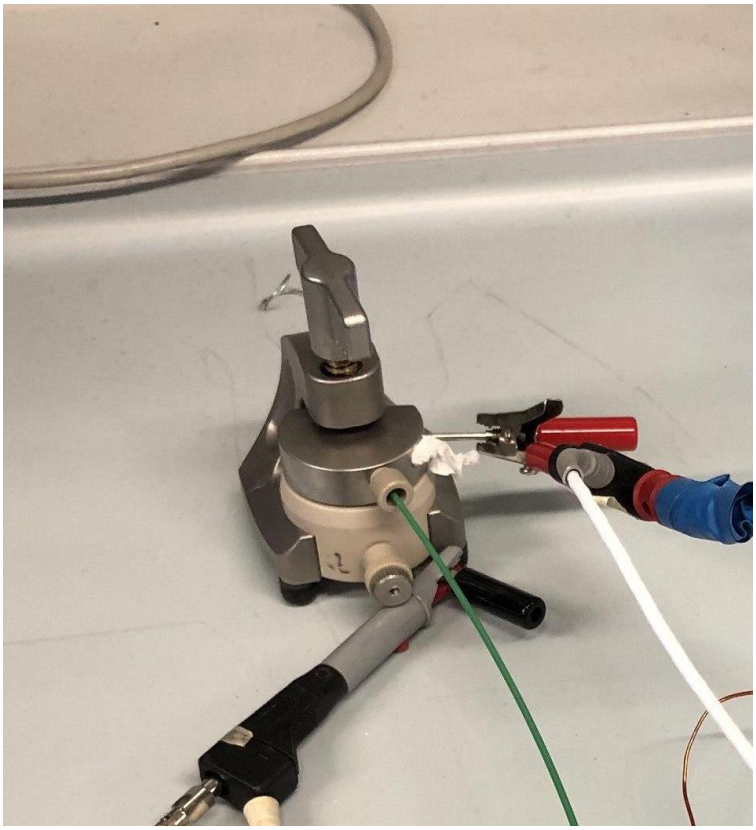

Figure 2.9. Photograph of a split cell setup.

2.2.1.2 Setup for Section ECD2

We deposited manganese dioxide on two different working electrodes, which were glassy carbon or Platinum (Pt). In a three electrode cell, we used LSV technique in the range of [0.239 V, 2 V] for glassy carbon, and CV technique mostly in the range of [0 V, 1.85 V] for Pt. The reference electrode was silver/silver chloride (Ag/AgCl) for both. Depending on the working electrode, the counter electrode was Pt wire electrode (for glassy carbon) or graphite rod (for Pt).

We applied different scenarios by changing substrates in the bulk solution and temperature of the cell as shown in table 2.1.

Table 2.1. Different scenarios of Section ECD2

Working Electrode	Bulk Solution	Temperature [°C]
Glassy C	0.1 M $MnSO_4$	22
Glassy C	0.1 M $MnSO_4$ + 1 M $ZnSO_4$	22
Pt	0.1 M $MnSO_4$	22
Pt	0.1 M $MnSO_4$ + 1 M $ZnSO_4$	22
Pt	0.1 M $MnSO_4$ + 0.1 H_2SO_4	22
Pt	0.1 M $MnSO_4$ + 0.5 H_2SO_4	22
Pt	0.1 M $MnSO_4$ + 0.5 H_2SO_4	90
Pt	0.1 M $MnSO_4$ + 0.5 $H2SO_4$ + 1 M $ZnSO_4$	22
Pt	0.1 M $MnSO_4$ + 0.5 H_2SO_4 + 1 M $ZnSO_4$	90

2.2.1.3 Setup for Section ECD3 and ECD4

The electrochemical cell was in a glass beaker with three electrodes. The reference electrode was a commercial silver/silver chloride (Ag/AgCl). The counter electrode was a large-area platinum wire braid. After each cyclic voltammetry measurement for electrodeposition (ECD-CV), platinum was kept in sulfuric acid for 10 minutes. Glassy carbon and carbon paper (CP) were used as working electrodes for Section ECD3 and Section ECD4 respectively. Glassy carbon electrodes were polished as described in "Preparation of RDE Electrode" part, and then both working and counter electrodes were sonicated separately before each ECD-CV.

There were 3 different ECD-CV setups in 4 mM $MnSO_4$, 4 mM $MnSO_4$ + 0.1 M Na_2SO_4, and 4 mM $MnSO_4$ + 0.1 M $ZnSO_4$ solutions in the range of [1.5 V, -1.0 V] starting from open circuit voltage at 10 mV s^{-1}.

2.2.2 Hydrothermal Synthesis of α-Manganese Dioxide

As far as hydrothermal synthesis is concerned, we focused on α-type (cryptomelane) nanostructures.

2.2.2.1 Hydrothermal Method

314 mg of Potassium sulfate, 486 mg of Potassium Persulfate, and 203 mg of Manganese (II) sulfate are dissolved in 10 ml of Millipore water and placed into a G30 Wide-Neck reaction vessel with a magnetic stirring bar. Stirring and heating processes are operated in a microwave Reactor (Anton Paar Monowave 450). Inside the reactor, the mix is heated twice to 25°C and to 200°C, held at these temperatures for 10 minutes each, cooled down to 55°C at last. During

all stages, it is stirred at 600 rpm and, the power is kept at maximum (1850 W) to synthesize α-MnO_2 phase abundantly, since a lower power input favours β-MnO_2 formation.

The collected mixture is centrifuged around 4 or 5 times at 4350 rpm for 10 minutes. Between each centrifugation, the liquid part is extracted and replaced with Millipore water and shaken for 30 seconds. Since the synthesis process leads to the acidification of the aqueous matrix, the pH value of the liquid mix is controlled to check to effectiveness of the centrifugation processes.

The obtained particles are dried in a vacuum oven under a vacuum range of ca.100 mbar, at 60°C for 12-24 hours. The product coming out of the oven is ground with an agate pestle.

2.2.2.2 Preparation of the Cathodes by Drop Casting and Spray Coating

I employed two different ink preparation protocols, aimed at the application of the catalyst by drop-casting and spray coating. Generally, inks can be Nafion based and PTFE based, , but fror this study, I chose Nafion for both applications, since its ionomeric nature results in the formation of hydrophilic channels that allow access of water and ions all the way to the electrode surface. On the contrary, PTFE is hydrophobic and tends to exclude water from the surfaces coated with it. The amount of Nafion depends on the application.

2.2.2.2.1 Ink preparation for Drop Casting

The Nafion solution consists of 39.85 mL H_2O (Millipore water), 10 mL of EtOH, and 0.350 mL 5 wt.% Nafion solution. All the elements are mixed into a beaker and the solution is stored sealed to avoid evaporation of the solvent, under magnetic stirring.

To form the ink, MnO_2 and C65 powders are introduced 32 mg each in a glass container. After adding 16 mL of the Nafion solution ready-prepared, then a magnetic stirring bar, the mixture is kept under stirring for 10 minutes. Then, immerse the sonicator tip is immersed in the solution and apply sonication while stirring for 10 minutes (The sonicator tip is immersed until the point where the magnetic stirrer can still rotate, and kept away from edges concurrently.) Sonication process was implemented under minimum power (P=10 W) and maximum frequency (C=100%, A=20%). Finally, the ink is kept under stirring until it is used. For better reproducibility, the ink has to be used after about 12-24 h since preparation.

2.2.2.2.2 Preparation of RDE Electrode by drop casting

Before each ink application (protocol A), RDE GlassyC disk is gently wiped with a precision cloth and some millipore water. The surface is dried with the same cloth. It is advisable to repeat the technique 3 to 5 times. When there is visible material remaining on the electrode surface, more drastic cleaning is applied with 0.3 μm alumina. Then it is sonicated for 30 seconds. Excessive polishing favours catalysts detachment facilely during RDE experiments. In view of this observation, grinding with alumina, leading to a controlled degree of roughness, was found to improve adhesion. For aggressive cleaning, the backing is removed and affixed a Nylon polishing pad to a stiff flat surface. After dispensing a small volume of 5 μm alumina slurry on the Nylon (In general, around 3mm round spot is sufficient), the electrode is polished against the slurry and lastly the alumina particles are cleaned off the electrode using distilled water.

After cleaning, 20 μL of the ink is released via the micropipette to the electrode without spreading it on the ring, and then dried for at least 45 minutes in controlled condition with the presence of Ethanol by applying Nitrogen.

2.2.2.2.3 Preparation of Spray Coating

Since an ink solution with higher viscosity is essential for spray coating, the amount of Nafion added to the mix is considerably lower compared to the previous protocol. As distinct from Protocol A, 90 mg of each MnO_2 and C65 are dissolved in a mix of 7.5 mL of EtOH, 7.5 mL H2O (Millipore water), and 400 mg Nafion solution (5 wt. % in the mixture). Again, after 10 minutes of stirring, the solution is sonicated for 1-2 minutes and kept under stirring till its disposal.

Lastly, the ink is sprayed on a CP at 80 °C by using a home-fabricated spray gun, and then the samples are dried under vacuum at 100 °C for 16 hours.

2.3 Raman Spectroscopy

The vibrational structure of MnO_2 and related compounds provides useful information about the crystalline structure and its modifications brought about by electrochemical conditions. This kind of information can be readily obtained by Raman spectroscopy, that measures inelastically scattered light, conveying information on the vibrational modes activated by the light delivered to the sample by a monochromatic source, typically a laser.

Specifically, regarding light scattering from a molecular system, two different types can be identified: Rayleigh scattering and Raman scattering. Rayleigh scattering is an elastic scattering phenomenon in which a photon bounces off a molecule like a billiard ball, returning with the same energy as it entered. The second form of scattering, Raman scattering, is an inelastic scattering mechanism in which the light scattered by a molecule has a slightly different energy (more or less) than the incident light.

Raman scattering is more difficult to detect than Rayleigh scattering due to its notably lower intensity. Regardless, the development of technologies such as lasers and sensitive charge coupled device (CCD) detectors has allowed Raman scattering to become the most general measurement technique known as Raman spectroscopy.

This technique is based on the fact that Raman scattered light from a given molecule in a sample will have various frequency shifts that correspond to the molecule's various vibrational modes. Since these frequency shifts depend on the chemical bonds and symmetry of the molecule, they correspond to a particular molecular structure. As a result, Raman spectroscopy has come to be regarded as a powerful investigative tool able to provide “optical fingerprints” that can be used to identify molecules. [36]

2.3.1 Raman Scattering

Raman effect can be identified by comparison with infrared spectroscopy as shown in Figure 2.10. During infrared absorption, a molecule exciting from a ground state (M) to a vibrationally excited state (M*) by absorption of an infrared photon with energy equal to the difference between the energies of the ground and the excited states.

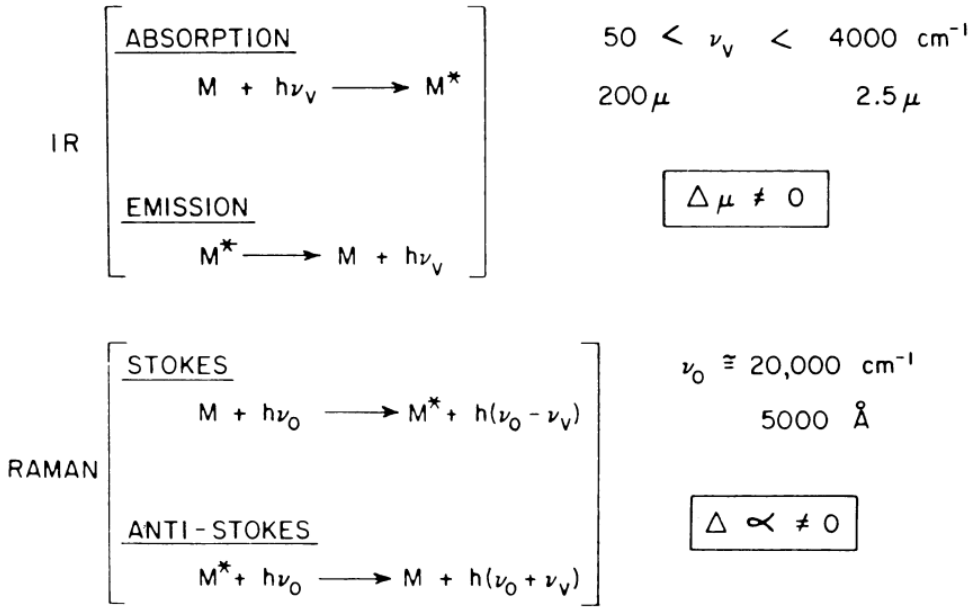

Figure 2.10. A comparison of infrared and Raman phenomena; μ = dipole moment, α = polarizability, υ_v = vibrational frequency, υ_0 = exciting frequency.

In infrared spectroscopy, we can derive information by measuring the frequencies of infrared photons that a molecule absorbs and explicating these frequencies in terms of the characteristic vibrational motions of the molecule.

For Raman activity, the major difference is that photons are not absorbed or emitted but rather shifted in frequency by an amount corresponding to the energy of the particular vibrational transition. It should be also noted that, in the Raman process, a change of transition is in the polarizability of the molecule, while it is in the molecular dipole for the infrared process.

In the Stokes process, which corresponds to absorption, the scattered photons are shifted to lower frequencies as the molecules abstract energy from the exciting photons; in the anti-Stokes process, which corresponds to emission, the scattered photons are shifted to higher frequencies as they gather up the energy released by the molecules reach back to the ground state. Furthermore, a significant proportion of the scattered photons are not frequency shifted.

2.3.2 Raman Spectroscopy

As shown in Figure 2.11, a Raman spectrometer consists of the following basic components: (1) an excitation source, generally a laser; (2) optics for sample illumination; (3) a double or triple monochromator; and (4) a signal processing system consisting of a detector, an amplifier, and an output device.

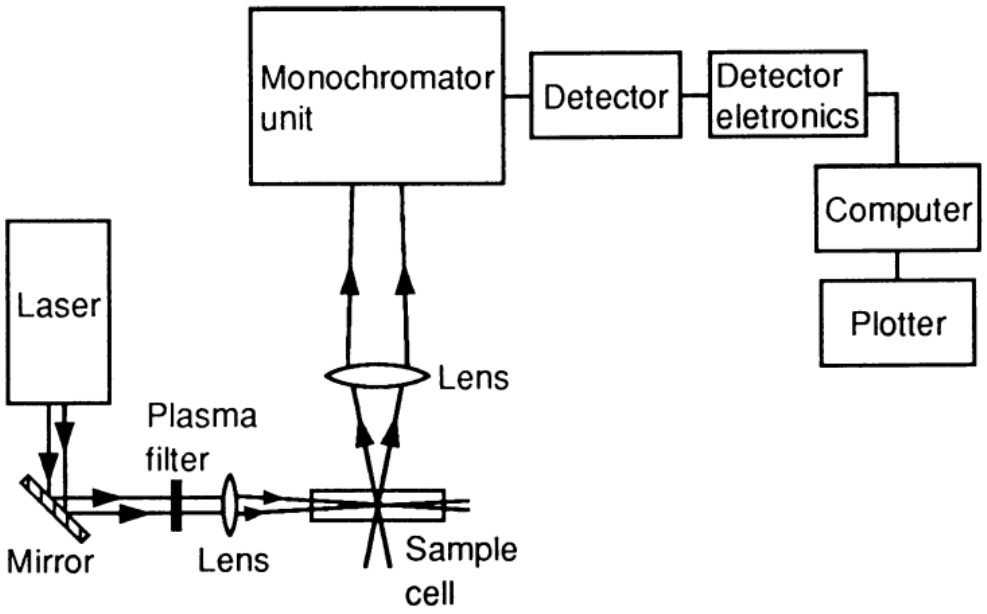

Figure 2.11. Schematic of a laser Raman system.

A sample is placed in the sample chamber, and laser light is focused on it using a lens. Liquids and solids are usually sampled in a Pyrex capillary tube. The scattered light is captured by another lens and directed at the monochromator entrance slit. Slit widths on monochromators are adjusted to achieve the desired spectral resolution. Stray light is effectively rejected by the monochromator, which also acts as a dispersing element for incoming radiation. The light that exits the monochromator exit slit is captured and focused on the surface of a detector. Inside the detector, this optical signal is transformed to an electrical signal, which is then manipulated using detector electronics. For each predetermined frequency interval, such a signal is stored in computer memory.

A Raman spectrum is a plot of signal intensity versus wavenumber (Figure 2.12). A Raman spectrum is provided by exposing a sample to a monochromatic source of exciting photons and measuring the frequencies of the scattered light. Since the Raman scattered component has a much lower intensity than the Rayleigh scattered component as explained before, a highly selective monochromator and a very sensitive detector are necessary.

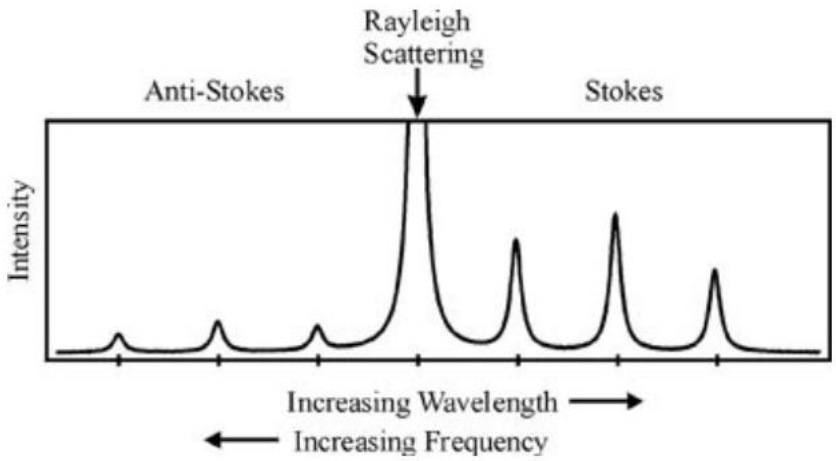

Figure 2.12. The simulation of a Raman spectrum.

For Raman analyses, we prepared our first batch of samples consisting of 5 spray-coated electrodes (one of them is a pristine sample), which are subjected to different Potentiostatic experiments (see Table 2.2). In a three electrode cell, the reference electrode was a commercial silver/silver chloride (Ag/AgCl), and the counter electrode was Pt wire electrode.

All Raman measurements were obtained using a Jobin Yvon Horiba LabRam confocal system. A 10× objective was used and the excitation at 633 nm was provided by a He–Ne laser, delivering 7 mW at the sample surface. Raman spectra were acquired with a 600 grid/mm spectrometer. The recorded Raman intensities are proportional to the discharge current of the CCD detector.

Table 2.2. The list of first batch of spray-coated samples sent for Raman Analyses.

Sample code	**Potentials Applied [V]**	**Solution**	**Preparation method**	**Number of PS Applied**
CP7	0.1	0.1 M Na2SO4	Spray coating on CP	1
CP8	0.1, 0.9	0.1 M Na2SO4	Spray coating on CP	2
CP9	0.1	0.1 M Na2SO4 +0.1 M ZnSO4	Spray coating on CP	1
CP10	0.1, 0.9	0.1 M Na2SO4 +0.1 M ZnSO4	Spray coating on CP	2

2.4 X-Ray Diffraction

X-ray diffraction (XRD) is a critical non-destructive method for analyzing various types of matter, from fluids to powders and crystals. XRD is an essential technology for materials characterization in all stages of research, production, and engineering.

XRD techniques are used to identify crystalline phases in various materials and to do quantitative phase analysis after the identification. In revealing the three-dimensional atomic structure of crystalline solids, XRD techniques are rather useful. The properties and functions of materials largely depend on the crystal structures. As a result, XRD techniques have become widely employed as a vital tool in materials research, development, and manufacturing.

2.4.1 XRD technique and Bragg's law

X-rays are electromagnetic waves with high energies and short wavelengths. When an X-ray wave encounters some regularly spaced particles, where its wavelength is in the order of the atomic spacing for solids, then diffraction occurs. [37] The resulting interference pattern is dependent on the phases of the diffracted waves. However, due to destructive interference (the result of out of phase waves), some diffracted waves do not appear in the interference pattern. Bragg's law gives criteria for the intensity of the diffracted beam related to the angle between the diffracted beam and the solid.

Considering two parallel atomic planes within a crystal structure (A and B) as shown in Figure 2.13, the distance between two planes is given by d_{hkl}, where *h*, *k* and *l* are the Miller indices of the plane. A beam of monochromatic coherent X-rays (in-phase) with wavelength λ hits these planes under an angle θ. Two waves are scattered by atoms P and Q with the same angle θ.

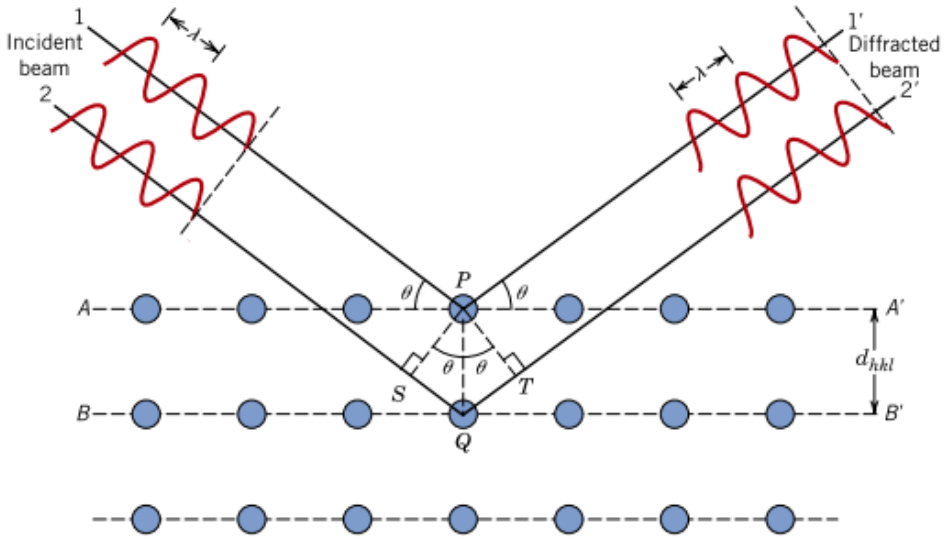

Figure 2.13. Diffraction of X-ray waves by crystallographic planes. [7]

When the diffracted waves have the same phase, they constructively interfere with one another. Therefore, the path difference between waves *1 + 1'* and *2 + 2'* should be equal to an integer number of wavelengths. The path difference is $|SQ| + |QT|$, which is equal to $2d_{hkl}\,sin(\theta)$. This result gives us Bragg's law:

$$n\lambda = 2d_{hkl}\sin(\theta)\,, \qquad for\ n \in \mathbb{N}^{+} \tag{2.8}$$

Bragg's law relates the diffraction angle to the interplanar spacing d_{hkl}. Then the equation, which relates the distance between planes with the lattice parameters a, b and c and the Miller indices h, k, and l, can be used to calculate the orientation of the plane:

$$d_{hkl} = \left(\frac{k^2}{a^2} + \frac{h^2}{b^2} + \frac{l^2}{c^2}\right)^{-1/2} \tag{2.9}$$

This particular instance of equation is valid for orthorhombic unit cells ($a \neq b \neq c$, $\alpha = \beta = \gamma = 90^\circ$). Of course, X-ray diffraction can detect in principle any long-range arrangement of atoms in a crystalline lattice, such as, e.g., a body-centered cubic crystal structure, where $h + k + l$ should be an even number and in a face-centered cubic crystal structure, where h, k, and l should all be even or odd.

2.4.2 Experimental

X-ray diffraction system (RIGAKU, SMARTLAB SE) operated at 3 kW with Cu Kβ as a radiation source was used to record XRD patters of spray coated α-MnO_2 on carbon paper samples to confirm the crystalline nature. The samples were fixed on the stage. Primary divergence slit of 10 mm and incident slit open at 20 mm on the secondary were used. The soller slit on the secondary are spaced with 2.5°. Ni filter was used to suppress the Kβ.

SmartStudio II software from Rigaku was used in order to extract the parameters of interest from measured θ-θ scans. The program is based on modern published physical theories and approaches, and takes into account the X-ray diffraction dynamical theory. Crystallographic open database (COD) is used for peak identificiation.

2.5 Scanning electron microscopy

A scanning electron microscope (SEM) is a method where an electron beam is scanned over a surface of a sample placed in vacuum chamber. The electrons from the beam are accelerated towards the surface. Under the interaction between the incident electrons and surface atoms in the sample, various signals such as secondary electrons, back-scattered electrons, auger electrons or X-ray emissions (Fig. 2.14). A detector transforms the emissions into a signal which is used to create an image of the sample [38].

In this work, secondary and backscattered electrons were mainly used to image the investigated samples. The sample's composition was determined via X-ray emissions.

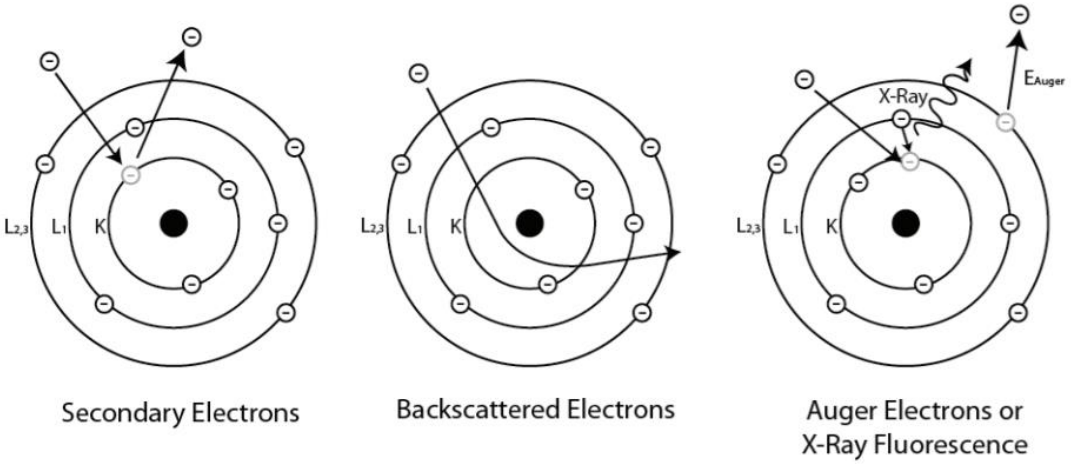

Figure 2.14 Electron atom interactions [39]

Secondary electrons

Secondary electrons (SE) are generated when an incoming electron of the electron beam interacts with the electrons of an atom in the sample. The incoming electron is scattered at the electron shell and the released energy is compensated by releasing a second electron. SE are

low-energy electrons (less than 50eV) and give information about the topography and surface variation of the sample.

Back-scattered electrons

Back-scattered electrons are high-energy electrons which are emitted when an electron from the beam is elastically scattered at the core of atom. They have a relatively high energy, reaching up to the accelerating voltage of the incoming electron beam, which increases the interaction volume compared to secondary electrons. The increased interaction volume reduces the resolution and topographic contrast. A higher atomic number leads to a more effective back-scattering, resulting in a compositional contrast that cannot be observed when secondary electrons are used. [40]

SEM observations were made on a Zeiss Supra 40 under high vacuum. The microscope is also equipped with a microanalysis apparatus for EDS elemental analysis (Oxford Instruments).

Chapter 3 Results

3.1 Electrodeposition of MnO_2 on Different Substrates

3.1.1 Introduction

In this section I describe electrodeposition of manganese dioxide (MnO_2) on CP, Platinum, and glassy carbon electrodes through an anodic electrodeposition method in order to investigate the effect of electrode material on the adhesion and electrocatalytic activity of the resulting MnO_2 thin films.

MnO_2 electrodeposition can occur on a large variety of substrates through a 2-electron oxidation reaction from Mn^{2+} cations used as precursors. The mechanism of the formation of MnO_2 thin films on a working electrode has been widely discussed, several mechanisms have been proposed, but it is difficult to define one single route because it is influenced by different factors such as the ion concentration, pH and deposition techniques. [41]–[43]

3.1.2 Electrodeposition of MnO_2 Films on Pt Electrode

3.1.2.1 Electrodeposition and Electrochemical Reduction of MnO_2 Films

Before investigating the electrochemical behavior of MnO_2 in conjunction with intercalation Zinc ions, a Pt electrode was used as a substrate for MnO_2 electrodeposition: a process that has been rather accurately described in the literature in the case of highly acidic electrolytes. [44] Figure 3.1 is representing the CV curves of Pt electrode in a $MnSO_4$/$H2SO_4$ aqueous electrolytic solution. Each of the CV cycles reported, is representing a different experiment with the same setup. We have applied potentiostatic cleaning at 0 V vs Ag/AgCl for 45 minutes after each CV. The anodic peak located in the positive potential range located between 1.0 V – 1.5 V vs. Ag/AgCl attribute to the oxidation of Mn^{2+} into Mn^{4+}, according to the following redox reaction:

$$Mn^{2+} + 2H_2O \rightarrow MnO_2 + 4H^+ + 2e^- \quad (3.1)$$

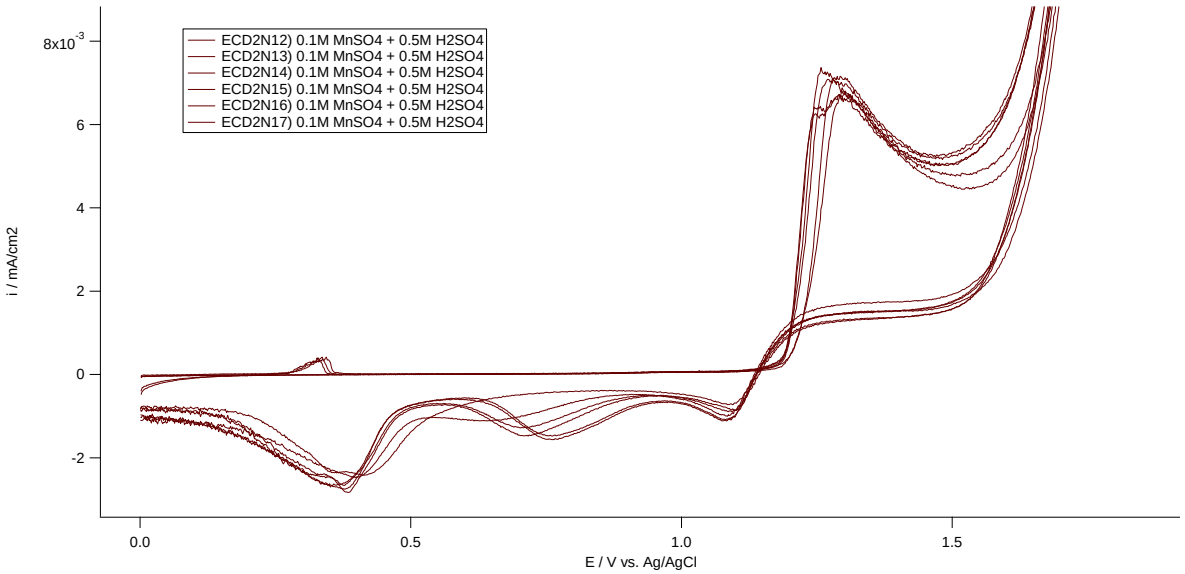

Figure 3.1 Non-consecutive cyclic voltammetry curves of MnO_2 electrodeposition and reduction on a Pt working electrode at 22°C. Electrolyte: 0.1 M $MnSO_4$ + 0.5 M H_2SO_4. Voltage range: [0 V, 1.85 V] Scan rate: 5 mV/s.

According to literature, the oxidation of Mn(II) to Mn(IV) is a multi-step anodic oxidation process, also known as an ECE mechanism [44], [45]. The formation of Mn^{3+} is the first step in this model of MnO_2 electrodeposition, as shown in reaction 3.2:

$$Mn^{2+} \rightarrow Mn^{3+} + e^{-} \tag{3.2}$$

Then it goes through a hydrolysis reaction, as shown in reaction 3.3 and 3.4:

$$Mn^{3+} + 2H_2O \rightarrow MnOOH + 3H^{+} \tag{3.3}$$

$$MnOOH \rightarrow MnO_2 + H^{+} + e^{-} \tag{3.4}$$

Non-consecutive scans show that the setup configuration is quite reproducible. We also observed that the oxidation peak seems to be quite sharp with large increase of the current (Figure 3.1). Even if it is difficult to separate the different steps of the abovementioned ECE mechanism, two anodic peaks, which are nearly engaged with each other, might be representing the reaction 3.2 and 3.4. The presence of anodic current peaks shows that the electrode is progressively covered by manganese dioxide, which is inhibiting the current flow, since the kinetics of Mn^{2+} oxidation process has been altered by a change in the catalytic activity of the electrode substrate. Considering the high catalytic activity of Pt, oxidation of soluble Mn^{2+} on a pristine Pt surface is expected to have a low overpotential. Consequently, as the Pt disk voltage increases, Mn^{2+} becomes increasingly difficult to coexist with the electrode surface, and the current flow due to oxidation ascends significantly. After we deposited a thin layer of manganese dioxide, the catalytic activity of the substrate has been lowered, so that the current flowing due to Mn^{2+} oxidation will now be less.

MnO_2 is generally deposited on the electrode through hydrolysis reaction (Eq. 3.3) specified above. In addition, there is also another reaction mechanism called “disproportionation”, which we have one oxidation state initially for then transferring electrons to end up with two species

that are in two different oxidation states. So Mn^{3+} oxidation may also occur through this pathway to form Mn^{4+} in concentrated acid aqueous solutions and then oxidized to MnO_2, as shown in reaction 3.5 and 3.6:

$$Mn^{3+} \rightarrow Mn^{2+} + Mn^{4+} \quad (3.5)$$

$$Mn^{4+} + 2H_2O \rightarrow MnO_2 + 4H^+ \quad (3.6)$$

On the reverse scan (cathodic direction), while we are reducing MnO_2 electrochemically, a reverse two-step reduction process is believed to happen, as shown in reaction 3.7 and 3.8 below:

$$MnO_2 + H^+ + e^- \rightarrow MnOOH \quad (3.7)$$

$$MnOOH + 3H^+ + e^- \rightarrow Mn^{2+} + 2H_2O \quad (3.8)$$

In addition to the electrochemical reduction steps of deposited MnO_2 mentioned above, the following chemical reactions may also occur in acid solutions, as given in: [46]

$$MnO_2 + Mn^{2+} + 2H_2O \rightarrow 2MnOOH + 2H^+ \quad (3.9)$$

$$0.5MnO_2 + 0.5Mn^{2+} + 2H^+ \rightarrow Mn^{3+} + H_2O \quad (3.10)$$

$$MnOOH + 3H^+ \rightarrow Mn^{3+} + 2H_2O \quad (3.11)$$

The Mn^{3+} ions generated by the chemical reactions 3.10 and 3.11 may be reduced to Mn^{2+} as given in reaction 3.12: [46]

$$Mn^{3+} + e^- \rightarrow Mn^{2+} \quad (3.12)$$

We can clearly observe a multi-step mechanism from the backward scan of the CV on Figure 3.1. The influence of electrode rotation on the second peak (the middle one) was examined by W.C. Maskell et al. [46], evidenced the participation of one or more solution species. The progressive increase in the second cathodic peak conveys us several distinct messages. First, the electrochemical cleaning procedure was insufficient, so we could not reduce MnO_2 deposited on the electrode completely from previous single CV measurements. Accordingly, due to larger quantities of MnO_2 remaining on the electrode surface after each CV, the overpotential for reaction 3.10 decreases while the peak current density increases. These

findings give rise to the assumption that the second cathodic peak located at 700 mV stands for reaction 3.10.

The reduction step during the third cathodic peak is believed to be the same as the first cathodic peak, which is attributed to reaction 3.13, which is the overall reaction of 3.7 and 3.8 [47]:

$$MnO_2 + 4H^+ + 2e^- \rightarrow Mn^{2+} + 2H_2O \quad (3.13)$$

3.1.2.1.1 Electrolyte Effects on Voltammetry

It is established that the second reduction peak does not appear in the absence of H_2SO_4 (Figure 3.2). A possible cause of why reaction 3.10 does not take place is that neutral aqueous solution is the low concentration of protons compared to the acidic electrolyte. Moreover, we can observe anodic peak on Figure 3.3, which appears in a potential range more cathodic than the one corresponding to Mn^{2+} oxidation on Figure 3.1. So, we can attribute this oxidation potential to MnO_2 electrodeposition possibly shifted because of a pH effect (see equation 3.1). We will look more closely at this alteration of the oxidation reaction later in this section.

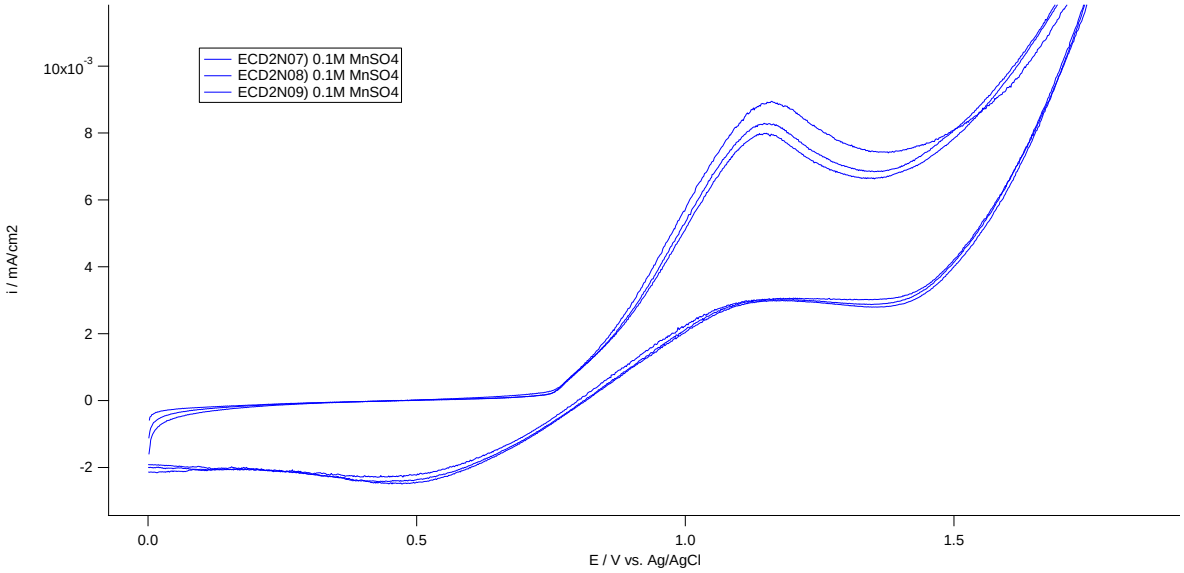

Figure 3.2 Non-consecutive cyclic voltammetry curves of MnO_2 electrodeposition and reduction on a Pt working electrode at 22°C. Electrolyte: 0.1 M $MnSO_4$. Voltage range: [0 V, 1.85 V] Scan rate: 5 mV/s.

The increase in the second reduction peak could be also observed with presence of ZnSO4 in the bulk solution at room temperature. (Figure 3.3)

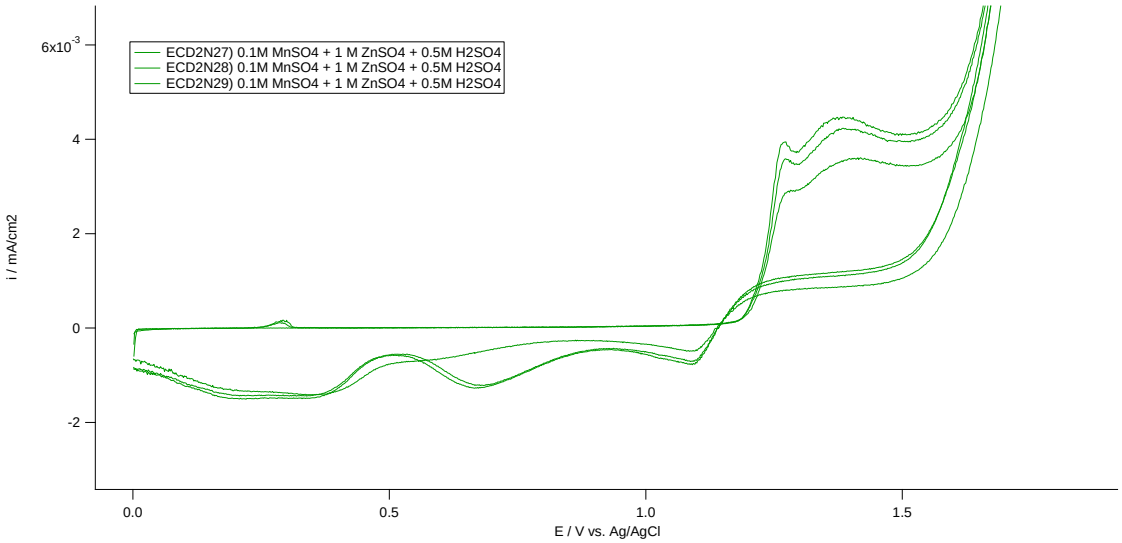

Figure 3.3 Non-consecutive cyclic voltammetry curves of MnO_2 electrodeposition and reduction on a Pt working electrode at 22°C. Electrolyte: 0.1 M $MnSO_4$ + 1 M $ZnSO_4$ + 0.5 M H_2SO_4. Voltage range: [0 V, 1.85 V] Scan rate: 5 mV/s.

To demonstrate the effects of varying the acid concentration on the electrodeposition and reduction of MnO_2 films, we continued to perform single CV scans (non-consecutive scans) using the potential range situated between 0 and 1.85 V vs. Ag/AgCl, the sulphuric acid concentration was varied as follows: 0.1 M, 0.5 M (The previous results from Figure 3.1 and Figure 3.3 are included) and without H2SO4 in the aqueous electrolytic solution, and all the results are superimposed as shown in Figure 3.4.

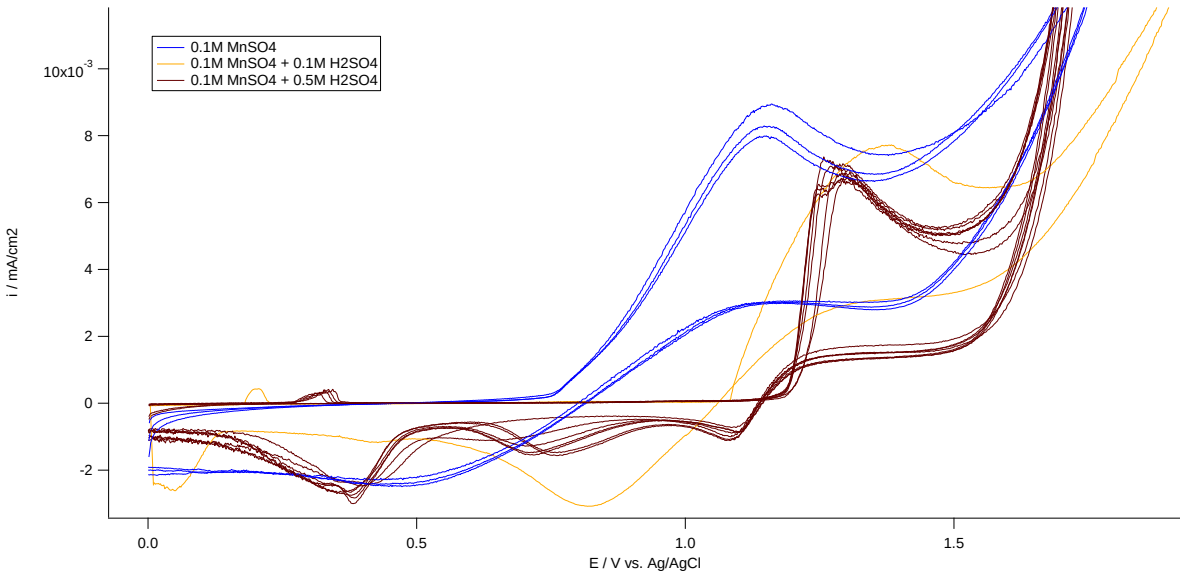

Figure 3.4 Cyclic voltammetry curve of MnO_2 electrodeposition and reduction on a Pt working electrode at room temperature. Electrolyte solutions: blue) 0.1 M $MnSO_4$, yellow) 0.1 M $MnSO_4$ + 0.1 M H_2SO_4, and dark red) 0.1 M $MnSO_4$ + 0.5 M H_2SO_4. Voltage range: [0 V, 1.85 V] Scan rate: 5 mV/s.

During the anodic-going scan, the onset and appearance of the oxidation peak is altered with H_2SO_4 concentration. In dilute H_2SO_4 (0.1 M) the peak appears suddenly and then increases slowly resulting in a broad anodic peak. As previously discussed, there are two overlapping anodic processes in these superimposed voltammograms. A sharper peak appears for more concentrated H_2SO_4 (0.5 M). These changes are occurring due to the behavior of Mn^{3+}

intermediate, which is an oxidation product of Mn^{2+}, which was claimed by Colin J. Clarke et al. [42]. We could observe a sigmoidal current for the initial part of the voltage scan, due to the higher stability of soluble Mn^{3+} in the more acidic electrolyte (0.5 M H_2SO_4). Since the lifetime of Mn^{3+} as the oxidation product is getting shorter with more dilute solution, Mn^{3+} hydrolysis occurs quickly. Consequently, MnOOH or manganese dioxide can be more easily deposited onto the electrode surface in 0.1 M H_2SO_4 solution, where MnOOH is expected to be the predominant solid phase formed in, rather than MnO_2.

Furthermore, it is obvious that increasing acidity inhibits oxidation. This cathodic shift can be computed via Nernst equation, which gives the relation between the electrolyte pH with the redox potential:

$$E_{(MnO_2/Mn^{2+})} = E^o{}_{(MnO_2/Mn^{2+})} + \frac{2.3RT}{zF}\log\frac{(a_{H^+})^4}{a_{Mn^{2+}}} \tag{3.14}$$

Where $E_{(MnO_2/Mn^{2+})}$ and $E^o{}_{(MnO_2/Mn^{2+})}$ are the redox potential and the standard potential for MnO_2/Mn^{2+} redox couple, a_{H^+} and $a_{Mn^{2+}}$ are the chemical activities of the H^+ and Mn^{2+} ions respectively, F is the Faraday constant, z is the number of transferred electrons in the redox half-reaction. Since $Mn^{2+} \rightarrow MnO_2$ is a two-electron reaction, the value of z is 2; 2.3RT/F=0.059, then equation 3.14 has the following form:

$$\begin{aligned} E_{(MnO_2/Mn^{2+})} &= E^o{}_{(MnO_2/Mn^{2+})} + \frac{0.059}{2}\log\frac{(a_{H^+})^4}{a_{Mn^{2+}}} \\ &= E^o{}_{(MnO_2/Mn^{2+})} + \frac{0.059}{2}(\log(a_{H^+})^4 - \log a_{Mn^{2+}}) \end{aligned} \tag{3.15}$$

By considering that:

$$pH = -\log a_{H^+} \tag{3.16}$$

This equation 3.15 can be written as:

$$E_{(MnO_2/Mn^{2+})} = E^o{}_{(MnO_2/Mn^{2+})} - \frac{0.059}{2}\log a_{Mn^{2+}} - 0.118pH \tag{3.17}$$

This means that the higher the pH of an electrolyte containing a given Mn^{2+} concentration, a lower potential is required for the reaction to proceed. Figure 3.4 shows that the oxidation potential onset moved to higher potentials (around 300 mV) when the acid concentration is raised from zero to 0.1 M. This large change can be a clue of different deposition mechanisms for MnO_2, as previously discussed. It is seen that the anodic peak current density is independent of the acid concentration, what was also found by Rodrigues et al. [41].

The acid concentration in the electrolyte has a large influence on the reduction of deposited MnO_2. When the acid concentration was reduced from 0.1 M to zero, the cathodic reduction

potential increased by 370 mV. The cathodic shift in the first peak may be caused by reducing mass transfer of protons to the interface electrode surface/deposit. We could also observe that the peak current density for the first reduction peak increased when H_2SO_4 concentration is lowered. This observation indicates that larger quantities of MnO_2 were formed when the acidity was reduced. We did not reduce all the deposited MnO_2 at the end of cathodic scan because some black/dark brown deposit was still visible. We could examine that acid strength has a recognizable effect on the reduction process of MnO_2.

During the cathodic voltage sweep, a plateau in current is always recorded at a lower value than that obtained with the anodic sweep, which can be attributed to a decrease in the catalytic activity of the electrode surface, after it has been covered with deposited MnO_2.

We also performed the same experiments with $ZnSO_4$ present in both neutral and acidic electrolyte at room temperature (Figure 3.5 and 3.6). Based on our observations, the oxidation current density is significantly reduced while onset potentials of first anodic peaks remain constant in both solutions. The oxidation peak is decreased by about 160 mV, while the reduction peak is shifted 130 mV in cathodic direction. Furthermore, no additional current peak was found on both anodic and cathodic sweeps in the neutral electrolyte, indicating that the electrochemical oxidation and reduction mechanisms can be reversed, though with a rather high overvoltage (Figure 3.5).

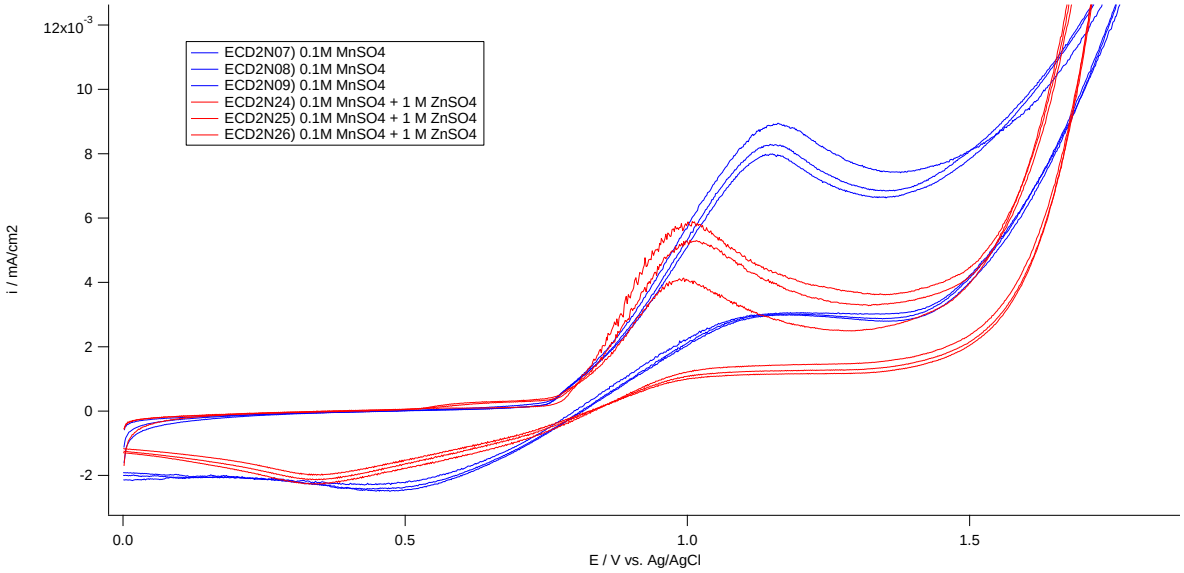

Figure 3.5 Cyclic voltammetry curve of MnO_2 electrodeposition and reduction on a Pt working electrode at room temperature. Electrolyte solutions: blue) 0.1 M $MnSO_4$, red) 0.1 M $MnSO_4$ + 1 M $ZnSO_4$. Voltage range: [0 V, 1.85 V] Scan rate: 5 mV/s.

It is significantly easier to see two distinct anodic current peaks in the acidic solution, which is coherent with the previously reported multistep electrodeposition mechanism. On the contrary, the first two reduction peaks do not appear to be affected during cathodic voltage sweep. The third reduction peak is reduced in intensity, and there is a new current shoulder formation between 0 and 0.25V vs Ag/AgCl. Following the current values for the first and second anodic peaks, it is obvious that the electrodeposition in an acidic electrolyte without ZnSO4 produces much higher peak current density values (7 μAcm^{-2} for the oxidation peak and -1.1 μAcm^{-2} for the reduction peak on Figure 3.6) by comparison with those in acidic electrolyte with ZnSO4 (4 μAcm^{-2} and 0.7 μAcm^{-2} respectively on Figure 3.6). Both oxidation peaks are suppressed by the presence of Zinc ions. This implies that electrodeposition in an electrolyte without ZnSO4 is considerably easier and faster.

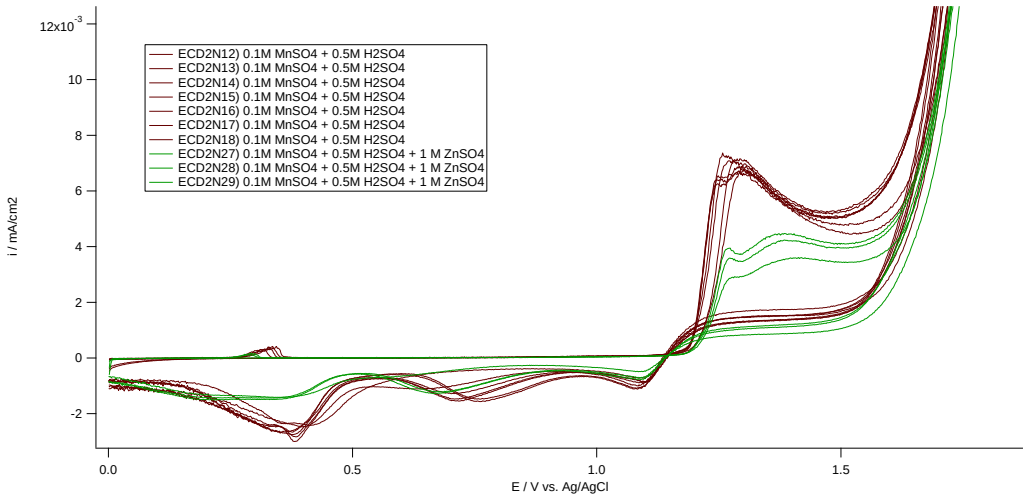

Figure 3.6 Cyclic voltammetry curve of MnO_2 electrodeposition and reduction on a Pt working electrode at room temperature. Electrolyte solutions: dark red) 0.1 M $MnSO_4$ + 0.5 M H_2SO_4, and green) 0.1 M $MnSO_4$ + 0.5 M H_2SO_4 + 1 M $ZnSO_4$. Voltage range: [0 V, 1.85 V] Scan rate: 5 mV/s.

Due to water oxidation, there was significantly more anodic charge passed than cathodic charge on all the voltammograms. These charges were calculated by subtracting the integral below the current-time curve from the CV curves previously provided from each electrolyte variation. Figure 3.7 shows representative anode:cathode charge ratios for the four different electrolytes investigated

The charge ratio increased when both Zn^{2+} and H^+ ions were added into the 0.1 M $MnSO_4$ solution separately. This is indicating that each ion has a similar impact on the charge ratio even if the electrodeposition mechanism is different for both cases. The presence of Zn^{2+} ions inhibits anodic charge in the acidic electrolyte, while we have a reverse situation in the neutral electrolyte.

In dilute or mildly acidic H_2SO_4 solutions, it was also evident that a small anodic peak formed between 0.1 V – 0.4 V vs. Ag/AgCl. This peak appeared when the electrochemical cleaning procedure was shorter than 2700 s or we observed relatively high current on the background during the potentiostatic measurement. On the contrary, there was no peak appearing on the completely cleaned electrodes. It indicates that when the cathode surface was not cleaned sufficiently, there was still residual MnO_2 present at the electrode, before performing the next non-consecutive CV measurement.

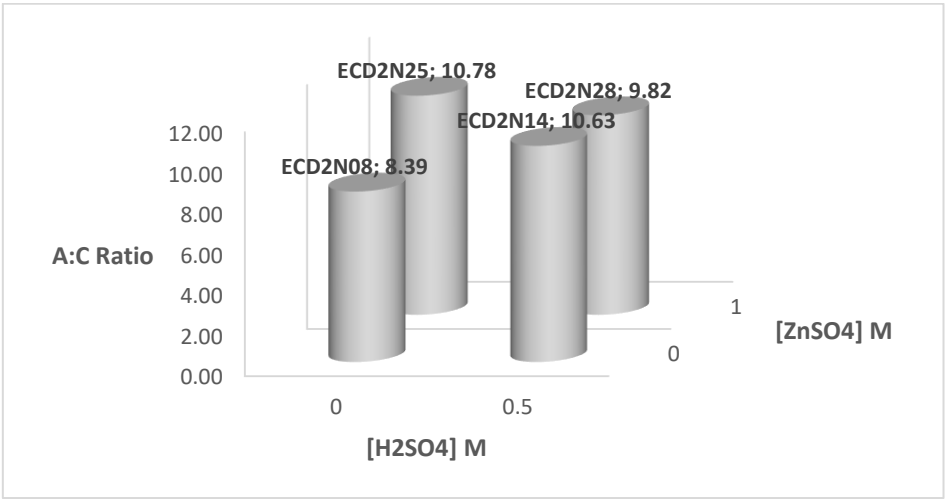

Figure 3.7 Selected anode-to-cathode charge ratio data representing 0.1 M MnSO4 with/without 0.5 M H_2SO_4 and/or 1 M $ZnSO_4$ salts in the electrolyte solution.

3.1.2.1.2 Effects of Temperature

In the previous section, we analyzed the voltammograms which were obtained in electrolytes at room temperature. In this chapter, the voltammograms presented in Figure 3.8 and 3.9 show the effects of temperature on the oxidation and reduction peaks in different electrolytes.

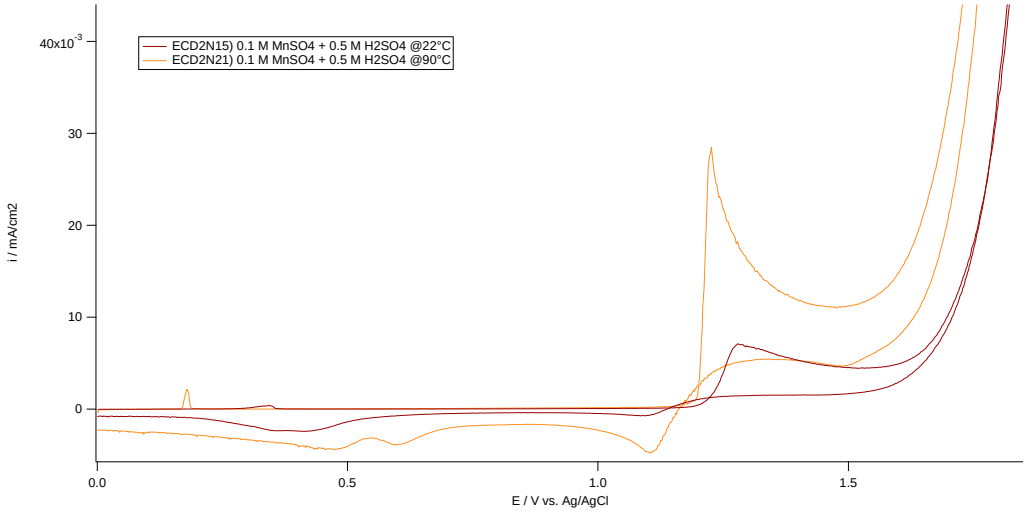

Figure 3.8 Cyclic voltammetry curve of MnO_2 electrodeposition and reduction on a Pt working electrode at 22°C and 90°C. Electrolyte solution: 0.1 M $MnSO_4$ + 0.5 M H_2SO_4 Voltage range: [0 V, 1.85 V] Scan rate: 5 mV/s.

When the temperature was increased from 22°C to 90°C, the oxidation potential was decreased by about 60 mV, and also the anodic peak current density increased drastically from 0.007 m A cm^{-2} to 0.028 m A cm^{-2} (Figure 3.8). We could also observe that increasing temperature had an impact on the deposition of MnO_2 on the anode surface, but no influence on the first reduction peak potential. A small current peak density increased and shifted in cathodic direction by increasing the temperature. A new reduction peak is formed at 0.6 V vs. Ag/AgCl at 90°C.

High temperature enhanced the oxidation rate of Mn^{2+} to MnO_2 with the presence of Zn^{2+} ions as well. (Figure 3.9).

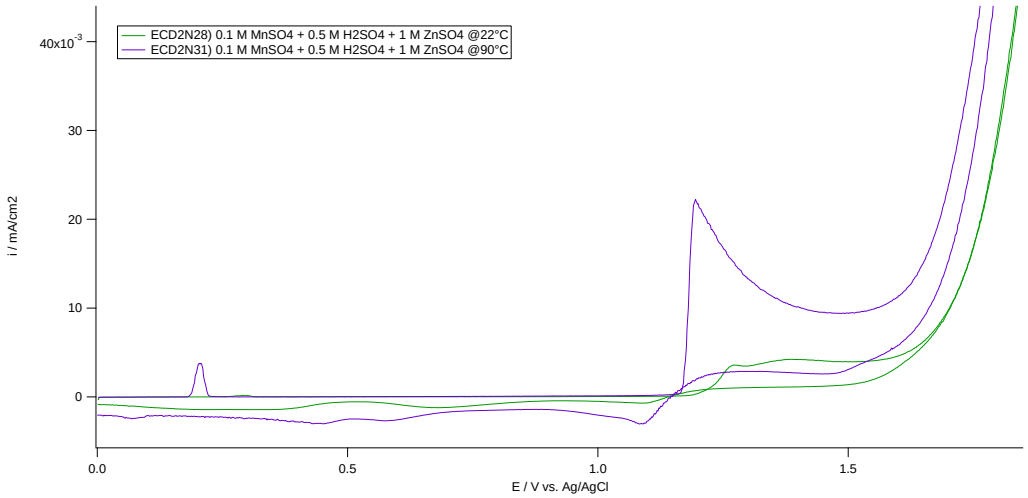

Figure 3.9 Cyclic voltammetry curve of MnO2 electrodeposition and reduction on a Pt working electrode at 22°C and 90°C. Electrolyte solution: 0.1 M $MnSO_4$ + 0.5 M H_2SO_4 + 1 M $ZnSO_4$. Voltage range: [0 V, 1.85 V]. Scan rate: 5 mV/s.

At high temperatures, the addition of Zn^{2+} ions had no significant effect either on electrodeposition or reduction process, but rather it causes a shift, which is about 20 mV, in

both anodic and cathodic peak (Figure 3.10). These observations tell us that the increased temperature enhances the oxidation rate of Mn^{2+} to MnO_2 for both setups.

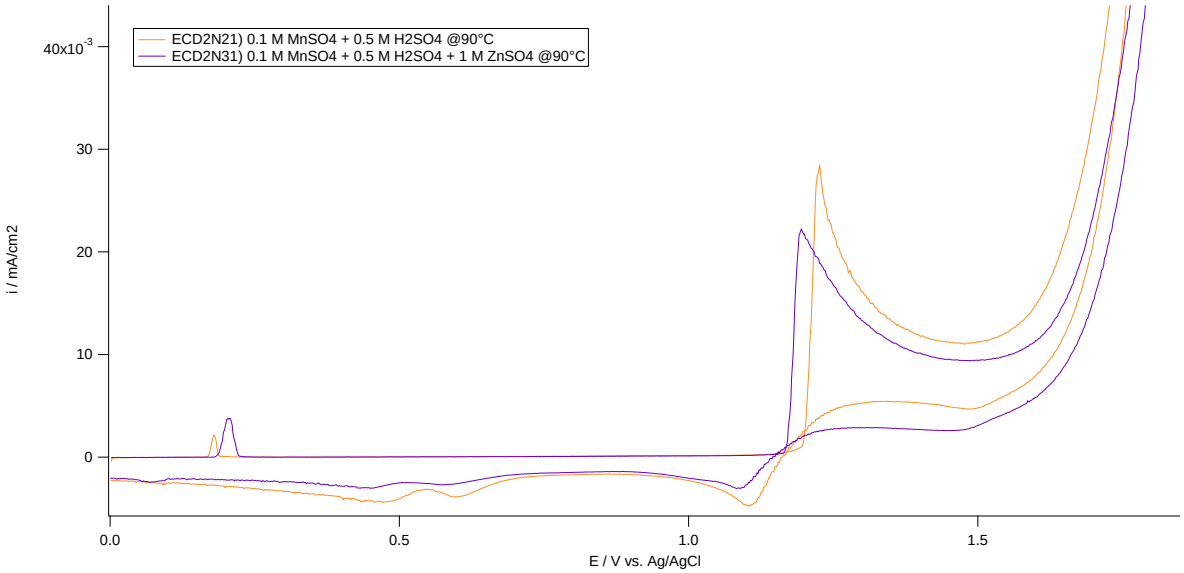

Figure 3.10 Cyclic voltammetry curve of MnO_2 electrodeposition and reduction on a Pt working electrode at 90°C. Electrolyte solutions: 0.1 M $MnSO_4$ + 0.5 M H_2SO_4 and 0.1 M $MnSO_4$ + 0.5 M H_2SO_4 + 1 M $ZnSO_4$. Voltage range: [0 V, 1.85 V vs Ag/AgCl]. Scan rate: 5 mV/s.

3.1.3 CV Testing for MnO_2 Films on Carbon Paper

In this chapter, we discuss the CV results obtained from the Section ECD1 setup configuration. CV testing of zinc metal and MnO_2@CP electrode was performed in a three-electrode cell with zinc metal as counter and reference electrodes, in various of aqueous solutions containing different salts like Na_2SO_4, $MnSO_4$, and $ZnSO_4$, using scanning rates of 0.05, 0.1, 0.5, 1 and 2 mV s^{-1}. All the measurements were performed at room temperature.

First, we observe trends on the CV results (Figure 3.11) were run in the range of 0.9 V and 1.8 $V_{Zn/Zn2+}$ (-0.1 V and 0.8 $V_{Ag/AgCl}$) at 0.5 mV s^{-1} on MnO_2@CP_0 in the aqueous solution with 0.2 M $MnSO_4$ + 2 M $ZnSO_4$ concentrations, while purging under N_2.

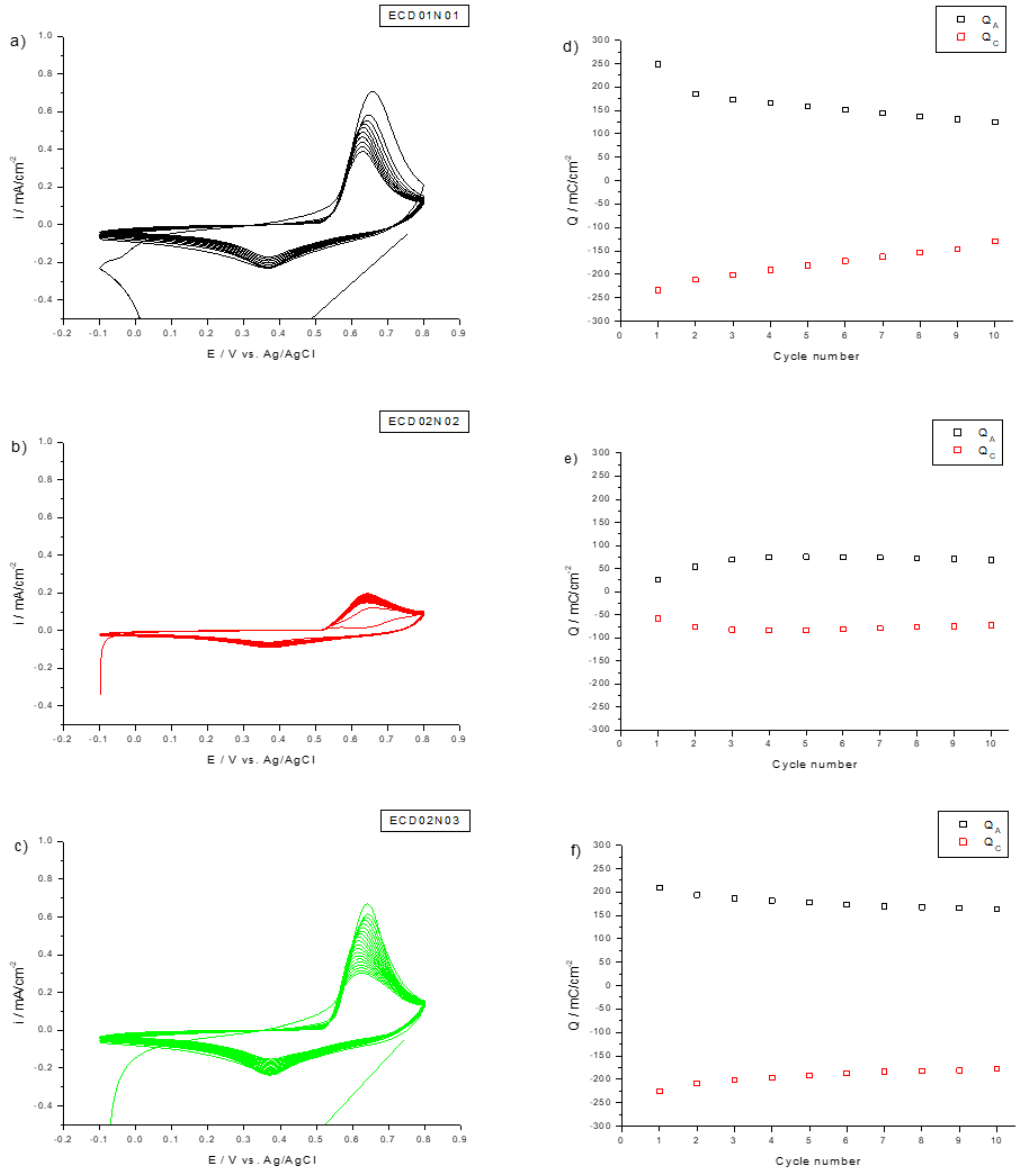

Figure 3.11 Cyclic voltammetry curves of ECD1N01 (a), ECD1N02 (b), and ECD1N03 (c), and plots of the anodic (Qa) and cathodic (Qc) coulombic charges corresponding to ECD1N01 (d), ECD1N02 (e), and ECD1N03 (f) respectively. Electrolyte: 0.2 M $MnSO_4$ + 2 M $ZnSO_4$. Voltage range: [-0.1 V, 0.8 V vs Ag/AgCl]. Scan rate: 0.5 mV/s.

ECD1N01 and ECD1N03 were the first CVs after potentiostatic electrodeposition PS1 and PS2, respectively. Their results show a progressive decrease of the peak intensity while cycling (Figure 3.12), which might indicate that progressively deposited MnO_2 is unfavorable for the electronic transportation process and thereby hinders the possible electrochemical reactions such as Zn^{2+}/H^+ insertion and extraction, because its poor electrical conductivity. On the contrary, ECD2N02 shows opposite trend. However, examining the behavior of CV alone is insufficient to reach this conclusion, so the changes on the anodic and cathodic areal coulombic charges should be also considered in this regard. The charges of the anodic peak related to oxidation, and of the cathodic peaks related to MnO_2 reduction and dissolution, were calculated for each cycle, and plotted as a function of the cycle number, as shown in Figure 3.11. Both the anodic and cathodic areal charge are decreasing gradually on ECD1N01 (Figure 3.11.d) and ECD1N03 (Figure 3.11.f). After the 6^{th} cycle, the negative slopes tend to be flattened for both charges. The charge values on ECD2N02 (Figure 3.11.e) are much lower than other two

experiments. ECD1N02 was the second CV applied after PS1, so ECD1N01 and ECD1N02 are consecutive CV experiments. Therefore, we could observe the plateaus on ECD1N02 which are continuation of the slopes on ECD1N01.

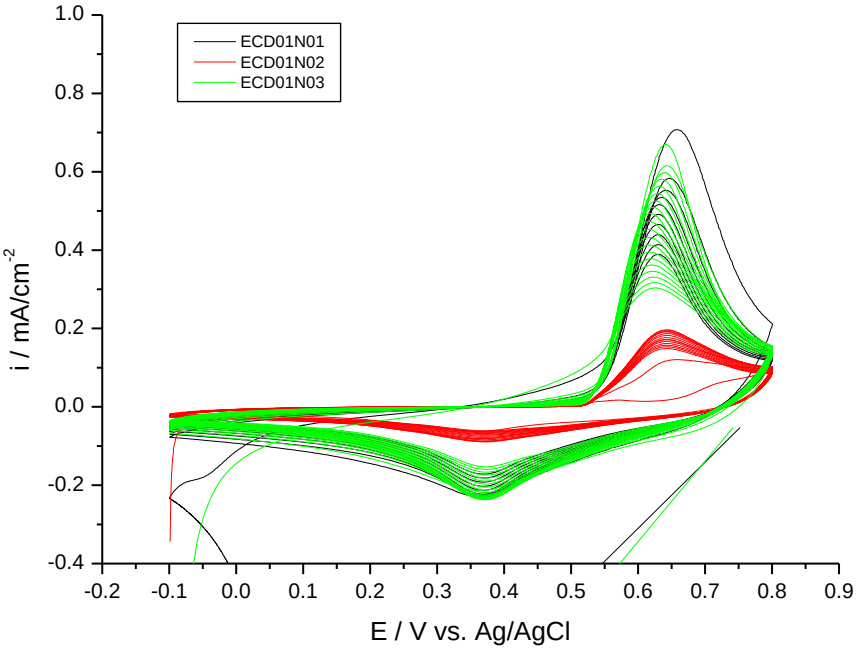

Figure 3.12 Superimposed CV curves of ECD01N01, ECD01N02, and ECD01N03 at 22°C. Electrolyte: 0.2 M $MnSO_4$ + 2 M $ZnSO_4$. Voltage range: [-0.1 V, 0.8 V vs Ag/AgCl]. Scan rate: 0.5 mV/s.

From the point of view of the anodic peak positions, ECD1N01 and ECD2N03 are comparable. Nevertheless, ECD2N02 shows a shifted peak towards higher voltages. It should be noted that if two different substrates are used and deposition occurs at different potentials, the deposition at higher voltage is inhibited (it requires more energy). As a result, carbon paper has a lower catalytic activity than MnO_2. So, it can be linked to a deposition on a clean piece of carbon paper, which will be corroborated later also by a comparison with LSV results on glassy carbon electrodes. After some cycles, the anodic peak returns to the same position as ECD1N01 and ECD2N03. All the curves show the same cathodic peak position (Figure 3.12). ECD02N02 has lower anodic and cathodic peak current density.

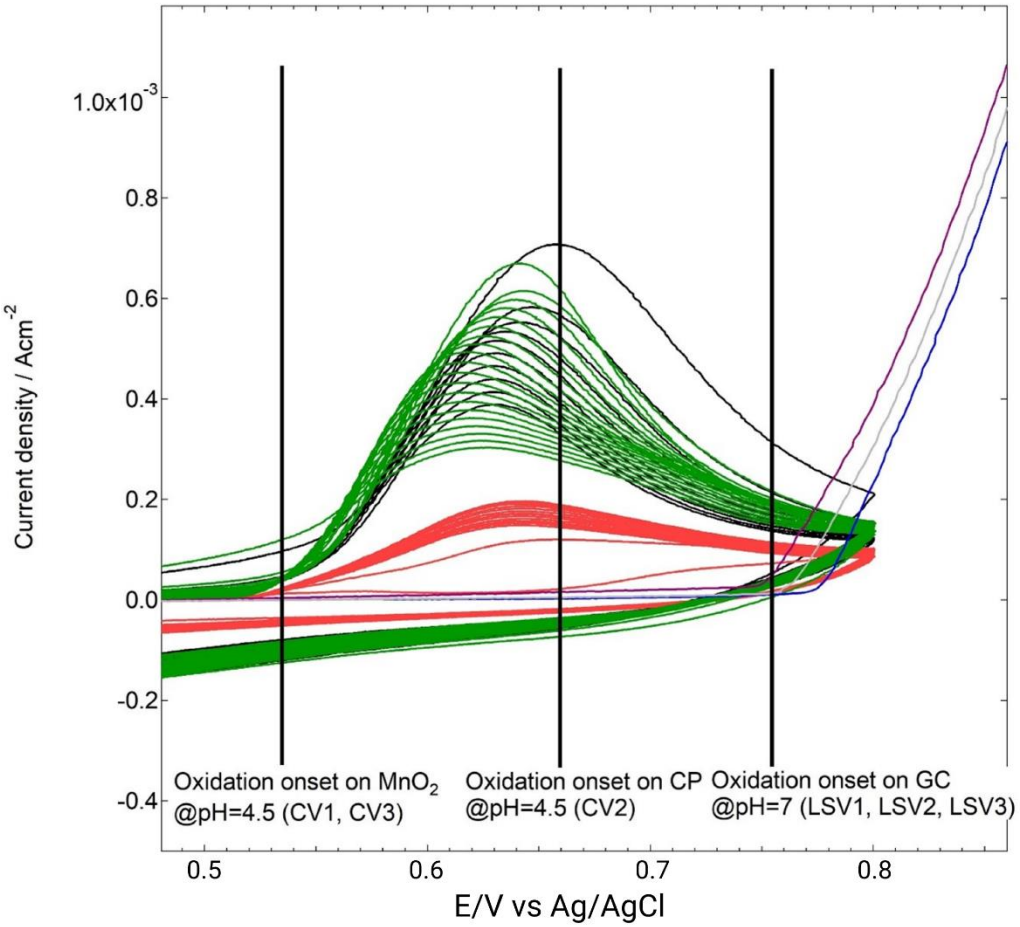

Figure 3.13 LSV curves on a glassy carbon electrode superimposed with CV measurements from Figure 3.11. Electrolyte: 0.1 M $MnSO_4$. Scan rate: 0.5 mV/s

In figure 3.13, we superimposed the LSV data from the RDE experiment applied on glassy carbon with CV datas on MnO_2@CP_0. We can see the effect of different pH, and the substrate. The deposition is inhibited when CP is available. It could be expected to observe the onset value at lower voltage on CP for pH=7 for the oxidation peak, so the anodic shift might be an effect of non-graphitizing structure of glassy carbon.

We focused on optimizing the working electrode by covering the back side and corners of carbon paper with Teflon paper before the electrodeposition. ECD1N04 (1st one after PS1) and ECD1N05 (2nd one after PS1) are consecutive CV. These experiments were run on MnO_2@CP_1 in the same electrolyte and electrochemical procedures with the previous sample MnO_2@CP_0.

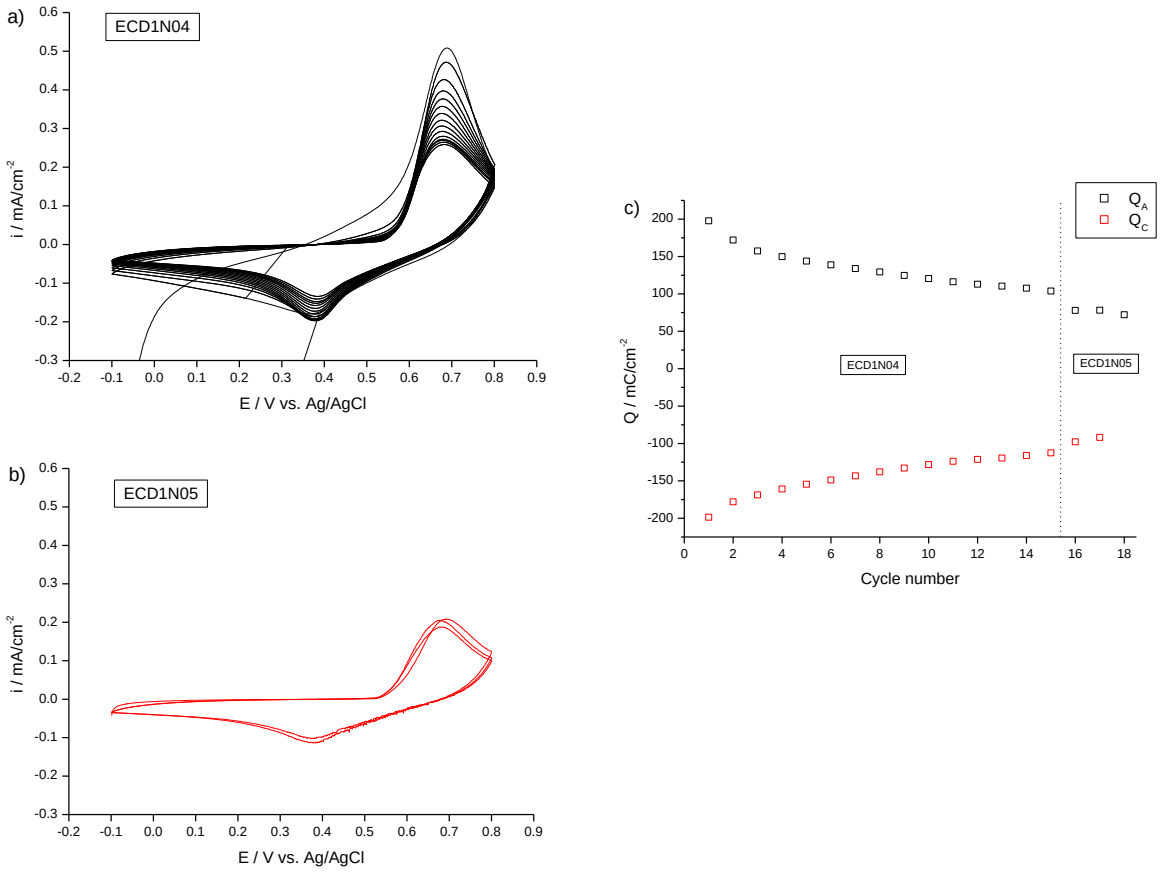

Figure 3.14 Cyclic voltammetry curves of ECD1N04 (a) and ECD1N05 (b), and plots of the anodic (Qa) and cathodic (Qc) coulombic charges corresponding to ECD1N04 and ECD1N05 (c). Electrolyte: 0.2 M $MnSO_4$ + 2 M $ZnSO_4$. Voltage range: [-0.1 V, 0.8 V vs Ag/AgCl]. Scan rate: 0.5 mV/s

Both anodic and cathodic current density peaks are in agreement with the previous CV measurements for ECD1N04 and ECD1N05 (Figure 3.14a,b). We can ignore minor differences due to the ohmic conditions. Since they are consecutive CV measurements, areal coloumbic charges are represented in the same graph (Figure 3.14c). We arrived at the following conclusions after comparing our findings to those of previous studies:

- If CV is the first one after electrochemical deposition, the anodic/cathodic charge decrease with each cycle.
- Both charges tend to stabilize in the following CVs.
- In every cycle studied so far, the cathodic charge is greater than the anodic charge.

MnO_2@CP_1 was also tested in a different electrolyte solution (2 M Na2SO4), but there was no oxidation/reduction reaction occurred on the electrode surface.

We synthesized MnO_2@CP_2 by the same electrodeposition procedure in a split cell. We applied anodic deposition 2 times (PS1 and PS2), the same as previous samples. The results are categorized by sweep rates and shown in different figures below. ECD1N06 and ECD1N07 are 3rd and 4th CV measurements after PS1, respectively. ECD1N08 is representing the 1st CV applied after PS2 (Figure 3.15,a,b,c). We were expecting to visualize two separate peaks that represents two-step reaction in both anodic- and cathodic-going scans. We could observe small

shoulder formations at 0.23 V and 0.57 vs Ag/AgCl correlatively, which are consistent with Wei Sun et al. found. [20]

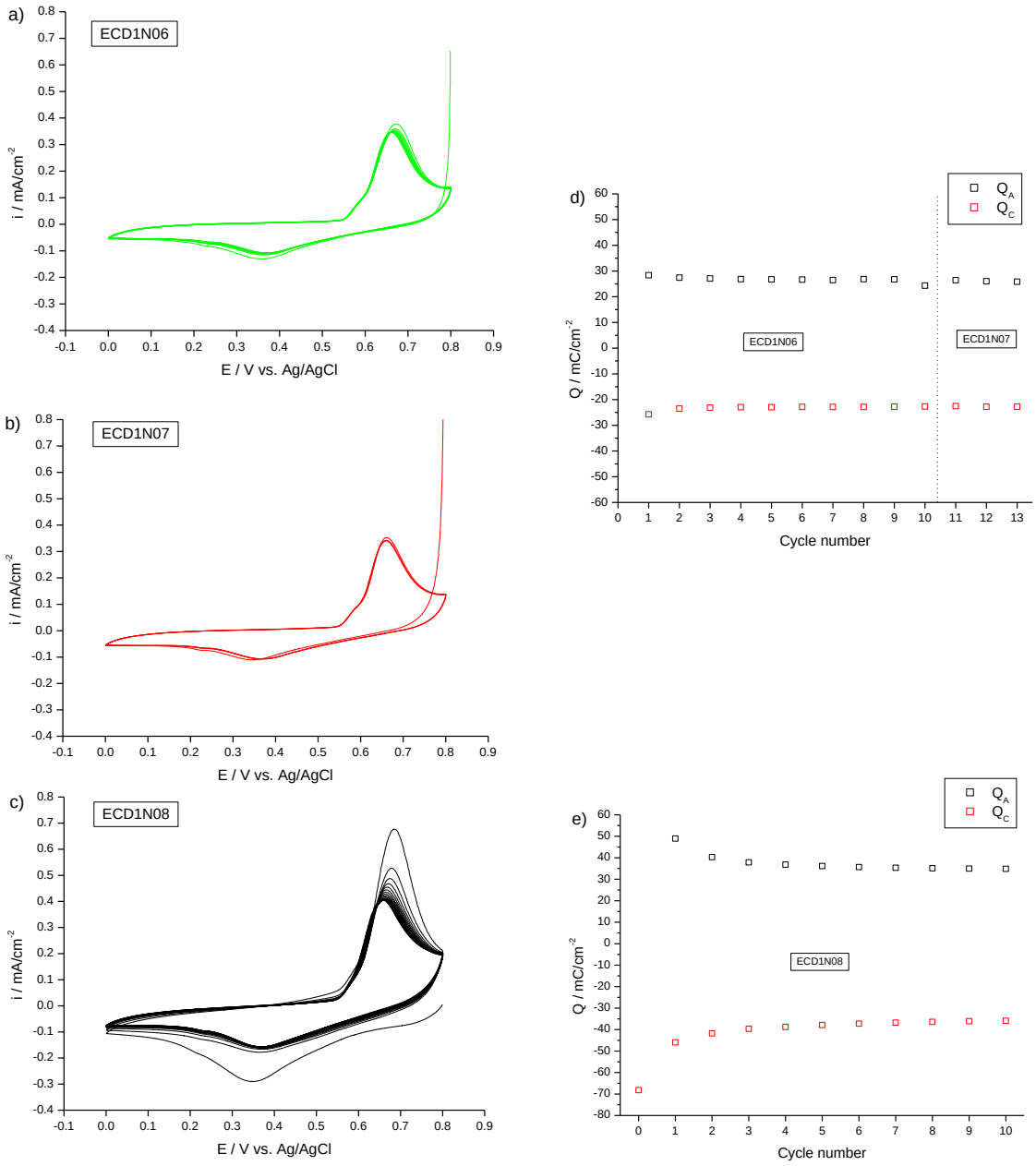

Figure 3.15 Cyclic voltammetry curves of ECD1N06 (a), ECD1N07 (b), and ECD1N08 (c) in an electrochemically split cell, and plots of the anodic (Qa) and cathodic (Qc) coulombic charges corresponding to ECD1N06 and ECD1N07 (d), and ECD1N08 (e). Electrolyte: 0.2 M $MnSO_4$ + 2 M $ZnSO_4$. Voltage range: [0 V, 0.8 V vs Ag/AgCl]. Scan rate: 2 mV/s.

ECD1N06 and ECD1N07 are consecutive tests as previously mentioned. It is readily apparent that both reach the same anodic and cathodic charge values +26 mC/cm^{-2} and -22.5 mC/cm^{-2} respectively (Figure 3.15,d), which tells us that global charges tend to stay constant after cycling. Each cycle is predominantly with a positive charge, in other words the active material is progressively accumulates on the electrode surface.

On the contrary, ECD1N08 starts with a cathodic charge (around -70 mC/cm^{-2}) relatively higher than the following cycles in the same CV. We could observe positive global charge values around 30th cycle (Q_A=35.9 mC/cm^{-2} and Q_C=-35.27 mC/cm^{-2}), as a result of slow descending

cathodic charge and ascending anodic charge after each cycle. But it is not shown on Figure 3.15, as we only graphed the first 10th cycles for each CV. In conclusion, the pristine MnO_2 (after PS) is more catalytic for the reduction of the active material. During the CV measurements, we are discharging the active material at cathodic sweep, which allows the coinsertion of H^+ and Zn^{2+} ions through the deposited MnO_2. [20] This sequential redox reaction increases reproducibility in a split cell, which is quite faster to be reached than in three electrode cell setup applications.

ECD1N09 and ECD1N10 were run at a lower sweep rate 0.5 mV/s. As presented in Figure 3.16,a,b, with the decrease in CV sweep rate, the cathodic peak at high voltage remain obvious whereas the cathodic shoulder at low voltage gradually increase. It appears that we allow slow kinetic reactions to happen by lowering the sweep rate. ECD1N10 is 2nd CV after PS1 (after ECD1N08). When we compare charge values for ECD1N08 (Figure 3.15,e) and ECD1N10 (Figure 3.16,d), we observed that the anodic charge stays constant, while the cathodic one gradually decreases. At lower scan rate, we also observe higher offset between anodic and cathodic charges, so we readily obtain positive global charges at the first cycles of ECD1N09 and ECD1N10.

ECD1N11, ECD1N12 and ECD1N13 were run at even a lower sweep rate 0.05 mV/s. They are 3rd , 4th, and 5th consecutive CVs after PS2, respectively. When the scan rate was reduced from 2 mV/s to 0.5 mV/s, and then to 0.05 mV/s, the oxidation peak moved to lower oxidation potentials (around 100 mV) and became sharper as can be seen from Figure 3.17. Nevertheless, the reduction peak potential is independent from the scan rate. Both anodic and cathodic current densities decreased to around 0.03 mA/cm^{-2} (Figure 3.17a,b,c) from 0.35 mA/cm^{-2} (Figure 3.15,a,b,c), when the scan rate was lowered. ECD1N11 is cycled between 0 V and 0.65 V (Figure 3.15,a) , where OER and the reduction shoulder do not appear. When we extended the voltage range from 0 V to 0.85 V, the cathodic shoulder is visible again at 0.32 V (Figure 3.17,b,c). It might indicate that limiting the OER is inhibiting the second cathodic reaction which can be attributed to Zn^{2+} insertion. The positive charge is even more predominant than negative charge during cycling at 0.05 mV/s (Average values: Q_A=149.16 mC/cm^{-2} and Q_C=-50.75 mC/cm^{-2}).

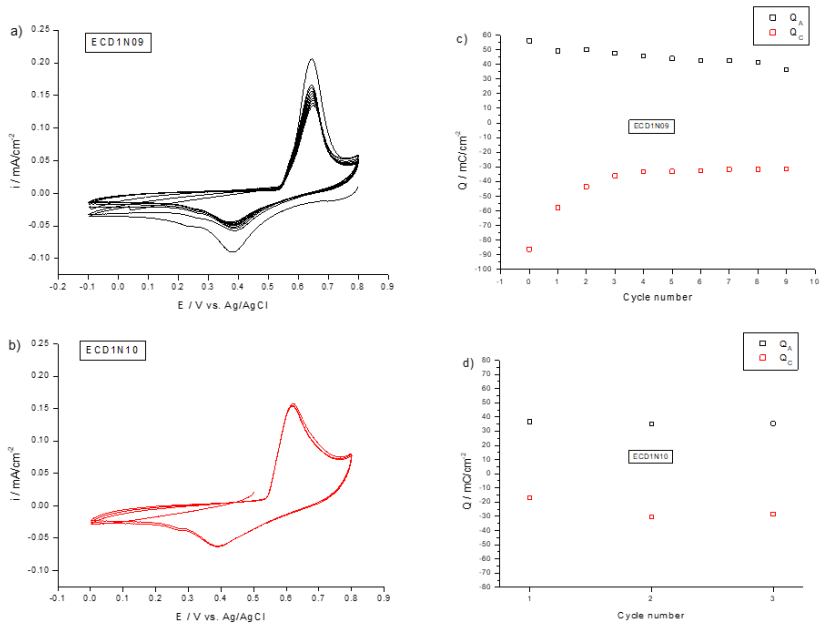

Figure 3.16 Cyclic voltammetry curves of ECD1N09 (a), and ECD1N10 (b) in an electrochemically split cell, and plots of the anodic (Qa) and cathodic (Qc) coulombic charges corresponding to ECD1N09 (c) and ECD1N10 (d). Electrolyte: 0.2 M $MnSO_4$ + 2 M $ZnSO_4$. Voltage range: [0 V, 0.8 V vs Ag/AgCl]. Scan rate: 0.5 mV/s.

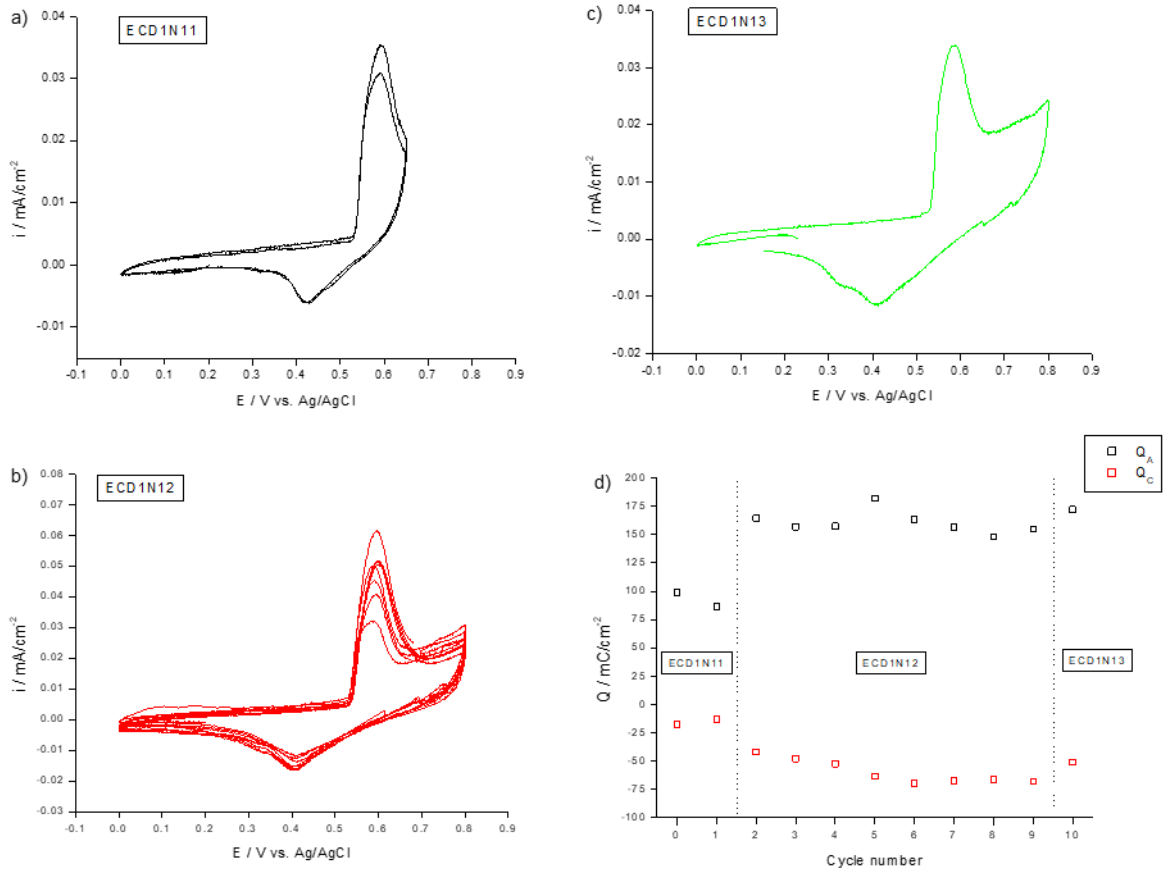

Figure 3.17 Cyclic voltammetry curves of ECD1N11 (a), ECD1N12 (b), and ECD1N13 (c) in an electrochemically split cell, and plots of the anodic (Qa) and cathodic (Qc) coulombic charges corresponding to ECD1N11, ECD1N12 and ECD1N13 (d). Electrolyte: 0.2 M $MnSO_4$ + 2 M $ZnSO_4$. Voltage range: [0 V, 0.8 V vs Ag/AgCl]. Scan rate: 0.05 mV/s.

We attempted to synthesize MnO2@CP_3 in 0.2 M MnSO4 aqueous solution by using the potentiostatic technique at 800 mV, as we had done on the previous CP samples with presence of $ZnSO_4$. However, running the the PS experiment at 800 mV the current value dropped sharply to zero right from the beginning of the measurement. Anyway, in the absence of Zn^{2+} in the solution, MnO_2 could be grown under otherwise identical conditions. In order to grow MnO_2 from the Zn^{2+}-contining bath, we switched to galvanostatic control at 0.01 mA/cm^2 for 17 hours (experiment MnO_2@CP_3). As we set a constant current value, the potential tented to be fixed around 850 mV (Figure 3.19,d). It appears that we could be able to apply PS without an issue if we change the potential value to 850 mV instead of 800 mV. Considering this shift in anodic direction, Zn^{2+} ions seem to interact with the oxidation of Mn^{2+} ions to MnO_2, somehow delaying it. This results correlated with what we obtained working with a Pt electrode (Figure 3.5).

After the electrodeposition on MnO_2@CP_3, the electrolyte was replaced with 0.5 M Na_2S0_4 and 2 M $ZnSO_4$ aqueous solutions. We rinsed both counter and working electrodes before each replacement of electrolyte solution. First, ECD1N14 was run at 1 mV/s in 0.5 M Na_2S0_4 solution, while purging under N_2. The anodic and cathodic current averages are quite high, and the voltammogram has a more rectangular shape (3.18,a).

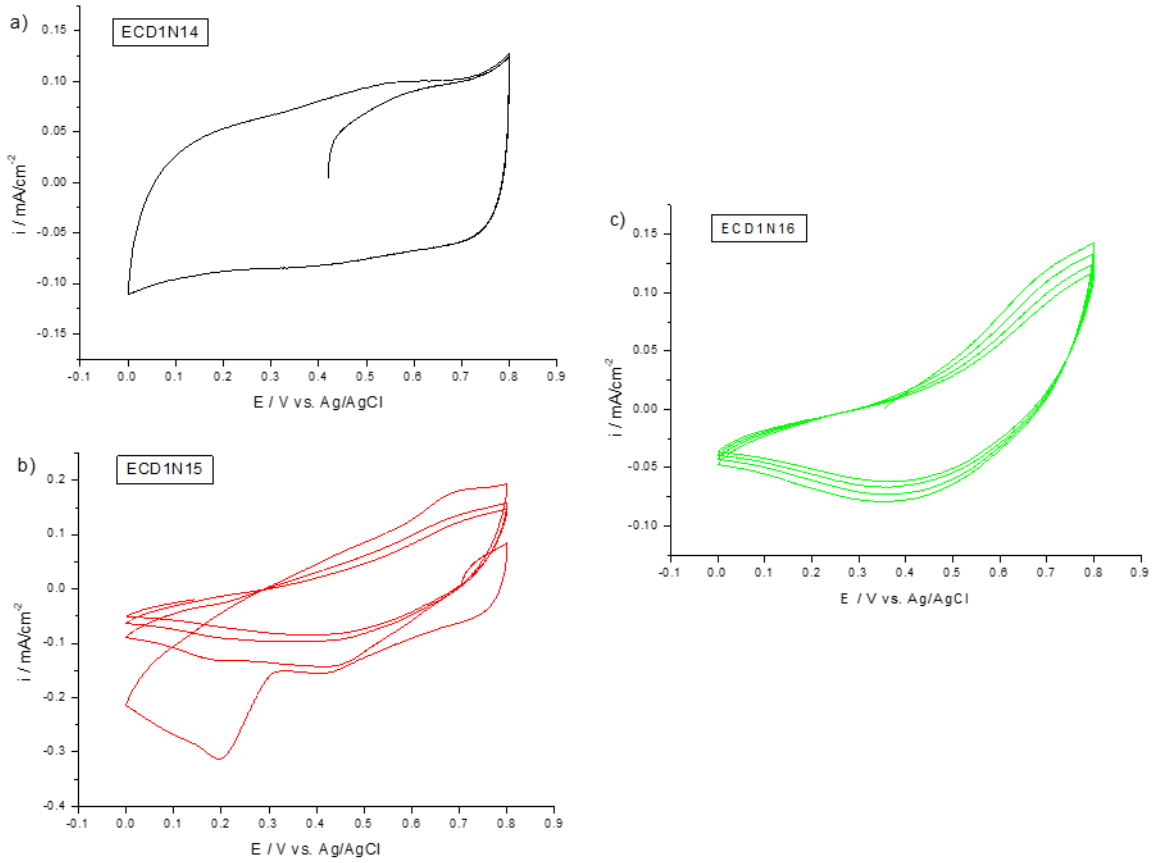

Figure 3.18 Cyclic voltammetry curves of ECD1N14 (a), ECD1N15 (b), and ECD1N16 (c) in an three electrode cell Electrolyte: 2 M Na_2SO_4 (a) , 2 M $ZnSO_4$ (b) and (c). Voltage range: [0 V, 0.8 V vs Ag/AgCl]. Scan rate: 1 mV/s.

ECD1N15 and ECD1N16 are consecutive CVs applied in 2 M $ZnSO_4$ solution. We can see two cathodic peaks with the presence of Zn^{2+} ions in the solution (3.18,b and 3.18,c). The voltages of the two cathodic peaks (200 mV and 400 mV), which corresponds to co-insertion of H^+ and Zn^{2+} ions, align with the results Wei Sun et al. obtained [18]. The second cathodic peak has relatively higher current peak at the first cycle of ECD1N15. The reason for this is unknown but note that ECD1N15 is the consecutive CV after ECD1N14. Accordingly, Na^+ pre-intercalated MnO_2 might be promoting Zn^{2+} insertion.

Under slow-sweep conditions, S. Ko et al. also proposed that their manganese oxide-decorated carbon nanostructured papers electrode exhibit capacitor-like and battery-like character in Na^+-only and Zn^{2+}-only electrolytes, respectively [48].

3.1.4 Electrodeposition of MnO_2 on Carbon Paper and Capacity Analysis

This section targets the following issues: assess the influence of cell setup and different ions on capacity, and examine capacity fading through cycling.

We can evaluate the active material loading on CP by using the Faraday constant. The Coulomb is a measure of the quantity of electricity. If a current of 1 A flows for 1 second, then 1 Coulomb of electricity has passed. By this way, we can estimate how much electricity has passed in a given time by multiplying the current in A by time in seconds.

$$\text{Number of Coulombs [C]} = \text{Current [A] x Time [s]} \tag{3.18}$$

Each electron carries 1.602 x 10^{-19}C. 1 mole of electrons contains the Avogadro constant, that is 6.022 x 10^{23} electrons. That means the 1 mole of electrons must carry:

$$6.022\ x\ 10^{23}\ x\ 1.602\ x\ 10^{-19}\ C\ = 96485\ C \tag{3.19}$$

This value is known as the Faraday constant. It is rounded off to 96500 C in our calculations. 96500 C is also called 1 faraday.

As previously shown in Formula 3.1, our electrochemical reaction consumes two moles of electrons (oxidizing from Mn^{2+} to Mn(IV)) to form one mole of MnO_2. So that,

- 2 moles of electrons give 1 mol of MnO_2.
- Therefore, 2 x 96500 C give 87 g of MnO_2.
- As we know the current we have applied to the electrode during electrodeposition and the time of current application, hence we can estimate the number of Coulombs (*NoC*) by subtracting the integral below the current(A)-time(s) line on PS&GS diagrams (Figure 3.19).

Now we can evaluate the mass loading of MnO_2 during PS and GS by the following calculation:

$$m_{MnO2} = \frac{\text{NoC x 87 g}}{\text{2 x 96500 C}}\ [\text{g}] \tag{3.20}$$

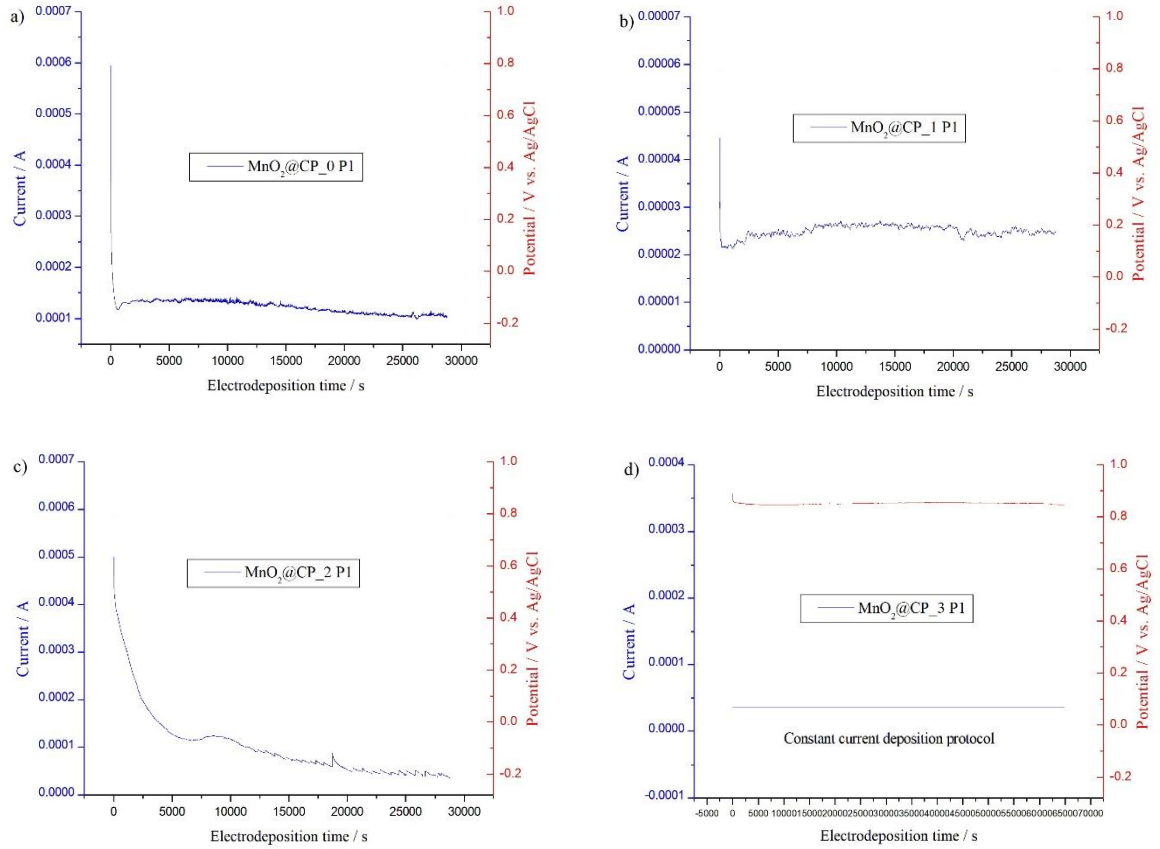

Figure 3.19 Constant potential electrodeposition (PS) of MnO_2@CP_0 (a), MnO_2@CP_1 (b), and MnO_2@CP_2 (c). Electrolyte: 0.2 M $MnSO_4$ + 2 M $ZnSO_4$. Constant current electrodeposition (GS) for MnO_2@CP_3 and Electrolyte : 0.2 M $MnSO_4$.

We evaluated the mass loading of MnO_2 per unit area for all electrodes and they are listed in Table 3.1. A comparison of MnO_2@CP_0 to MnO_2@CP_1 indicates that, deposition performed with higher current values on MnO_2@CP_0. A possible cause of this increase is electrodeposition at the unscreened back side of the electrode. We could simply avoid this by covering those areas with Teflon during the electrodeposition process. Therefore, the electrodes are optimized since the measured current represents the redox reaction more accurately. MnO_2@CP_2 has the highest loading per unit area. Our findings on MnO_2@CP_3 suggest that we can receive the same amount of loading per unit area via GS by doubling the deposition time.

Table 3.1 Loading values of MnO_2 during PS/GS for CP Electrodes

Sample no [-]	Deposition Technique [-]	Loading [g]	Loading per unit area [g/cm2]	Duration Time [h]
MnO_2@CP_0	PS	0.00159	0.000420	8
MnO_2@CP_1	PS	0.00032	0.000289	8
MnO_2@CP_2	PS	0.00132	0.000522	8
MnO_2@CP_3	GS	0.00104	0.000292	16

The specific capacities were calculated from the CV curves according to the following equation:

$$C = \frac{\int I\, dv}{2\ x\ 3600\ x\ m\ x\ v} \tag{3.21}$$

where *"∫Idv"* implies area under the CV curve, *"m"* signifies loading (g) of active material, *'v'* specifies the scan rate (mV/s), and C is specific capacity (mAh/g_{MnO2}). *"∫Idv"* also stands for the summation of anodic and cathodic charges of each cycle, as previously computed.

Three graphs in Figure 3.20, shows first, second and third CV measurements, respectively. The black, red, green and blue symbols are representing specific capacities of MnO_2@CP_0, MnO_2@CP_1, MnO_2@CP_2 and MnO_2@CP_3, respectively. It appears that CVs, which are not started from open circuit voltage, had considerably large specific capacities at their first cycle. We also added the capacities of their 2nd cycles in order to monitor the general trend accurately.

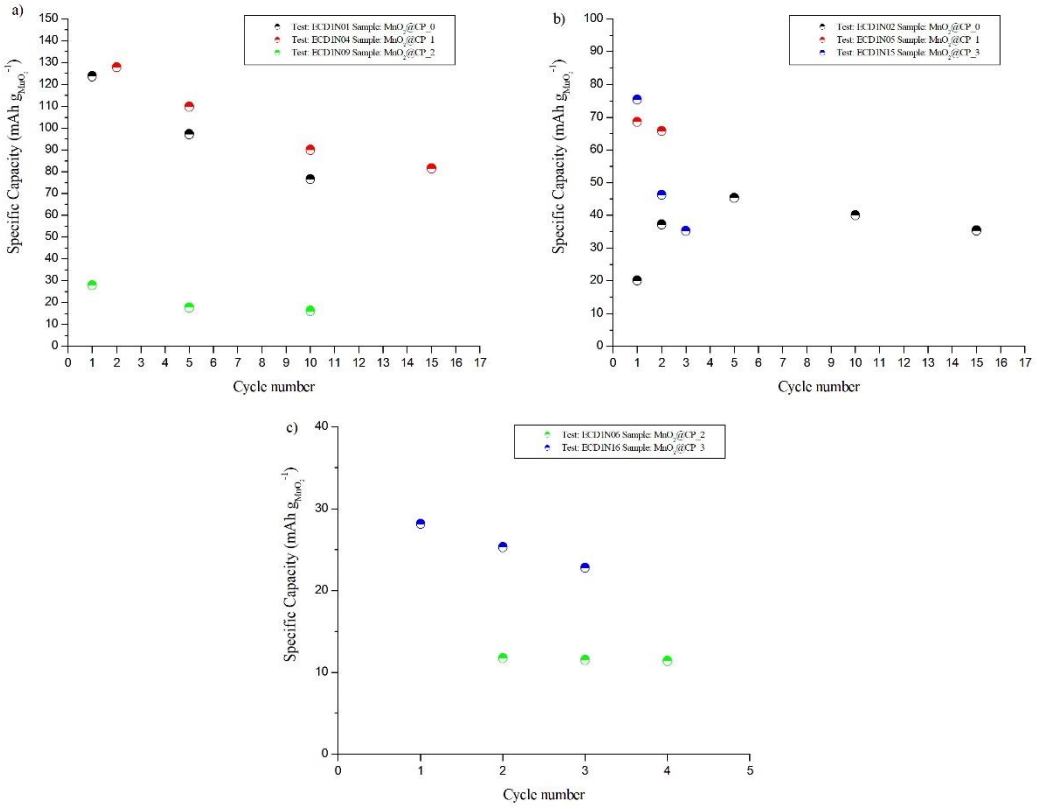

Figure 3.20 Specific capacities per cycle of 1st CVs (a), 2nd CVs (b), and 3rd CVs (c) after electrodeposition. Electrolyte for MnO_2@CP_3: 2 M $ZnSO_4$ Electrolyte for other samples: 0.2 M $MnSO_4$ + 2 M $ZnSO_4$.

We could reach the highest capacities (123.8 and 127.7 $mAhg^{-1}$) at the first cycle of ECD1N01 and ECD1N04, respectively (Figure 3.20,a). It is around 40 % of the theoretical capacity of MnO_2 (308 $mAhg^{-1}$, based on molecular weight of MnO_2 and 1 e^- transfer reaction). Contrary to our expectations due to high loading rate, capacity dropped drastically for MnO_2@CP_2. Besides having a considerably lower capacities, it has strong tendency to reach a plateau around 10 $mAhg^{-1}$ after few cycles. On the contrary, capacity is fading substantially in three electrode applications. The graphs show that capacity has tendency to decrease approximately 5 percent per cycle in the mixed $MnSO_4$:$ZnSO_4$ electrolyte (Figure 3.20,a and b). However, capacity fade increases up to 10 percent per cycle in the $ZnSO_4$-only solution (Figure 3.20,c). Together, these findings support the view that presence of Mn^{2+} ions in the electrolyte change the equilibrium

of reducing Mn^{2+} ions from the MnO_2 electrode, and thus prevent continuous Mn2+ dissolution [21] .

3.2 Electrochemical behavior of micro-wave synthesized α - MnO_2

In this section I investigated electrochemical activity of micro-wave synthesized α-MnO_2 (cryptomelane), which is drop cast on glassy carbon substrate as described in Chapter 2, by using cyclic voltammetry in alkaline and near neutral electrolytes.

Four replicated, independently synthesized, batches of ink were produced using alpha manganese dioxide, in view of a consistency check, I denominated them in the following way:

- « Ink 1»
- « Ink 2»
- « Ink 3»
- « Ink 5»

3.2.1 Cyclic Voltammetries in Alkaline Solution

Each of the CV cycles reported in this chapter, is representing a different experiment under the same setup. We rinsed both counter and working electrodes between each measurement. The cells are pressurized with Nitrogen or Argon and a gas recirculation circuit allows to bubble the inert gas in the solutions to remove the oxygen dissolved in the solvent.

As illustrated in figure 3.21, the rotation rate dependence during neither cycling nor drying the sample is not particularly notable. There has been no change in the peak locations but slight increase in current densities on INK1CV4 (with 1600 rpm). While four reductive peaks (C0, C1, C2 and C3) are visible in Fig. 3.21, only one broad anodic is apparent (A0).

The fabrication of alpha manganese for Ink 1 was carried out by following the techniques mentioned in this thesis. As a result of this difference, Ink 1 shows slightly different electrochemical behaviour than Ink 2,3 and 5 in the cathodic reverse sweep. It also appears that Ink 2,3 and 5 that are produced with the same protocol has at least two adjacent peaks that forms a large broad peak at reduction steps (see fig. 3.22). In any case, no differences were in the CV curves acquired for Ink 2,3 and 5 (see fig. 3.22).

It is worth to notice that the current peak density of A0 (see fig. 3.21 and 3.22) gradually decreased every new cycle, while the distinct cathodic peaks disappeared after the first cycle and a new cathodic peak (C0) formed at 0.2 V vs Hg/HgO. Moreover, A0 potential shift in anodic direction over several cycles, but the peak potential of C0 remains constant.

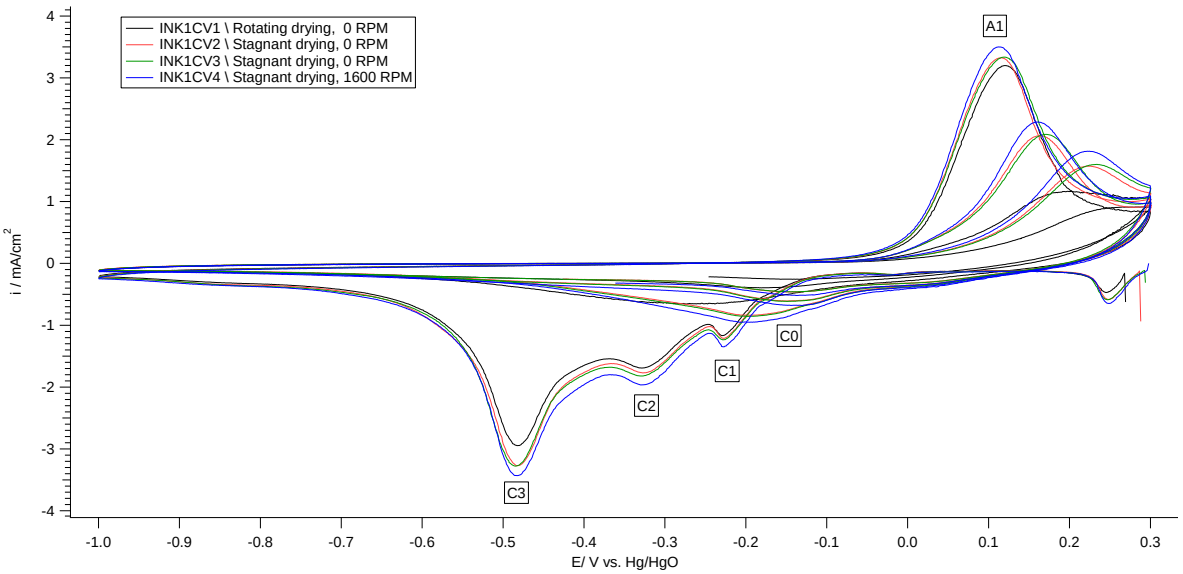

Figure 3.21 Cyclic voltammetry curve of Ink 1 drop-cast on a glassy carbon electrode at room temperature. Electrolyte solution: 0.1 M KOH. Voltage range: [OCP, -1.0 V, 0.3 V] vs Hg/HgO. Scan rate: 5 mV/s.

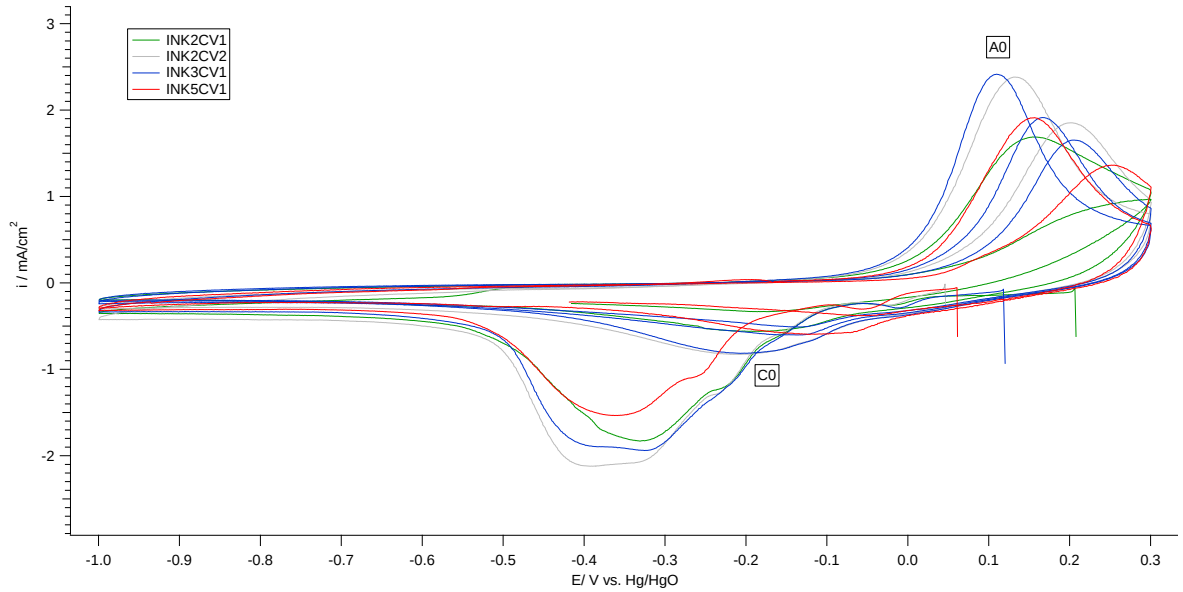

Figure 3.22 Cyclic voltammetry curve of Ink 2 and Ink 5 drop-cast on a glassy carbon electrode at room temperature. Electrolyte solution: 0.1 M KOH. Voltage range: [OCP, -1.0 V, 0.3 V] vs Hg/HgO. Scan rate: 5 mV/s.

As illustrated in Fig. 3.21 and 3.22, a pair of redox peaks developed in the CV curve after the first cycle at a scan rate of 5 mV s^{-1}. The presence of redox peaks in the CV curves between -0.2 V (C0) and 0.1 V (A0) indicates that the charge storage mechanism is primarily dependent on this redox reaction.

3.2.2 Cyclic Voltammetries in Near Neutral Solutions

In this chapter, as a calibration run, we repeated the experiments, that were applied on Ink 1, for Ink 5 samples in order to examine the reproducibility of the drop-cast protocol of choice. Then, CVs were performed in different solutions containing Na2SO4, MnSO4, and ZnSO4 salts.

First, we observe trends on the CV results (Figure 3.23) were run in the range of -1.101 V and 1.5 V vs Ag/AgCl at 5 mV s^{-1} in 0.1 M Na_2SO_4 solution while purging under N_2. The main similarities are that:

- Merged anodic peaks A1 and A2 are visible on the first anodic going scan and disappear in the consecutive cycles.
- Peak A3 tend to decrease progressively while its peak voltage remains constant.
- C0 is observed only in first cathodic going scan.

From the second cycle, the cathodic peaks C1 and C2 arose exclusively on INK5CV2. Another minor differences during cathodic sweep were identified previously in the alkaline solution (see Fig. 3.21 and 3.22). These alterations could have been generated by the overaging of the α-MnO_2 powder used in the synthesis of Ink 1.

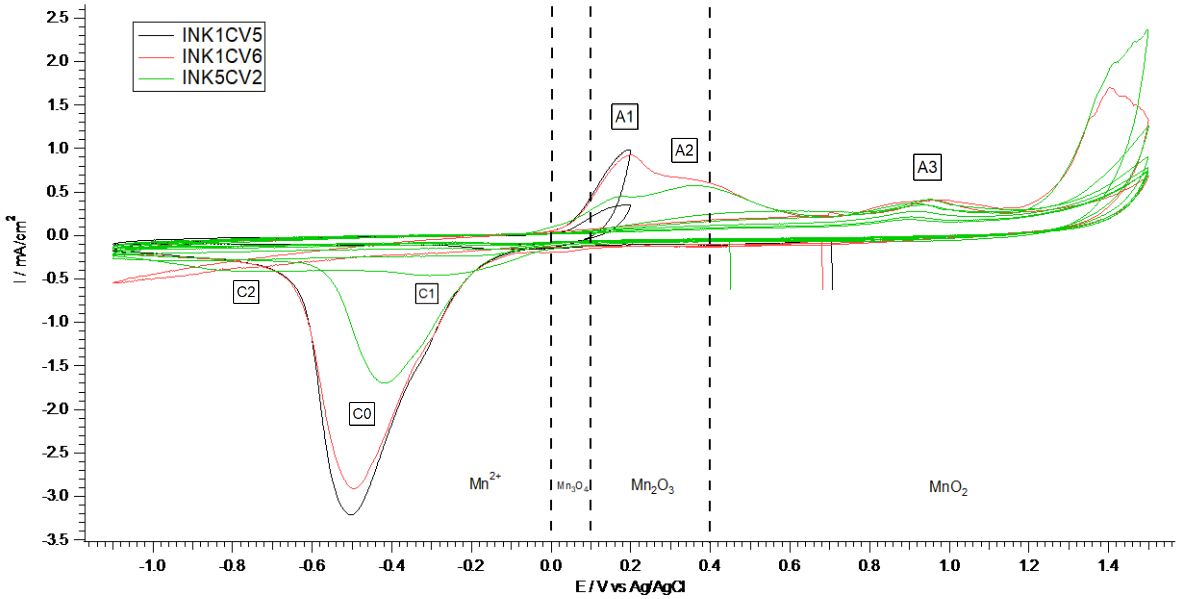

Figure 3.23 Cyclic voltammetry curve of Ink 1 and Ink 5 drop-cast on a glassy carbon electrode at room temperature. Electrolyte solution: 0.1 M Na_2SO_4. Voltage range: [OCP, -1.101 V, 1.5 V] vs Ag/AgCl. Scan rate: 5 mV/s.

When Zn^{2+} and Mn^{2+} are added to the Na^+ solution (the mixed solution), significant changes in the CVs occur (Figure 3.24). C0 is present only in the first cathodic-going scan for both the mixed and the Zn^{2+}-alone solutions (INK5CV3), and then C1 and C2 are rising after the first anodic-going scan in the mixed and the Zn^{2+}-alone solutions, respectively. A1 and A2 gradually decrease in the mixed solution, but A2 is not visible in the Zn^{2+}-alone solution.

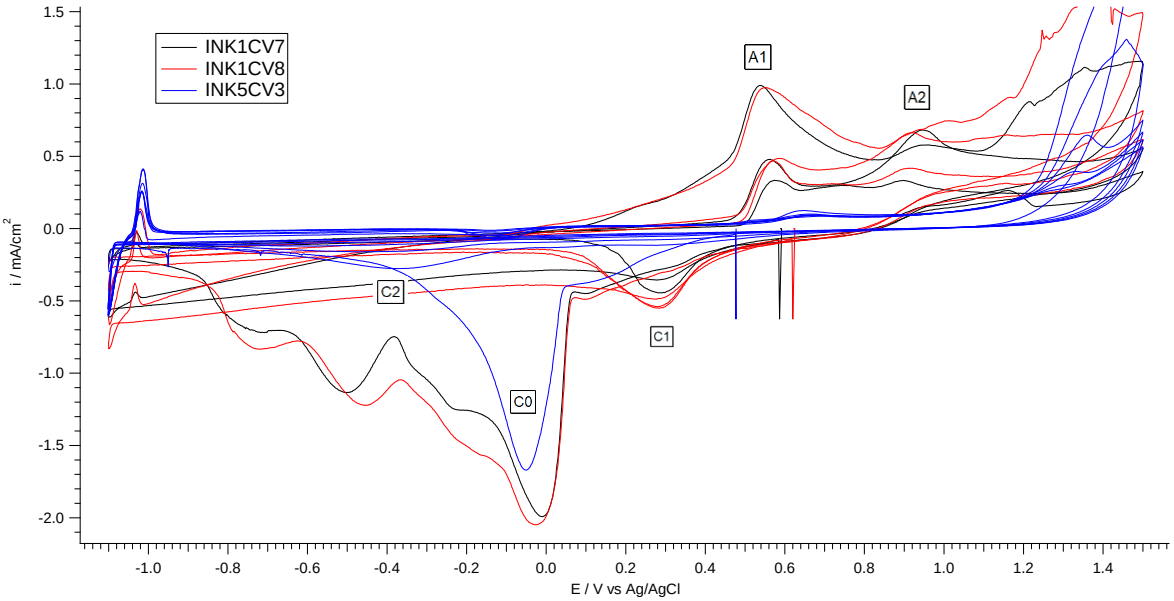

Figure 3.24 Cyclic voltammetry curve of Ink 1 and Ink 5 drop-cast on a glassy carbon electrode at room temperature. Electrolyte solutions: 0.1 M $ZnSO_4$ (INK5CV3) and 0.1 M Na_2SO_4 + 0.1 M $MnSO_4$ + 0.1 M $ZnSO_4$ (INK1CV7 and INK1CV8). Voltage range: [OCP, -1.101 V, 1.5 V] vs Ag/AgCl. Scan rate: 5 mV/s.

Now, we observe trends on the CV results were run in the range of 0 V and 0.8 V vs Ag/AgCl at 5 mV s^{-1} in Na^+-alone, and Zn^{2+}-alone solutions, respectively, while purging under N_2. We observed that the anodic and cathodic current averages are quite high in Na^+-alone solution, and the voltammogram has a more rectangular shape which is the same trend observed on the ECD1N14 measurement applied on the electrodeposited sample. (See Fig 3.18a and Fig. 3.25).

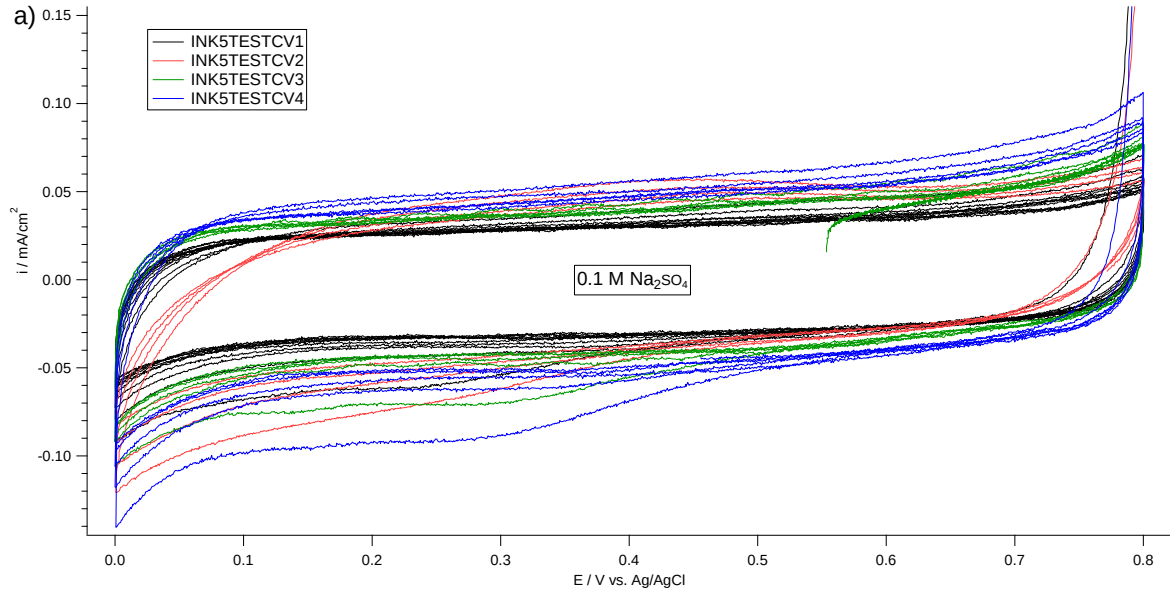

Figure 3.25 Cyclic voltammetry curves of Ink 5 drop-cast on a glassy carbon electrode at room temperature. Electrolyte: 0.1 M Na_2SO_4. Voltage range: [0 V, 0.8 V vs Ag/AgCl] and. Scan rate: 5 mV/s.

More than one cathodic peak was visible below 0 V vs. Ag/AgCl in Zn^{2+}-alone solution previously (see C0 and C2 on Fig. 3.24). Accordingly, the voltammogram resulted with the predictable appearance of a cathodic peak (C1) after extending the voltage range in cathodic direction (to -0.3 V vs. Ag/AgCl) in Zn^{2+}-alone solution (See Fig. 3.26). It is worth noting that feature A1 is shifted in anodic direction when the cathodic terminal voltage is moved to -0.3 V vs Ag/AgCl. Both anodic and cathodic charges are fading drastically after few cycles.

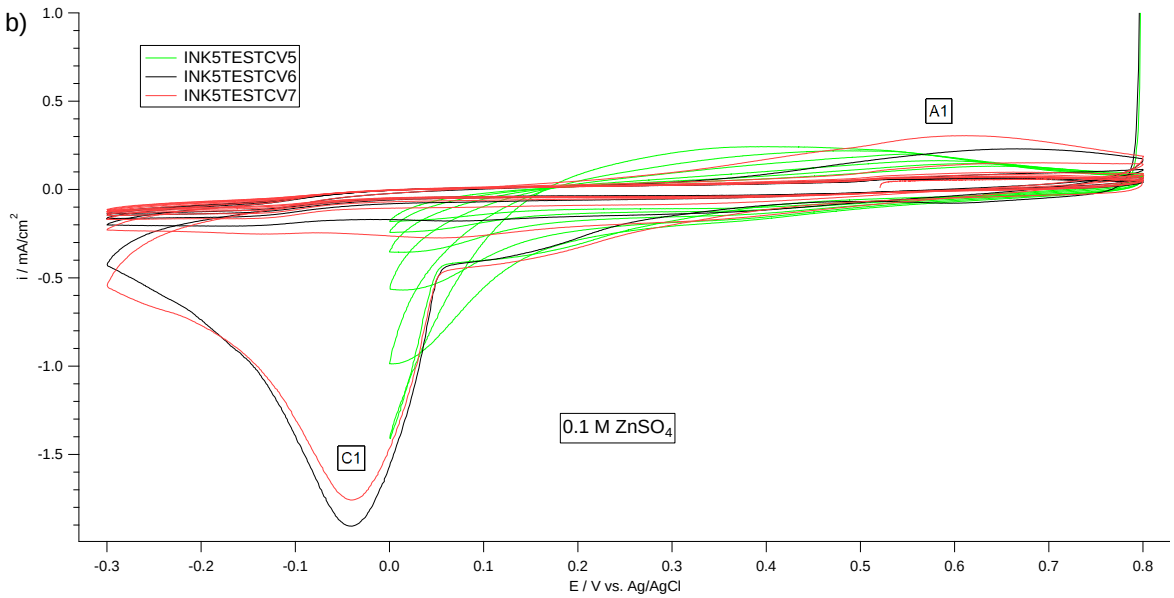

Figure 3.26 Cyclic voltammetry curves of Ink 5 drop-cast on a glassy carbon electrode at room temperature. Electrolyte: 0.1 M $ZnSO_4$. Voltage ranges: [0.8 V, 0 V] (INK5TESTCV5) and [OCP, 0.8 V, -0.3 V] vs. Ag/AgCl. Scan rate: 5 mV/s.

3.3 Physicochemical Characterization

3.3.1 X-Ray Diffraction

X-ray diffraction was employed to characterize manganese dioxide synthesized with the microwave-assisted hydrothermal method. The measurement refers to an as-synthesized pure powder sample. Fig. 3.29 shows typical cryptomelane-like pattern having tetragonal crystal structure with I4 m space group. The diffraction peaks which appeared at 2θ = 28.7°, 37.56°, 41.98°, 49.74°, 56.34°, and 60.12° can be perfectly indexed with the diffraction peaks of (310), (211), (301), (411), (600), and (521) crystal planes of cryptomelane-type α-MnO_2 standard data (JCPDS card PDF file no. 44-0141) and lattice parameters of a = b = 9.78 Å, c = 2.86 Å.

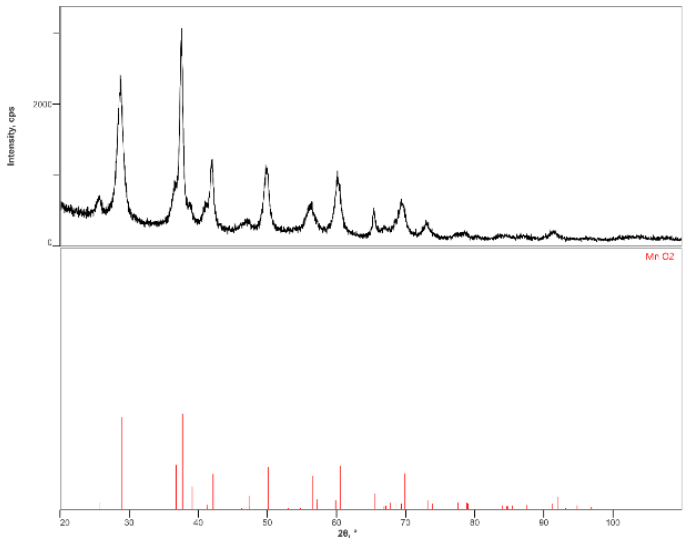

Figure 3.27 XRD pattern of spray-coated MnO2 material.

3.3.2 Scanning Electron Microscopy

The surface of the α-MnO_2 film, spray-coated onto carbon paper, was imaged by FESEM in the pristine state and after electrochemical treatments (see Section 2.3.2) in Na_2SO_4 and $ZnSO_4/Na_2SO_4$ solutions.

Table 3.2 The list of the batch of spray-coated samples sent for SEM.

Sample code	**Potentials Applied [V] vs. Ag/AgCl**	**Solution**	**Preparation method**	**Number of PS Applied**
Pristine sample (CP0)	n/a	n/a	Spray coating on CP	n/a
CP7	0.1	0.1 M Na2SO4	Spray coating on CP	1
CP8	0.1, 0.9	0.1 M Na2SO4	Spray coating on CP	2
CP9	0.1	0.1 M Na2SO4 +0.1 M ZnSO4	Spray coating on CP	1
CP10	0.1, 0.9	0.1 M Na2SO4 +0.1 M ZnSO4	Spray coating on CP	2

First, several images for the pristine sample were taken with SEM (Fig. 1.1), to verify the homogeneity of the sample.

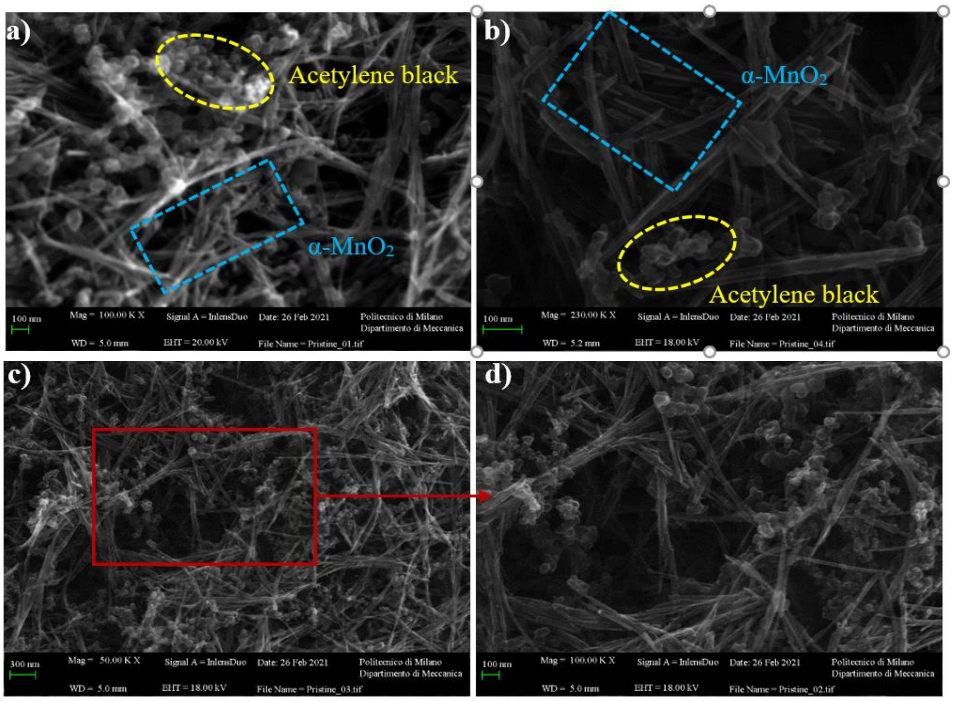

Figure 3.28 The SEM images of different points (a),(b), and (c) on the pristine α-MnO_2 spray coated electrode (CP0) and (d) the corresponding high-resolution SEM image of (c).

The morphology of α-MnO_2 film is nanorod (indicated with the blue areas on Fig. 1.1): EDS point spectra (inset of Fig 1.2a) confirmed the presence of: (i) Mn, O and K from cryptomelane; (ii) C from the C-black and from the carbon paper support and (iii) F and S (in addition to C and O) from the binder. After polarization at 0.1 V in Na_2SO_4 solution, the weight percent of Mn has been reduced from 32.2% to 14.6% (the usual caveats regarding quantitative EDS analyses, of course, apply here), which can be attributed loss of Mn by dissolution under the form of $Mn(II)_{aq}$ (see RRDE data in Section 3.2.2) (inset of Fig. 1.2b). When the electrode is

first polarized at 0.1 V and then at 0.9 V, some Mn is regained, but oxidation of $Mn(II)_{aq}$ back to solid MnO_x (inset of Fig 1.2c). Moreover, the fact that no Na is found in the pristine sample, but it is instead present in the samples treated electrochemically in the Na_2SO_4 solution, with higher relative amounts of Na found in the samples polarized at 0.1 V than in those polarized subsequently at 0.1 and 0.9 V, are compatible with Na intercalation/deintercalation processes. It is worth noting that there is no appreciable modification in the surface morphology among the three conditions investigated.

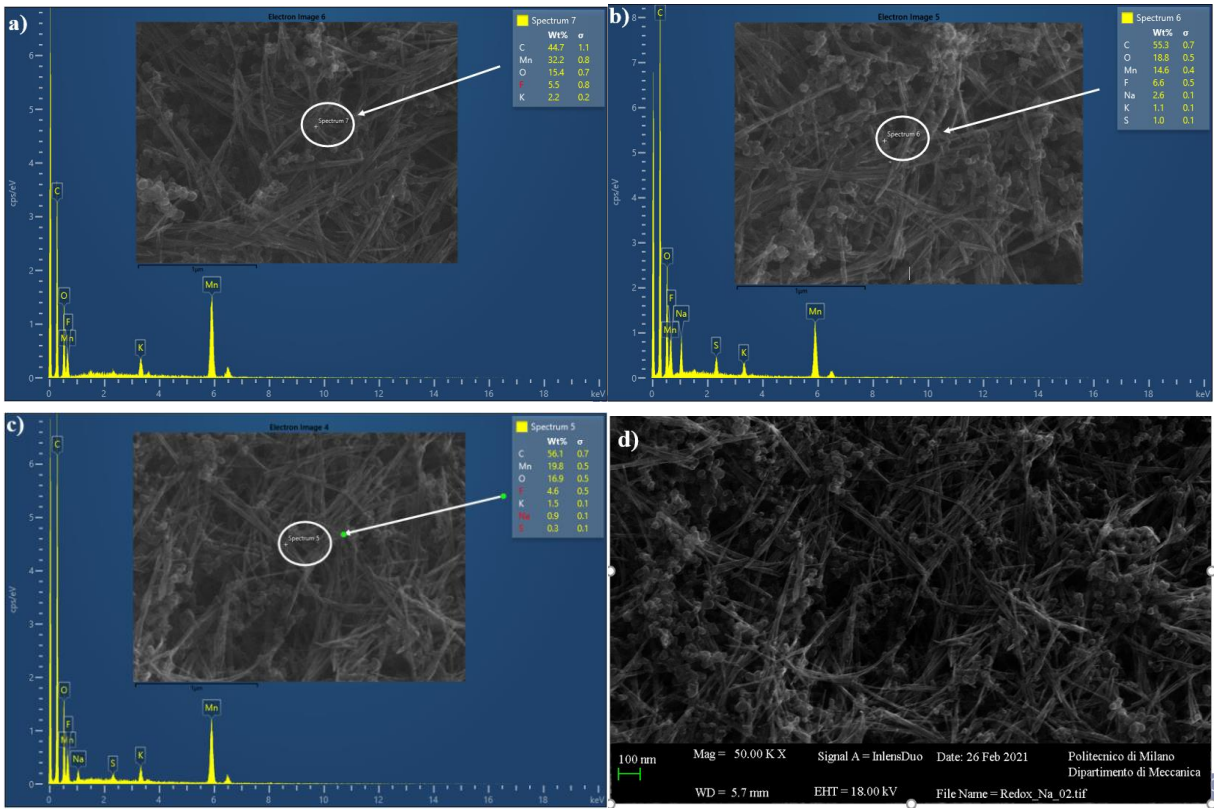

Figure 3.29 The SEM images of sample CP0 (a), sample CP7 discharged to 0.1 V (b), and sample CP8 discharged to 0.1 V and charged to 0.9 V consecutively (c),(d) in Na+-alone solution and the insets are the corresponding EDS for point scan analysis.

After electrochemical treatment in the Zn(II)-containing solution, flaky/platelet structures form (Fig. 1.3a), the EDS composition of which contains Zn as well as a high proportion of S (Fig. 1.3b): this finding is compatible with the formation of $Zn_4SO_4(OH)_6\ 4H_2O$ (ZHS), coherently with our CV (Chapter 4 - Section 4.3) and Raman (Chapter 3 - Section 3.3.3) results. When the reduction potential alone is applied, as well as when the reduction and oxidation potentials are applied consecutively, a continuous increase in the amount of Zn and S is detected (Fig. 1.3b and 1.4b,c), showing that ZHS tends to form in a wide range of electrochemical conditions, possibly independently from the accompanying Mn redox. After polarization at 0.1 V in Zn^{2+}/Na^+ solution, the weight percent of Mn is reduced, coherently with our findings with Na_2SO_4 solutions, indicating that the presence of Zn(II) does not alter appreciably Mn-dissolution. Unlike in Na^+-alone solutions, lower amounts of Mn are instead found after polarizing first at 0.1 V then at 0.9V in the Na^+/Zn^{2+} solution (Figure 1.4b,c), showing that Mn oxidation can be instead influenced by the presence of Zn(II): this finding correlates with the rapid capacity decay found in Zn^{2+}-containing solutions (see Chapter 4 - Section 4.2.3.1).

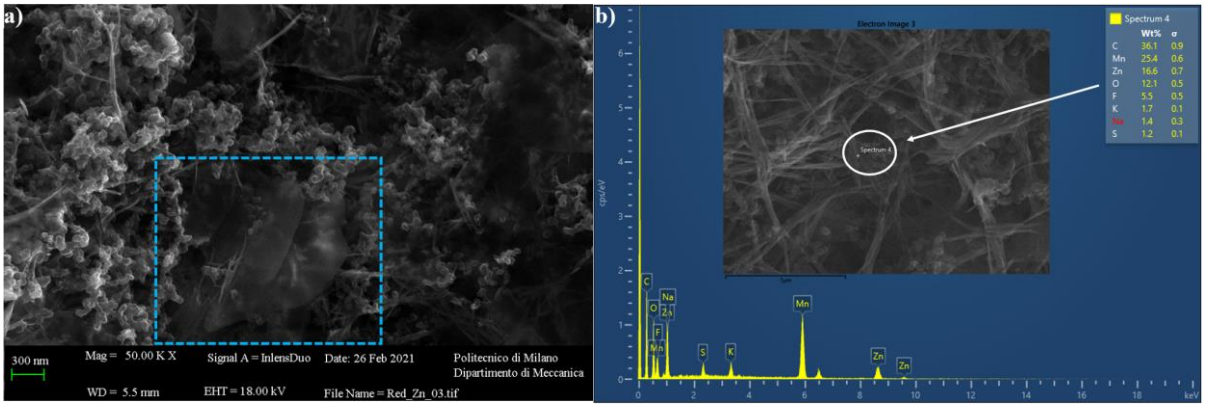

Figure 3.30 The SEM images of different points (a), (b) on sample CP9 discharged to 0.1 V in Zn^{2+}/Na^{+} solution and the inset is the corresponding EDS for point scan analysis.

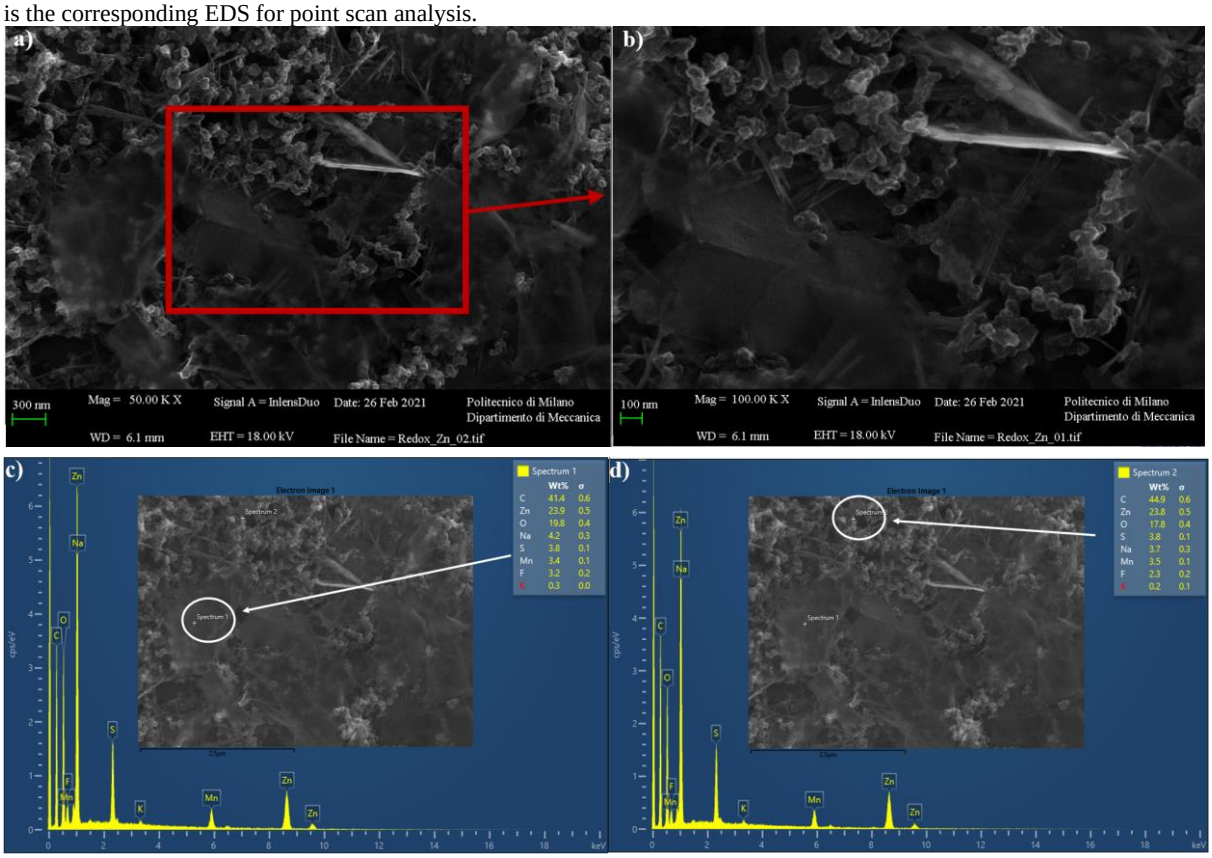

Figure 3.31 The SEM images of sample CP10 (a) discharged to 0.1 V and charged to 0.9 V consecutively in Zn^{2+}/Na^{+} solution, (b) the corresponding high-resolution SEM image of (a). and the insets (c) and (d) are the corresponding EDS for point scan analysis for spectrum 1 and 2, respectively.

3.3.3 Raman Spectroscopy

We are specifically interested in the vibrational spectroscopic properties of the α-MnO_2-type materials since Raman scattering spectroscopy at low wavenumbers provide useful alternatives and/or supplements to X-ray diffraction for structural characterization of materials. It is sensitive to local structural properties of materials, can provide a more complete and reliable description of materials such as MnO_2-related compounds, where crystalline disorders as well as different local structural properties can be expected. Since the vibrational features of MnO_2 exhibit lower Raman activity, only the stretching vibrations of [MnO_6] octahedra are proven to lie between 500 and 700 cm^{-1} [49]. The peaks at the lower wavenumber of ~580 cm^{-1} are

attributed to the deformation modes of the metal-oxygen chain of Mn-O-Mn in the MnO_2 octahedral lattice.

Ex-situ Raman analysis were acquired in order to better understand the nature of the cryptomelane-like manganese dioxide film, spray-coated onto carbon paper, after electrochemical and/or ion-exchange reactions. The same batch of spray coated samples prepared for SEM (see Table 1.1), were also investigated through Raman microscopy. The physical origin of cryptomelane-type manganese dioxide (α-MnO_2) has been widely investigated and theorized and is well summarized in [50]. Structurally, α-MnO_2 type materials crystallize into a body-centered tetragonal structure, space group I4/m; factor group analysis indicates that $6A_g + 6B_g + 3E_g$ spectroscopic species are Raman-active [51]. After revisiting the RS properties of α-MnO_2 and K-MnO_2 (See Fig .3.32b), we observe strong evidence that RS spectrum of the pristine sample has five contributions (Fig. 3.32a). The main characteristic RS peaks of α-MnO_2 are observed at 310, 362, and 648 cm^{-1} (indicated with blue arrows). Other features should be present, but their intensity is quite low so that they usually get covered by the baseline noise. It shall also be emphasized that two diagnostic RS bands at medium-frequency region, 386 and 574 cm^{-1} (indicated with red arrows), can attributed to the tunnel cation K^+ intercalated in α-MnO_2.

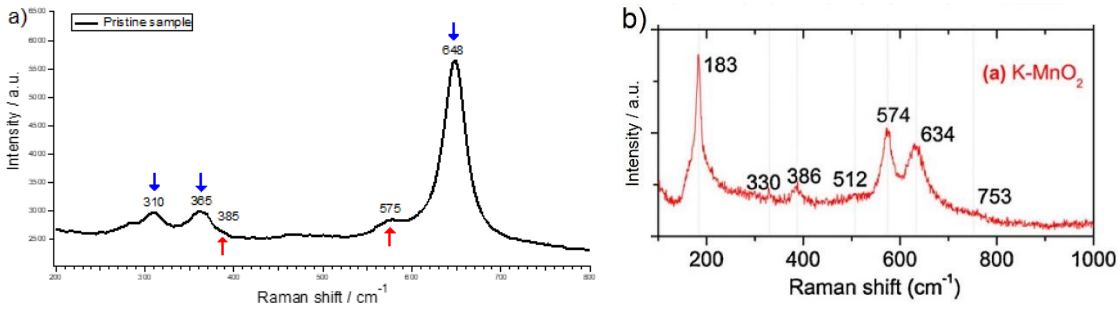

Figure 3.32 RS spectra of (a) pristine sample (spray-coated), and (b) K-MnO2 [Gao et al., 2009].

Post et al. observed a low frequency (around 620 cm^{-1}) for MnOOH, which reflects longer average Mn-O distances. Replacing Mn^{4+} with the larger Mn^{3+} shifts the corresponding peaks to lower frequencies [52]. In their next research, Chalcophanite (ZnMn3O7 • 3H 2 O; Space Group R-3, a type of layered MnO_2 with interlayered Zn ions) shows the highest frequency (at 670 cm^{-1}) compared to the other layer Mn oxides they have examined, which claims all the Mn is in 4+ valance state with the shortest possible Mn-O distance, and accordingly the highest frequency for the most diagnostic peak of MnO_x [53]. After polarization at both 0.1 V and/or 0.9 V in Na_2SO_4 solution, there is no significant band shift for internal octahedral MnO6 mode (around 650 cm^{-1}). After polarization at 0.1 V in Na^+-alone solution, there is no change in Raman spectrum (red curve) (see Fig 3.33), because the potential applied is not cathodic enough for reduction of manganese (See Chapter 3 - Section 3.2.2 – Fig. 3.23). Furthermore, after polarizing first at 0.1 V then at 0.9V in Na_2SO_4 solution, the new spectra (dark blue) is slightly shifted compared to the pristine (black), denoting that potential switch might have triggered structural change from α-Mn_2O_3 to γ-Mn_2O_3 [54].

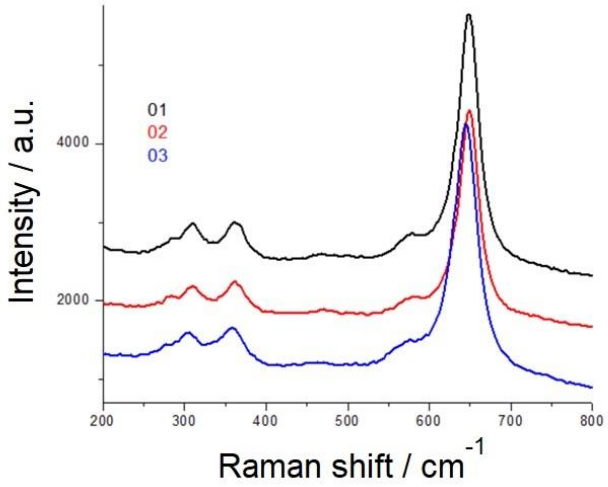

Figure 3.33 RS spectra of pristine sample CP 0 (black), sample CP7 discharged to 0.1 V (red), and sample CP8 discharged to 0.1 V and charged to 0.9 V consecutively (blue) in Na_2SO_4 solution.

After polarization at 0.1 V in the Zn(II)-containing solution, the prominent band (red curve) disappeared (See Fig 3.34). Interestingly, a new peak formed at 511 cm^{-1} on this spectrum, but it could not be assigned basis of literature. Furthermore, after polarization at both 0.1 V and 0.9 V consecutively in Zn^{2+}/Na^{+} solution, a spectra (dark blue) is congruent with the pristine (black), denoting that the reaction mechanism is reversible.

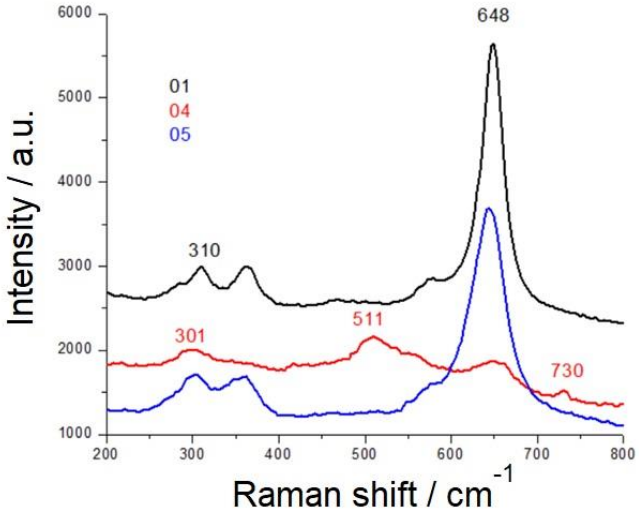

Figure 3.34 RS spectra of pristine sample CP 0 (black), sample CP9 discharged to 0.1 V (red), and sample CP10 discharged to 0.1 V and charged to 0.9 V consecutively (blue) in Na2SO4/ZnSO4 solution.

The electrodeposited carbon papers in different solutions are also investigated through Raman microscopy (see Chapter 2 - Section 2.2.1.1 – Section ECD4 for setup protocols). In both Mn^{2+}-alone and Mn^{2+}/Na^{+} solutions (Fig 3.35a), the peak positions at 350 and 639 cm^{-1} are coherent with what is found for nsutite type γ-Mn_2O_3 [54]. After introducing Zn^{2+} into Mn^{2+} solution, the spectrum shows a new pattern with 6 different peaks between 200 cm^{-1} and 800 cm^{-1} (Fig 3.35b). This pattern is most closely associated with a coexistence of $ZnMn_2O_4$ nanoparticles [55]and birnessite type δ-MnO_2 [56].

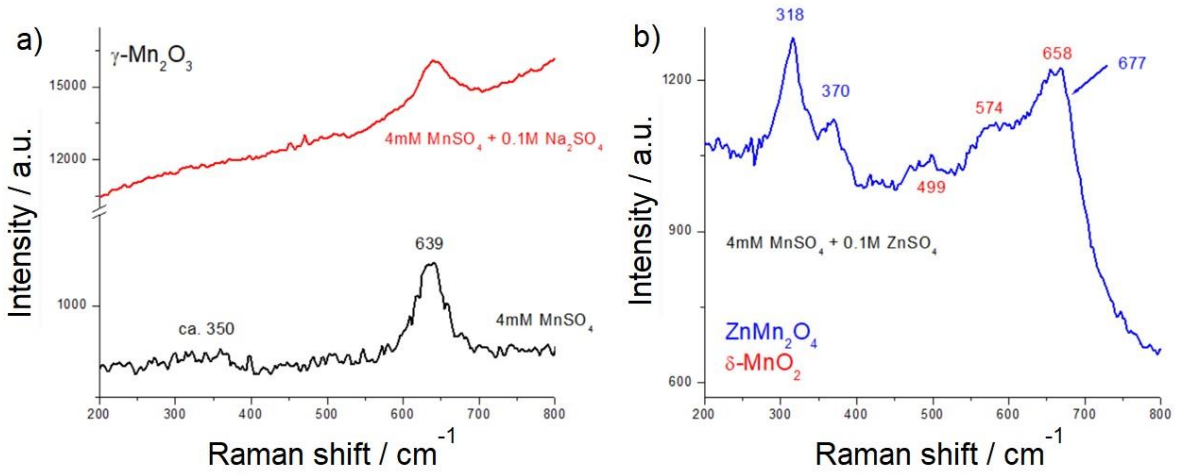

Figure 3.35 RS spectra of electrodeposited samples (a) in 4 mM $MnSO_4$ (black), in 4 mM $MnSO_4$ + 0.1 Na_2SO_4 (red), (b) 4 mM $MnSO_4$ + 0.1 $ZnSO_4$.

Chapter 4 Discussion

4.1 Overview of the Electrochemistry of Mn oxides

Mn oxides (MnO_x), owing to their low point of zero charge, large surface area, strong acid sites and easily changeable valence states, participate readily in a variety of oxidation–reduction, catalytic and cation-exchange reactions. In particular, redox process may occur at the surface of the solid, which is typically non-stoichiometric and containing several defects.

4.1.1 Electrochemistry of Mn oxides in neutral deaerated aqueous solutions

The electrochemistry of MnO_x is varied and complex, in particular in the near-neutral aqueous solutions relevant to ZIBs, strongly dependent on the crystal structure, on the details of the electrolyte composition, on the solubility of Mn species and on the surface conditions and critically and comprehensively reviewing the available literature would be a formidable task. Nevertheless, some general and ubiquitous aspects of MnO_x electrochemistry are amenable to a straightforward sequence of redox reactions, involving progressive valence changes. To address this issue concretely, we shall refer, without appreciable loss of generality, to the particular case of cyclic voltammetry during birnessite (δ-MnO_2) electrodeposition, as reported on Figure 4.1 in [29]. In the following discussion, we shall refer to this particular set of experimental data, because it represents prototypically the complexity and logic of MnO_x redox, but we shall in part modify and in many respects, generalize the interpretation put forward in this paper, in view of offering a sufficiently broad platform for the discussion of electrochemical measurements, voltammetric in particular, of this class of metarials. It is worth noting here that the redox scenario we are going to address is indeed compatible with the Pourbaix diagram of Mn in aqueous systems, but cointains more complex information, in particular regarding the redox of mixed-valent oxides.

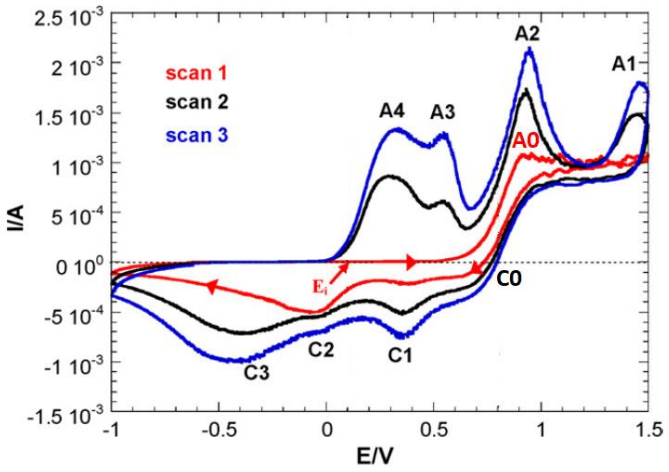

Figure 4.1 CVs for birnessite electrodeposition onto SnO_2 from a neutral, deaerated Na_2SO_4 0.4 M, $MnSO_4$ 4 mM solution, with a scan rate of 10 mV/s, potentials are reported in the Ag/AgCl scale. Subsequent scans are color-coded as indicated in the image. Elaborated from [29], with permission. We refer to the original publication, for details.

Figure 4.1 shows the CVs originally published by Larabi-Gruet et al. [29], graphically re-elaborated in view of the discussion relevant to this work. Very similar data have also been published by Ndjeri et al. [57]. Experimental details are contained in the source paper, aspects relevant to the present discussion are that the measurements have been carried out in neutral, deaerated Na_2SO_4 0.4 M, $MnSO_4$ 4 mM solution, with a scan rate of 10 mV/s. Ndjeri et al. proposed a very similar study in which the concentration of $Mn(II)_{aq}$ was varied, without modifying qualitatively the voltammetric features: only quantitative changes were observed, that can be explained with limiting c.d. effects. Coherent results were also reported in the same work, as a result of changing the scan rate. The potential scans were initiated with an anodic-going scan, starting from the OCP of 0.12 V (potentials refer to the Ag/AgCl scale, unless otherwise stated). In the following, we propose a discussion of the voltammetric features found in Figure 4.1 – referring to each feature with the code reported in the image and – in Table 4.1 we summarize it. It is worth noting that we are modifying some of the interpretations of [29] and ref.s therein, to make them more adherent to the sequence of oxidation processes as well as allowing for intercalation processes [58], [59]. Finally, it is important to note that, since most of the electrochemical reactions involving Mn-species include exchanges of protons, in the absence of buffering agents, potential-dependent changes in pH is an important point that ought to be address explicitly in future work on neutral electrolytes.

Table 4.1 List of voltammetric features of Figure 1, referring to the electrochemical behaviour of Mn in deaerated neutral aqueous solution, and their interpretation.

Feature code	Redox process	Net valence changes of Mn species
A0	$Mn(II)_{aq} \rightarrow M(IV)_{solid} + 2e^-$ $(Mn(II)_{aq} \rightarrow M(III)_{solid} + e^-$ $M(III)_{solid} \rightarrow Mn(IV)_{solid} + e^-)$	$Mn(II)_{aq} \rightarrow M(IV)_{solid} + 2e^-$
C0	$2Mn(IV)O_2 + Na^+/H^+ + e^-$ $\rightarrow Na/HMn(III)Mn(IV)O_4$	$2Mn(IV)_{solid} + e^-$ $\rightarrow M(III)_{solid}M(IV)_{solid}$
C1	$Na/HMn(III)Mn(IV)O_4 + Na^+/H^+ + e^- \rightarrow 2Na/HMnO_2$ $HMn(III)Mn(IV)O_4 + H_2O + e^-$ $\rightarrow 2MnOOH + OH^-$	$M(III)M(IV)_{solid} + e^-$ $\rightarrow 2M(III)_{solid}$
C2	$3Mn(III)_2O_3 + H_2O + 2e^-$ $\rightarrow 2Mn(II)Mn(III)_2O_4 + 2OH^-$	$2M(III)_{solid} + e^-$ $\rightarrow M(II)M(III)_{solid}$
C3	$Mn(II)Mn(III)_2O_4 + 4H_2O + 2e^-$ $\rightarrow 3Mn(OH)_2 + 2OH^-$ $Mn(II)Mn(III)_2O_4 + 4H_2O + 2e^-$ $\rightarrow 3Mn^{2+} + 8OH^-$	$M(II)M(III)_{solid} + e^- \rightarrow$ $2M(II)_{solid/aq}$
A4	Reverse of C3, referring to solids	$2M(II)_{solid} \rightarrow$ $M(II)M(III)_{solid} + e^-$
A3	Reverse of C2	$M(II)M(III)_{solid}$ $\rightarrow 2M(III)_{solid} + e^-$
A2	Reverse of C1	$2M(III)_{solid} \rightarrow$ $M(III)M(IV)_{solid} + e^-$

Feature A0 – According to [29], scanning the potential anodically, starting from OCP with a clean electrodic substrate (SnO_2, in this case), anodic current starts flowing at ca. 0.6 V and an anodic plateau is found from +0.9V (feature A0), which corresponds to the oxidation of $Mn(II)_{aq}$, forming a solid film: the potential range suggests that the oxidation product is solid Mn(IV). The global reaction can be schematized as:

$Mn(II)_{aq}+2H_2O \rightarrow MnO_2+4H^+ +2e^-$

Most probably, coherently with thermodynamic data, the formation of the Mn(IV)-containing solid goes through an intermediate Mn(III)-containing solid. The plateau c.d. is compatible with a limiting-c.d. for a process in aqueus electrolyte with the relevant bulk concentration of Mn(II). A slightly different, but compatible, picture is put forward by [42], where an ECE mechanism, with the second electrochemical step as the rate-deterining one, is proposed for weakly acidic and or neutral solutions, involving the following steps: (E1) $Mn(II)_{aq} \rightarrow Mn(III)_{aq}+e^-$; (C) $Mn(III)_{aq}+2H_2O^- \rightarrow MnOOH+3H^+$; (E2) $MnOOH \rightarrow MnO_2+H^+ +e^-$.

Feature A0 is observed only in the first anodic scan, indicating that the electrochemical response on the second anodic-going scan is solely controlled by the solid present on the electrode at the end of the previous cathodic scan. Formation of A0 on the first anodic-going scan is necessary for the development of the sequence of cathodic peaks C1-C3 described below: this issue has been explicitly addressed in [57].

Feature C0 – In the cathodic-going scan, irrespective of the scan number, the current changes sign at ca. 0.85 V and to take on an I-V behaviour, coherent with diffusion-limited reduction, that can be attributed to the formation of $Mn(III)_{solid}$ species in a $Mn(IV)_{solid}$ matrix. In the relevant ambient, this process might be due to intercalation or co-intercalation of Na^+ and/or H^+: schematically. It is worth noting that feature C0 can be observed only it the anodic terminal voltage is not moved far into the OER range (compare, e.g., Figure 1 of [29] and Figure 1 of [57]).

Feature C1 – This CV peak, that is present in all cathodic-going scans, has been attributed to the reduction of solution species of the type: $Mn(III)_{aq}+e^- \rightarrow Mn(II)_{aq}$ [60]. This explanation is probably more appropriate for more acidic systems [42], but in any case can be interpreted as full reduction of Mn(IV) to Mn(III), probably in the solid state and possibly through complete intercalation. An alternative process could be the reduction of residual Mn(IV) to Mn(III) in the form of groutite α-MnOOH [29]. A more complex explanation of C1, based on an EC mechanism, has been put forward in [57]:

[E] $Mn(IV)_{surf}+e^- \rightarrow Mn(III)_{surf}$;

[C] $xMn(III)_{surf}+ yMn(II)_{aq}+(3x+2y)H_2O \rightarrow [xMn(OH)_3 \cdot yMn(OH)_2]+ (3x+2y)H^+$.

Adoption of a two-step scheme and incorporation of $Mn(II)_{aq}$ in the reaction mechanism, does not change the overall message that this peak is related to the partial reduction of $Mn(IV)_{solid}$ to $Mn(III)_{solid}$, since Mn(II) present in the conjectured complex does not result from a reduction process, but rather from incorporation of a species present in the solution.

Feature C2 – This further voltammetric feature of the cathodic-going scan is a peak, that is found in all cathodic-going scans and has been attributed, in combination with feature C3 discussed more in detail below, to the to the reduction of Mn(IV) to Mn(II) via an intermediate Mn(III) compound [60]–[62]. In particular, [33], [60] attribute feature C2 to the process: $MnO_2+H^+ +e^- \rightarrow MnOOH$. On the basis of thermodynamics, the individual peak C2 might rather correspond to the following reduction process $Mn(III)_{solid}+e^- \rightarrow Mn(II)_{solid}$, e.g. corresponding to the formation of a mixed-oxide species,

such as Mn_3O_4 or the transformation of the [$xMn(OH)_3 \cdot yMn(OH)_2$] complex form a low-y form to a high-y one [57].

Feature C3 – This last peak of the cathodic going scan (of course, in a potential range in which Mn cannot be reduced to the metallic form) might correspond to complete reduction to Mn(II), as solid $Mn(OH)_2$ or with partial dissolution to $Mn(II)_{aq}$. [29] reports that, for potentials more cathodic than C3, the working electrode becomes pale brown due to a partial dissolution of the Mn(II)-containing solid $Mn(OH)_2$ into soluble $Mn(II)_{aq}$ species. In particular, [29], [60] interpret feature C3 as corresponding to the reaction: $MnOOH+H^{+}+e^{-} \rightarrow Mn(OH)_2$. It is worth noting that feature C3 tends to grow with cycling, witnessing the buildup of a Mn(III)-containing film, liable to undergo reduction to Mn(II).

The residual solid present at the electrode at the end of the cathodic-going scan, is electro-oxidized back to Mn(IV) in four steps (denoted by labels: A4, A3, A2 and A1) during the subsequent anodic-going scan.

Feature A4 – Can be explained as the oxidation of a Mn(II) compound to a mixed Mn(II)–Mn(III) compound, in a process that would be the reverse of C3. As commented above regarding feature A0, the solid electrodeposited during the cathodic-going scan modifies the Mn(II) oxidation process: this implies that electron transfer occurs some diffusion process, as suggested in [60]. Specifically, [29] suggests the mechanism: $3Mn^{(III)}(OH)_{2,solid} \rightarrow Mn_3O_4+2H^{+}+2e^{-}$, were, of course: $Mn^{(II)}Mn^{(III)}{}_2O_4$.

Feature A3 – Might correspond to the oxidation of the mixed Mn(II)–Mn(III) compound to a Mn(III) compound, i.e. the reverse of C2. Specifically, [29] proposes: $Mn_3O_4+2H_2O \rightarrow 3MnOOH+H^{+}+e^{-}$.

Feature A2 – Can be assigned to the oxidation of a Mn(III) compound to a mixed-valent Mn(III)–Mn(IV) one: the reverse process with respect to C1. The conjectural schematic of [29], a work that is focused on the growth of birnessite Mn_7O_{13}, for this case, can be restated as: $7Mn^{(III)}OOH \rightarrow Mn^{(IV)}{}_5Mn^{(III)}{}_2O_{13}+H_2O+5H^{+}+5e^{-}$.

Feature A1 – Can be interpreted in terms of the oxidation of a Mn(III)-Mn(IV) compound to a Mn(IV)-containing species. Again, this can be expressed according to the stoichiometric scheme of [29] as: $Mn^{(IV)}{}_5Mn^{(III)}{}_2O_{13}+H_2O \rightarrow 7Mn^{(IV)}O_2+2H^{+}+2e^{-}$.

Finally, it should be noticed that after a few cycles a steady-state voltammetric pattern is attained, with c.d.s that tend to increase, reaching an asymptotic level, showing that a solid film forms, exhibiting low solubility and good electronic conductivity, allowing electron transfer, that undergoes a sequence or redox processes upon cycling. Moreover, as emphasized in [29], the presence of untransformed birnessite Mn_7O_{13} and groutite α-MnOOH in films exposed to anodic polarizations at which MnO_2 is the stable form, testifies that sluggish kinetics might result in retention of out-of-equilibrium phases in MnO_x films subjected to electrochemical polarization.

4.1.2 Electrochemistry of Mn oxides in neutral aerated aqueous solutions

O_2 saturation of $Mn(II)_{aq}$ solutions does not modify the voltammetric pattern, but has been reported to lead to complete oxidation of MnOOH formed at C1 back to Mn(IV) [29].

4.1.3 Electrochemistry of Mn oxides in acidic aqueous solutions

A large number of studies have been published regarding the electrodeposition of MnO_2 in strong acidic sulphate media, owing to the interest of the preparation of electrochemical manganese dioxide (EMD) for alkaline battery cathodes and supercapacitors (e.g. [42] and references therein). This topic will be treated only cursorily here, because of limited interest for ZIBs. Also in this case, the global oxidation reaction leading from $Mn(II)_{aq}$ to $Mn(IV)O_2$ goes through Mn(III) intermediates.

Apart from details, that can be retrieved e.g. in [42], the key point with strongly acidic solutions is that Mn(III) is soluble and readily disproportionates according to the scheme: $2Mn(III)_{aq} \rightarrow Mn(II)_{aq} + Mn(IV)_{solid}$. The solubility of Mn(III) leads to the possibility of growing pure Mn(IV) compounds. These are appropriate for alkaline battery cathodes and supercapacitors, but more complex structures, possibly containing a fraction of Mn(III) in the crystal structure, enabled by neutral solutions [32], [33], [60], can be better suited for intercalating or electrocatalytic Mn compound, of interest for ZIB and ZAB applications, respectively.

4.1.4 Electrochemistry of Mn oxides in alkaline aqueous solutions

Work on the electrochemistry of MnO_x in alkaline aqueous ambient has main focussed on γ-MnO_2, owing to its interest for commercial alkaline batteries. Several classical papers have addressed the reduction reaction mechanisms, highlighting strong dependence on operating conditions, such as: c.d., additives and oxide dopants [63]–[67]. More recently, renewed interest in secondary alkaline batteries has also brought back into the spotlight mechanistic issues regarding the reoxidation of MnO_2 reduction products in alkaline electolytes [68].

Notwithstanding the complexity of the scenario if details are taken into full account, along the line of reasoning of Section 4.1.1 above, it is still possible to rationalize the redox of MnO_x also in alkaline ambient with a reasonably general class of simple processes. Basically, in the reduction of γ-MnO_2, two types of reactions are found: (i) a homogeneous solid-solution one, leading to the continuous voltage variation that is typical of intercalation processes without phase changes and (ii) and a heterogeneous, multi-phase reaction, giving rise to a characteristic voltage plateau. The homogeneous reduction process can be described as:

$\gamma\text{-}MnO_2 + xH^+ + xe^- \rightarrow H_xMnO_2$

while the heterogeneous one can be schematized as:

$(x+y)\gamma\text{-}MnO_2 + (x+2y)H^+ + (x+2y)e^- \rightarrow xMnOOH + yMn(OH)_2$

It is worth noting that MnOOH can undergo dispoportionation, yielding Mn(IV) and Mn(II) species: the latter tend to dissolve in strongly alkaline ambient [69].

The homogeneous reaction is typical of low DODs, while, higher DODs activate also the hererogeneous mechanism. The former is reversible, and allows recharge, while the latter is irreversible, owing to the accompanying phase changes, in particular yielding Mn_3O_4 [68], [70].

4.1.5 Interaction of Zn with redox processes of MnO_x

4.1.5.1 Alkaline solutions

Hetaerolite $ZnMn_2O_4$ has been reported to form as an irreversible phase at the cathode of alkaline batteries [67], [68], [71], [72]. This side product is the result of the chemical reaction between $Zn(OH)_4^{2-}$ and MnOOH: the anodic and cathodic reactions products, respectively. $ZnMn_2O_4$ is highly resistive and notably electrochemically inert, thus impairing the recharge process.

4.1.5.2 Near neutral solutions

The most commonly reported mechanism is reversible Zn ion intercalation/deintercalation, which involves a reversible phase transition from tunnel-structured -MnO_2 to layer-structured Zn-birnessite, spinel $ZnMn_2O_4$, or layered Zn-buserite [19]. A layer-type MnO_2(δ-MnO_2), where Zn^{2+} can intercalate into the structure, showing different structural evolution patterns because of the diversity of δ-MnO_2 phases (e.g chalcophanite, birnessite, buserite, and vernadite), which results in joint incorporation of cations and water molecules within the interlayer. For example, spinel-type $ZnMn_2^{3+}O_4$ was observed when nano-flake δ-MnO_2 was used in an aqueous electrolyte [18], while a reversible variation of MnO_2/$ZnMnO_2$ was observed for hydrated δ-MnO_2 in a non-aqueous solution [73].

At variance with this approach, as mentioned in Chapter 1, Sun et al. [20] proposed H^+ and Zn^{2+} cointercalation in akhtenskite-structure MnO_2 (ε -MnO_2). The consecutive formation of the MnOOH and $ZnMn_2O_4$ strongly promotes this mechanism of insertion of H^+ followed by Zn^{2+}.

In addition to redox-related intercalation and phase transition, an accompanying precipitation process was recognized, which leads to the formation of inactive $Zn_4(OH)_6(SO_4)\cdot 5H_2O$ (ZHS) on the surface of α-MnO_2, that could be removed by rinsing [19], [21]. On the contrary, a new study [22] revisited the effect of ZHS formation, proposing a complex reversible dissolution-deposition mechanism that contributes to capacity.

At the end of this section, we wish to emphasize that the above-reported mechanistic considerations are mainly based on integral electrochemical measurements and thermodynamic calculations, complemented by a limited number of *ex situ* structural studies. Needless to say that notably more insight could be achieve by *in situ* measurements, sensitive to chemical state and structure.

4.2 Impact of Zn^{2+} on the electrochemical behaviour of electrodeposited MnO_x in near-neutral aqueous solution

In ZIBs, as well as, to some extent in ZABs, the redox of MnO_x occurs in the presence of Zn^{2+} solution species. In view of gaining fundamental understanding of this process, this section addresses the role of the interaction of Zn^{2+} with birnessite, δ-MnO_2 films, electrochemically grown onto glassy carbon by voltammetric cycling in a potential range encompassing the Mn(II)-Mn(IV) redox.

4.2.1 Electrodeposition of MnO_x in near-neutral aqueous solution

Electrodeposition of birnessite onto extraneous electrodes is reasonably well documented in the literature (e.g. [29], [57]). We selected glassy carbon as a substrate because it is more stable than SnO_2 and can be pretreated in a way that ensured high reproducibility standards.

Our interpretation of voltammetric features is based on the overview of Section 4.1, the key results of which are summarized, for ease of reference, in Figure 4.2, below. Again, for ease of reference, as well as to enable easy appreciation of the pH effects that we shall consider later in this Section, we are reporting the positions on the voltage scale of the voltammetric features on the Pourbaix diagram, in Figure 4.3.

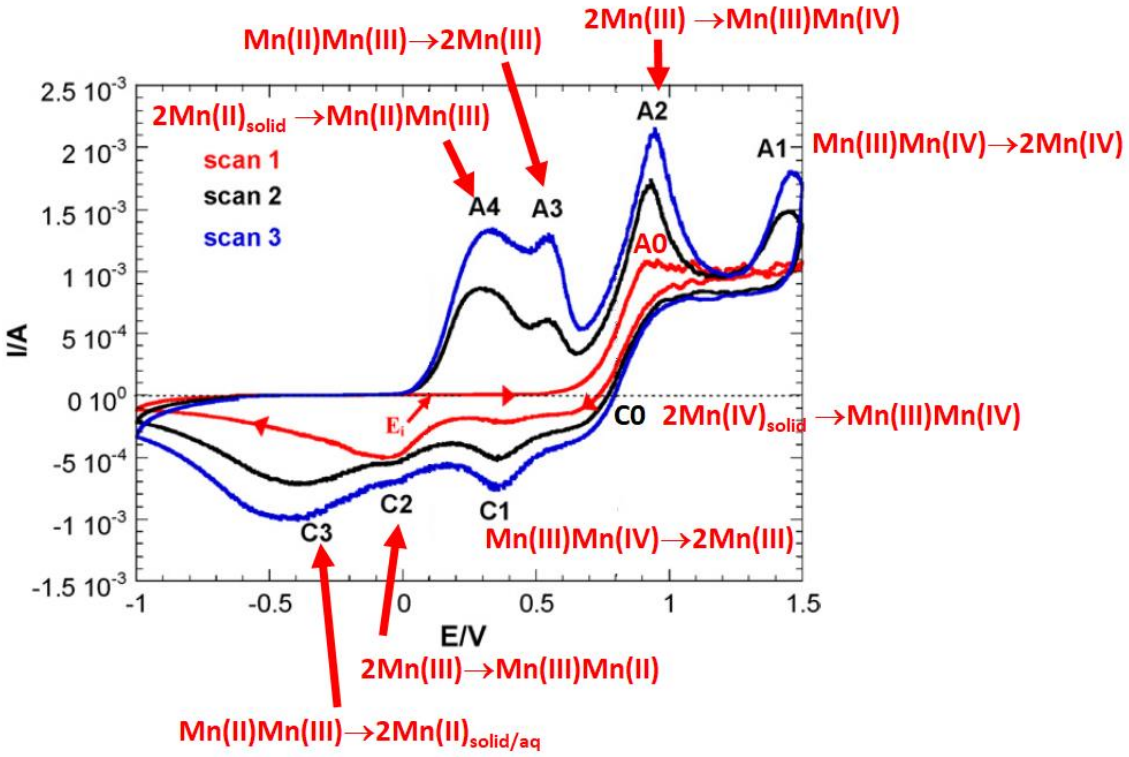

Figure 4.2 Schematic adopted for the assignment of CV features for MnO_x films in neutral electrolyte. See also Figure 4.1 and refer to Section 4.1 for details.

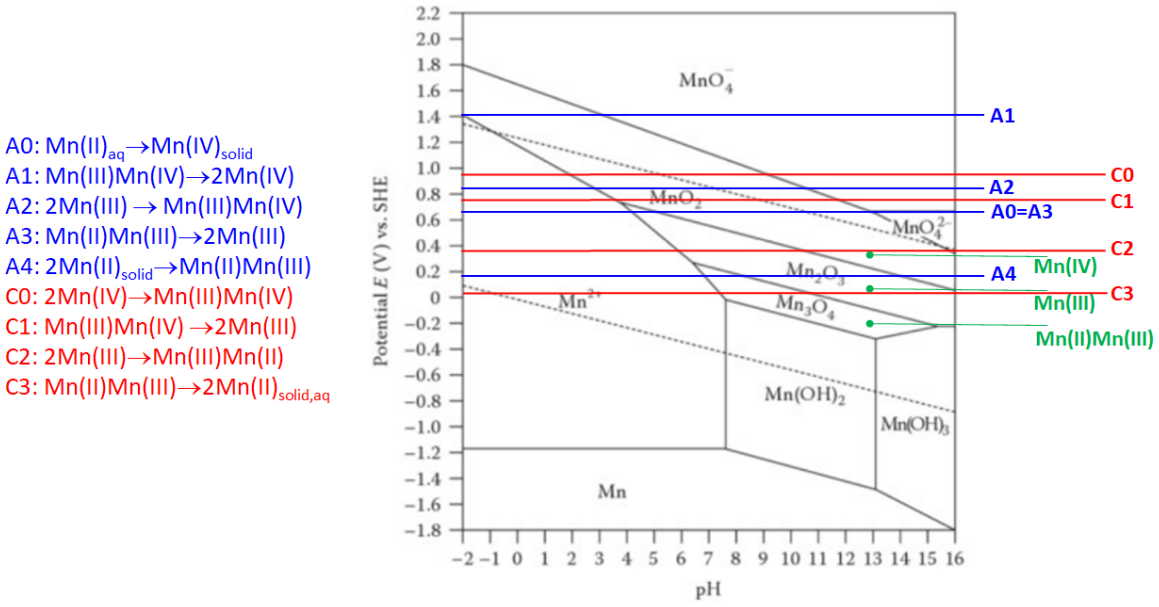

Figure 4.3 Positions, on the voltage scale, of the voltammetric features of Figure 2, reported on the Pourbaix diagram for the Mn/H2O system at room T.

As a calibration run, and in order to address the potential role of Na^+ intercalation, we repeated the experiments of [29] under nominally identical conditions, but increasing the number of voltammetric cycles, in order to attain a proved steady-state condition. Our results are shown in Figure 4.4. Apart from negligible differences in peak positions, that might be due to details of the electrochemical configuration, the voltammetric pattern is essentially the same as that of Figure 4.3. The main differences are that: in keeping with [57], peaks C0 and C1 tend to merge; (ii) the cathodic peaks of our CV are sharper and better defined that those of [29]. Moreover, prolonged cycling disclosed an evolution of the MnO_x film that escaped the analyses of [29], [57], disclosing that the asymptotic CV pattern is one in which peaks C3 and A4 tend to vanish progressively, while peak A3 increases and shifts to higher anodic potentials. In correspondence, the c.d. in the high cathodic range, more negative than C3, is vanishing. The long-term evolution of the CVs seems to point towards a stabilization of the mixed Mn(II)Mn(III) species, that loses its propensity to fully reduce to Mn(II) in the investigated potential range. The merging of peaks C0 and C1 is compatible with a homogenous Na^+-intercalation reaction, possibly favoured by structural differences in the film triggered by the differences in nucleation between GC and SnO_2. Moreover, the decreasing intensity of peak C0-C1 with cycling seems to correlate with the progressive change in the A3+A4 pattern, that might correspond to structural changes that discourage intercalation, possibly owing to the buildup of inactive Mn_3O_4, that might be identified with the Mn(II)Mn(III) species that seems to be stabilized in this system. In fact, oxide buildup is witnessed by the fact that the anodic consumed charge after prolonged cycling is notably larger than the cathodic one (See Fig. 4-B).

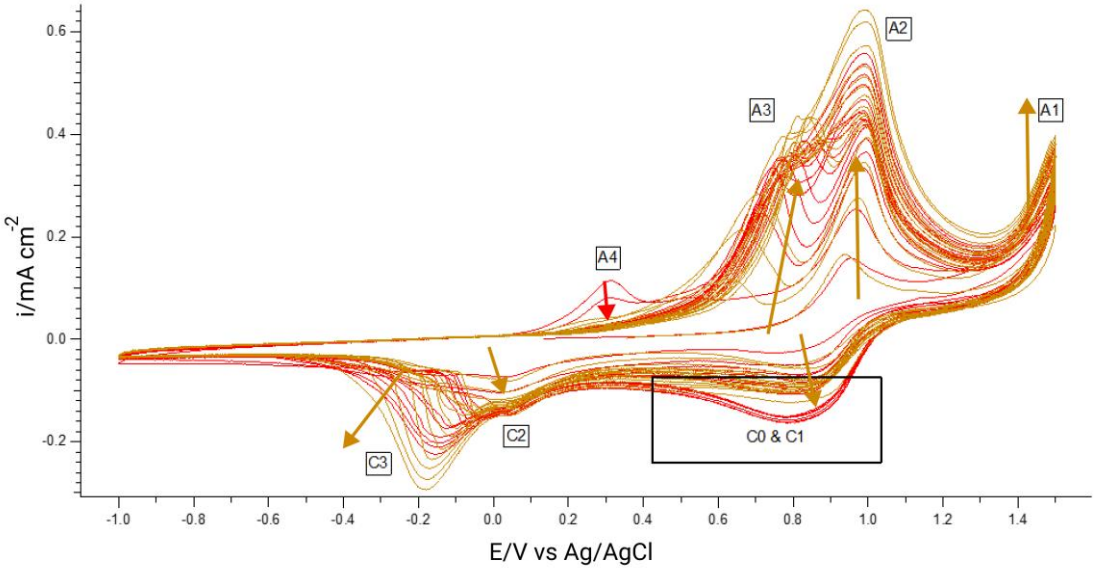

Figure 4.4 CVs measured in 4 mM $MnSO_4$ + 0.1 M Na_2SO_4 neutral solution. CV corresponds to the light brown curve is a replica of the red one. WE: glassy carbon, Scan rate. 10 mV/s. RE, Ag/AgCl 3.5 M.

Repeating the same experiment in a Na^+-free electrolyte (Figure 4.5) results in interesting quantitative changes in an essentially similar qualitative voltammetric pattern. (i) Merged features C0-C1 are shifted cathodically, as well as peaks C2 and C3; (ii) the c.d. at high cathodic potentials is appreciably larged in the absence of Na+, and, in correspondence feature A4 exhibits some residual current even after prolonged cycling; (iii) peak A4 is found at higher anodic potentials, moreover, it shifts anodically, at variance with what we found in the Na+-containing solution. These changes witness the formation of different structures, a full characterization of which cannot be based solely on electrochemical measurements. Nevertheless, some clear-cut conclusion can be drawn: the H+-intercalation process of features C0-C1 is less energetically favoured and more extensive reduction

of the electrodeposit to Mn(II) takes place. In addition, full oxidation of the film requires higher potentials, possibly owing to the progressive growth of poorly conducting material.

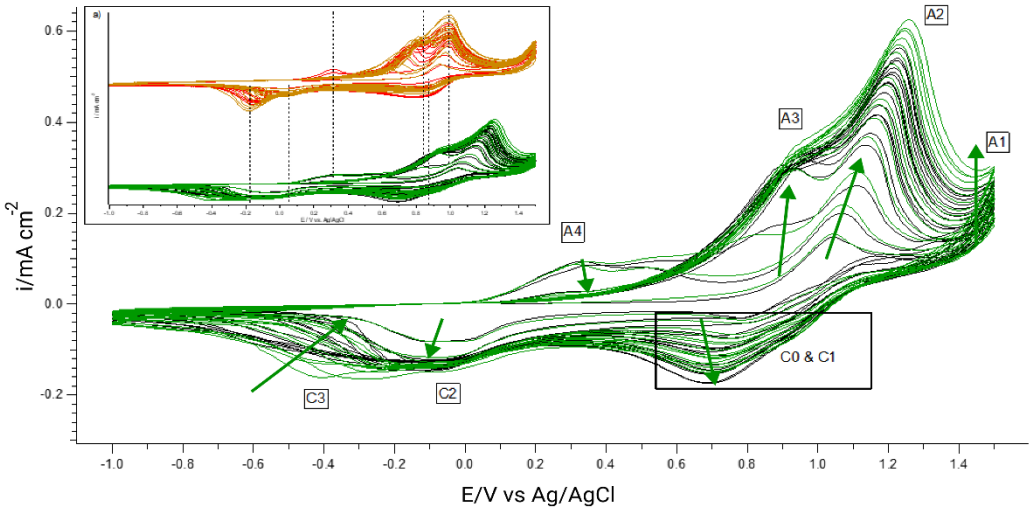

Figure 4.5 CVs measured in 4 mM $MnSO_4$ neutral solution. CV corresponds to the green curve is a replica of the black one. WE: glassy carbon, Scan rate. 10 mV/s. RE, Ag/AgCl 3.5 M. Inset (a): comparison with CVs in Na_2SO_4-containing solution (Figure 4.4).

Adding Zn^{2+} to the Mn^{2+} solution results in deep changes in the CVs (Figure 4.6). The measurement reaches a very stable steady-state cycle, characterized by well defined type-C1 and type-A1 peaks. Anodic charges are notably lowered with the presence of Zn^{2+} ions , while cathodic charges remained unaltered (Figure 4.7c), compared with Mn^{2+}-alone (Figure 4.7b) and Na^{+}-containing solutions (Figure 4.7a). The CVs do no exhibit a tendency to decrease and the consumed anodic and cathodic charges are very similar. This scenario is compatible with intercalation/deintercalation of Zn^{2+}, without formation of phases that would tend to inhibit this process.

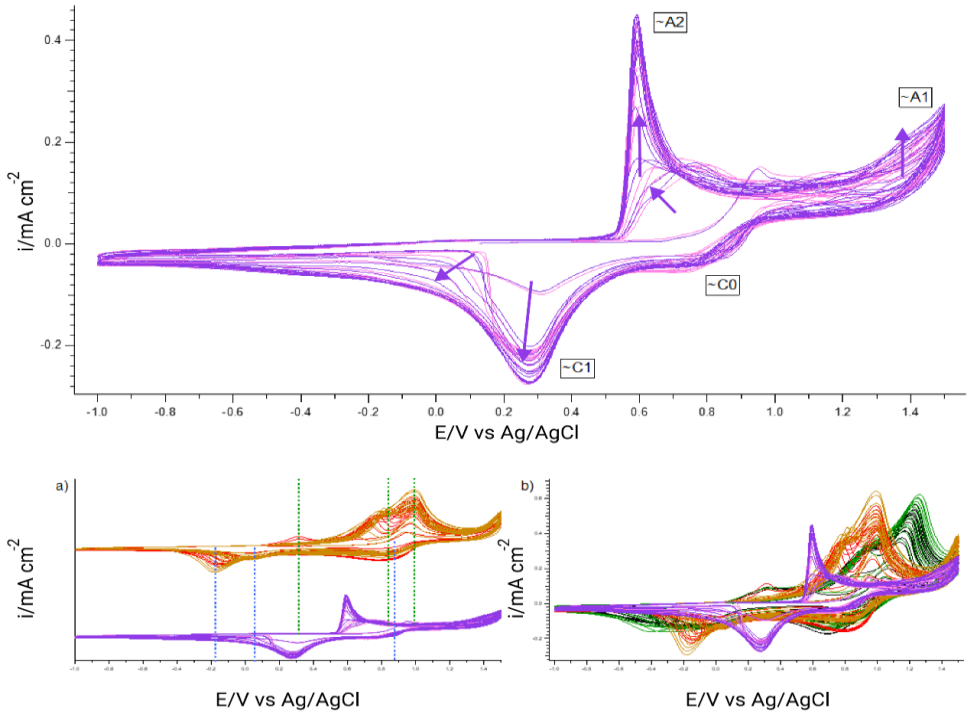

Figure 4.6 CVs measured in 4 mM $MnSO_4$ + 0.1 M $ZnSO_4$ neutral solution. WE: glassy carbon, Scan rate. 10 mV/s. RE, Ag/AgCl 3.5 M. Inset (a): comparison with CVs in solution containing only $MnSO_4$. CV corresponds to the purple curve is a replica of the pink one. Inset (b): comparison with CV in solution containing only $MnSO_4$ (green/black, see Figure 4.5) and Na_2SO_4+$MnSO_4$ (red, see Figure 4.4)

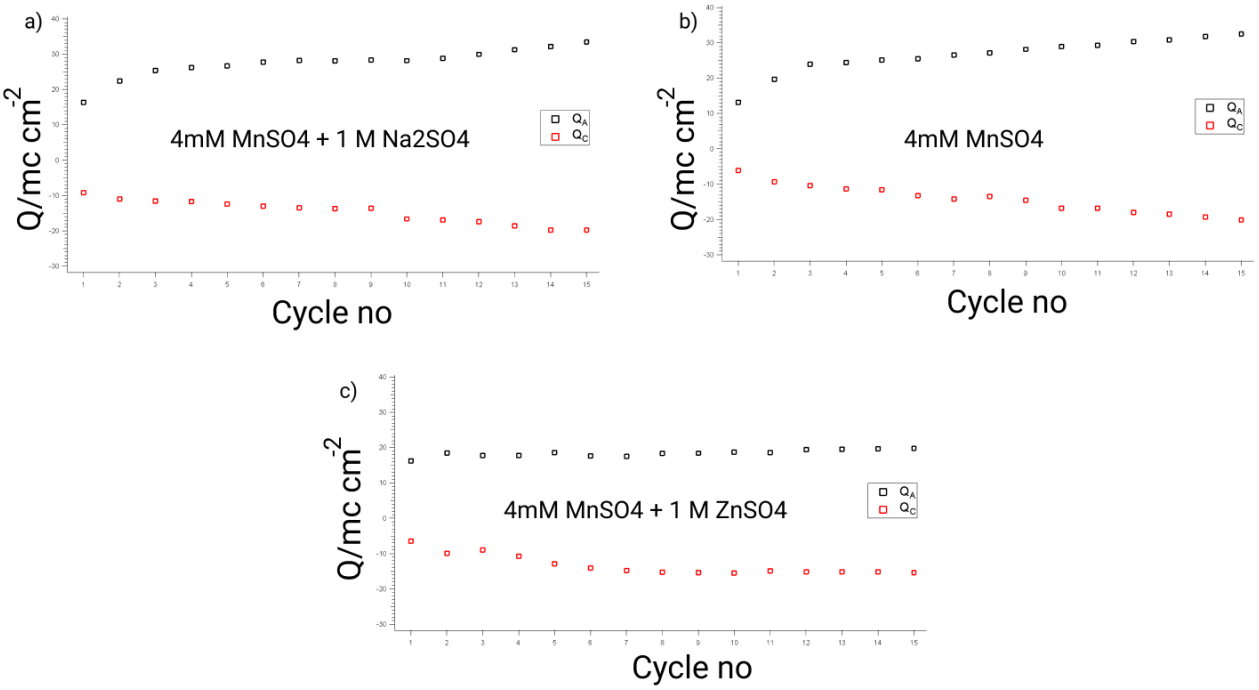

Figure 4.7 Anodic (Qa) and cathodic (Qc) coulombic charges corresponding to (a) the red curve (Figure 4.4); (b) the black curve (Figure 4.5); (c) the pink curve (Figure 4.6).

4.2.2 Impact of operating parameters on MnO_x electrodeposition

In Section 4.1, we have pinpointed that, even though MnO_x electrodeposition processes carried out in different conditions exhibits several commonalities that enable the joint discussion we proposed, nevertheless, the details of electrochemistry are notably influenced by operating parameters, such as pH, voltammetric voltage range, temperature and electrode substrate. In this section we carry out an systematic exploration of a portion of the electrodeposition parameter space, in view of providing background for our work on the impact of Zn^{2+} in neutral electrolytes.

4.2.2.1 Acidic electrolytes: a benchmark case

Since, as detailed in Section 4.1, limited electoanalytic work is available in neutral electrolytes, work in acidic ambient at a Pt electrode can be regarded as a benchmark case, against which to ground the investigation of Zn^{2+} effects. In Figure 4.8 we compare CVs measured in the MnO_2 formation range in neutral and acidic ambients. The effect of pH on the onset of Mn^{2+} oxidation (A2) as well as the subsequent redox processes is clearly coherent with thermodynamics. Specifically, in the acidic solution, peaks A2 and A1 come much closer than in the neutral one. The underlying mechanisms are discussed in full details in [42]. In particular, in the investigated potential range, all three cathodic processes C1-C3 are thermodynamically accessible only in the solution of lowest pH. In this case, as expected, most of Mn is reduced to the Mn(II)aq form and, in the anodic-going scan, the CV pattern is essentially the same as the first one, performed with a clean Pt electrode. Moreover, a tiny amount of some residual surface film formed towards the end of the cathodic-going scan is oxidized in the high-cathodic range of the anodic goings scans following the first one (feature A5). The small amout of Mn reduced in correspondence of peak C1 in the neutral electrolyte and in that containing 0.1 M H_2SO_4 is not enough to modify appreciably feature A2. Coherently with the literature [42], high temperature increases the anodic reaction rate (Figure 4.9) and bring peaks A1 and A2 to coincide. In addition, we found some impact - that has not been pointed out in the literature - of temperature in

the position of the c.d. maxima in the sequence of cathodic peaks as well as of the oxidation feature A5.

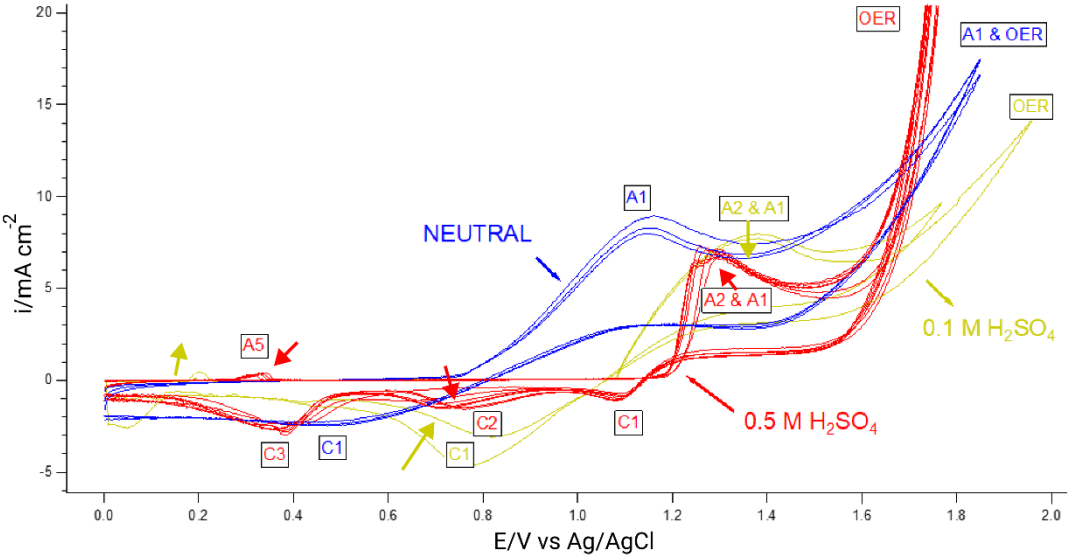

Figure 4.8 CVs measured in 0.1M $MnSO_4$ solutions, neutral and acidic (0.1 and 0.5 M H_2SO_4). Pt working electrode. Scan rate 5 mV/s. Temperature 22°C.

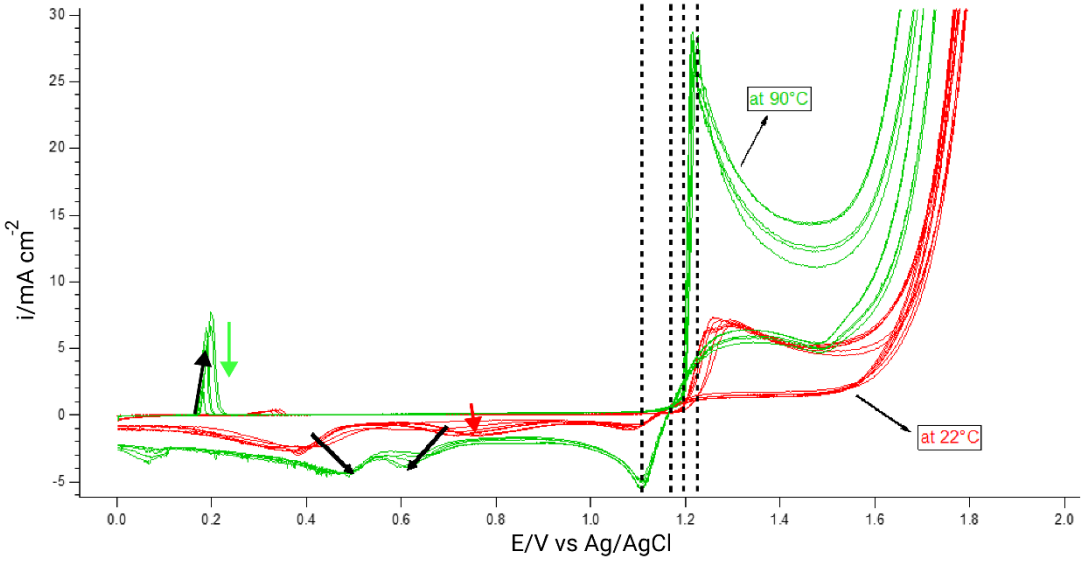

Figure 4.9 CVs measured in 0.1M $MnSO_4$ + 0.5 M H_2SO_4 acidic solution at 22 and 90°C. Pt working electrode. Scan rate 5 mV/s.

Addition of Zn^{2+} to the acidic electrolyte at room temperature (Figure 4.10) leads to an anodic shift of the $Mn(II)_{aq}$ oxidation threshold and to an increase in the separation of peaks A2 and A1, denoting some degree of inhibition of both the steps forming $Mn(III)_{aq}$ and $Mn(IV)_{solid}$. The cathodic branch is only marginally affected by the presence of Zn^{2+}, indicating that H^+ intercalation is the process controlling MnO_2 reduction. At 90°C, instead (Figure 4.11) the voltammetric pattern is not influenced by Zn^{2+} addition, apart from slight anticipation of the $Mn(II)_{aq}$ oxidation feature, an effect that is compatible with the enhancement of ionic conductivity. As in the room-temperature experiment, the cathodic-going scan is unaffected by adding Zn^{2+}.

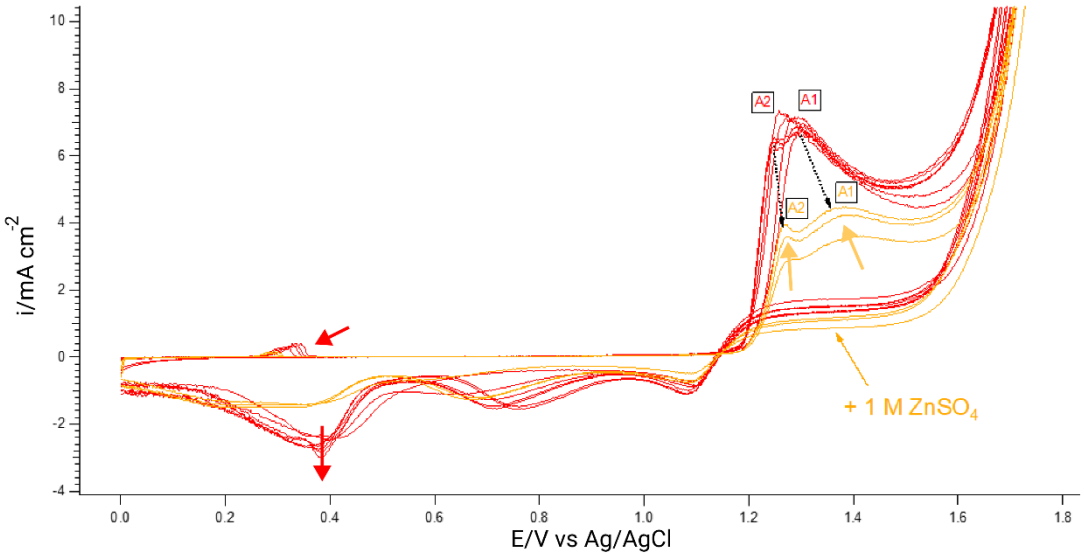

Figure 4.10 CVs measured in 0.1M $MnSO_4$ acidic solutions (0.5 M H_2SO_4) without and with addition of 1M $ZnSO_4$, at 22°C. Pt working electrode. Scan rate 5 mV/s.

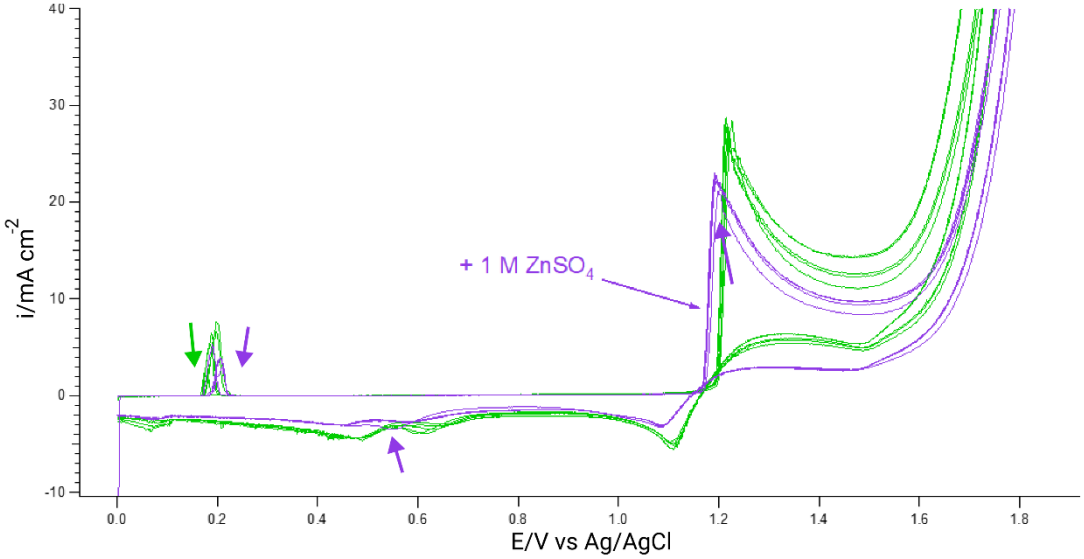

Figure 4.11 CVs measured in 0.1M $MnSO_4$ + 0.5 M H_2SO_4 acidic solution without and with addition of 1M $ZnSO_4$, at 90°C. Pt working electrode. Scan rate 5 mV/s.

4.2.2.2 Effect of the presence of Zn^{2+} of initial stages of MnO_x electrodeposition

The influence of adding 1M $ZnSO_4$ to the 0.1M $MnSO_4$ on the initial stages of electrodeposition have been studied following the first CV cycle at a clean Pt electrode (Figure 4.12). Even though Zn^{2+} effects on MnO_x electrodeposition develop after prolonged cycling (see Section 4.2.1, Figure 4.6), anticipation of peaks A2 and C1, is visible already from the first cycle also on Pt electrodes denoting interaction of Zn^{2+} with $Mn(III)_{solid}$ species.

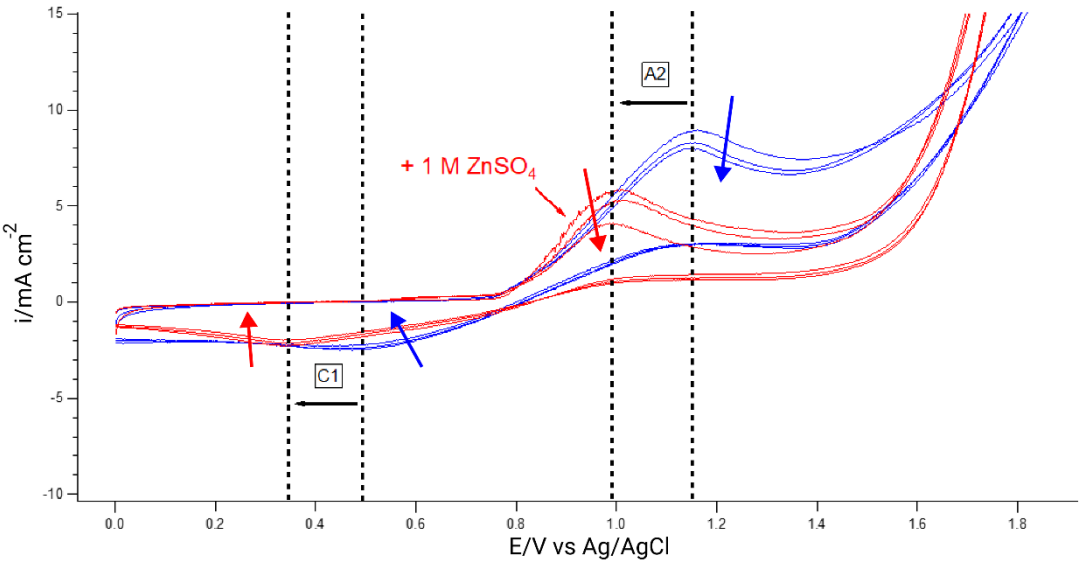

Figure 4.12 First CV cycles measured in neutral 0.1 M $MnSO_4$ solutions, without and with 1 M $ZnSO_4$ addition, in contact with Pt electrodes. 22°C, scan rate 5 mV/s.

4.2.2.3 Influence of electrode material of initial stages of MnO_x electrodeposition

The effect of employing Pt vs. GC electrodes in neutral 0.1 M $MnSO_4$ electrolyte, has been investigated by measuring the first anodic-going scan. The results reported in Figure 4.13 show that the impact of the electrode substrate on the LSV pattern – that is fully coherent with that commented in Section 4.2.1 – is negligible, while the catalytic effect of Pt on Mn^{2+} oxidation, highlighted in [42] for the acidic case is confirmed also with a neutral electrolyte.

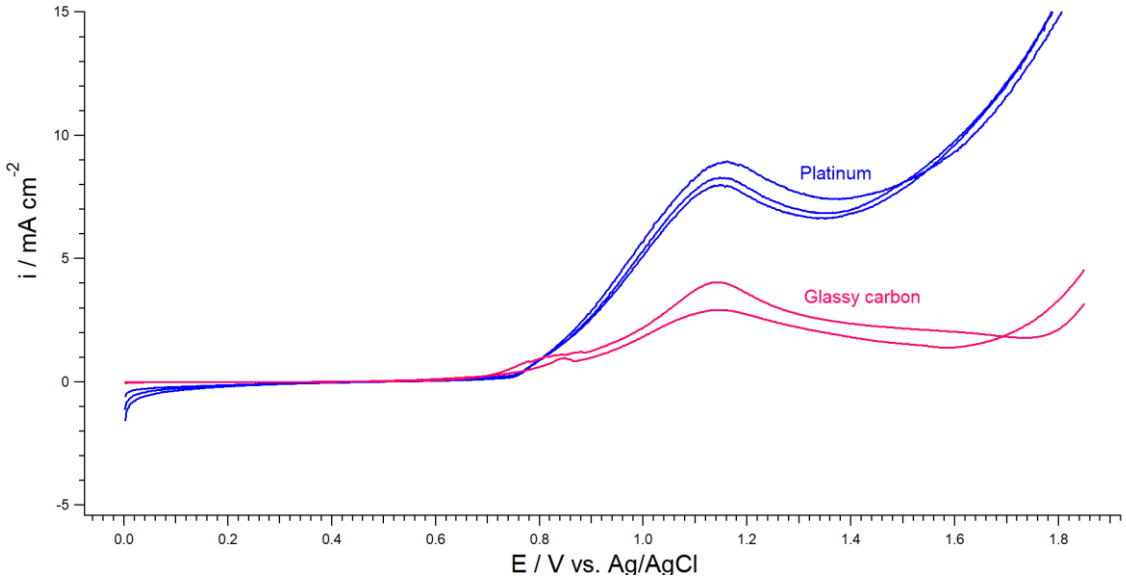

Figure 4.13 Anodic LSVs measured in neutral 0.1M $MnSO_4$ solutions in contact with GC and Pt electrodes. 22°C, scan rate 5 mV/s.

4.2.3 Electrochemical behaviour of electrodeposited in the ZIB operative range

4.2.3.1 Electrochemical measurements in three-electrode cells

4.2.3.1.1 MnO_x cycling in $MnSO_4$-free electrolytes

In order to assess the impact of Zn^{2+} on the electrochemical behaviour of MnO_x-based ZIB cathodes, we carried out cycling tests in the operating potential range. Specifically, we carried out tests in electrolytes without and with added Zn^{2+}, for MnO_x films electrodeposited from the electrolytes discussed in Section 4.2.1: the results are shown in Figures 4.14-16. In the case of MnOx grown from a $MnSO_4/Na_2SO_4$ electrolyte, a featureless and stable pseudocapacitive cycle can be observed with an Na_2SO_4 electrolyte (Figure 4.14a), while in the $ZnSO_4$ electrolyte the voltammetric pattern is quite different (Figure 4.14b): the first cycles shows a couple of peaks of C1/A2 types, the potentials of which correspond to the main peaks observed during electrodeposition from the $MnSO_4/ZnSO_4$ electrolyte, that we tentatively attributed to Zn^{2+} intercalation (Section 4.2.1). Interestingly, this couple of peaks fades out in the first few cycles. This result points out to the fact that, even though this characteristic couple of peaks correlates with the presence of Zn^{2+} in the electrolyte, stable cycles of the type observed in Figure 6 can be obtained only if $ZnSO_4$ and $MnSO_4$ are simultaneously present in the solution. Of course, deeper investigations are needed to gain a full understanding of this process, but it seems that some form of regeneration of the MnO_x structure is needed, making use of solution Mn^{2+}, in order to stabilize redox cycling in the presence of Zn^{2+}. Instead, the interaction of the MnO_x film with solution Zn^{2+} leads to some kind of irreversible transformation correlated with drastic loss of the initial capacity.

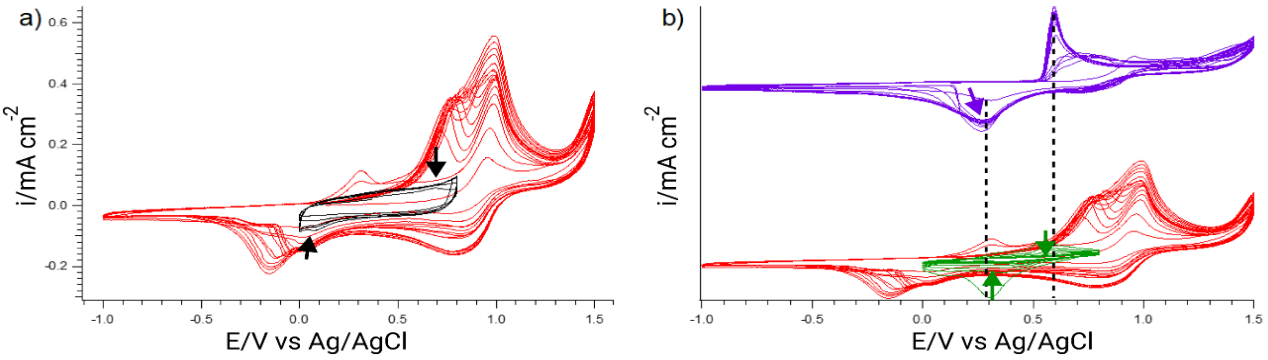

Figure 4.14 CVs measured in the operating range of a ZIB cathode, for a MnO_x film electrodeposited from a 4 mM $MnSO_4$ + 0.1 M Na_2SO_4 neutral solution. Test carried out in the following solutions: (a) black - 0.1 M Na_2SO_4; (b) green - 0.1 M $ZnSO_4$. The inset in Panel (b) shows the CV measured during electrodeposition from the 4 mM $MnSO_4$ + 0.1 M $ZnSO_4$ solution, for comparison.

The same type of behaviour is observed with a MnO_x film electrodeposited from the $MnSO_4$ solution (Figure 4.15), showing that the differences in the films grown in the absence and in the presence of Na_2SO_4 do not impact the interaction with Zn^{2+}. Instead, a profound difference in electrochemical behaviour is found for the MnO_x film electrodeposited from the $MnSO_4/ZnSO_4$ electrolyte. In the Na_2SO_4 electrolyte (Figure 4.16,a) the same type of pseudocapacitive behaviour is found, while in the presence of Zn^{2+} (Figure 4,16b) charge transfer processes are deactivated, possibly owing to the formation of an insulating surface phase right from the first CV cycle. Instead, if $MnSO_4$ and $ZnSO_4$ are both present in the electrolyte, stable cycling can be achieved also during ZIB operation: more details on this point will be provided in Section 4.2.3.2.

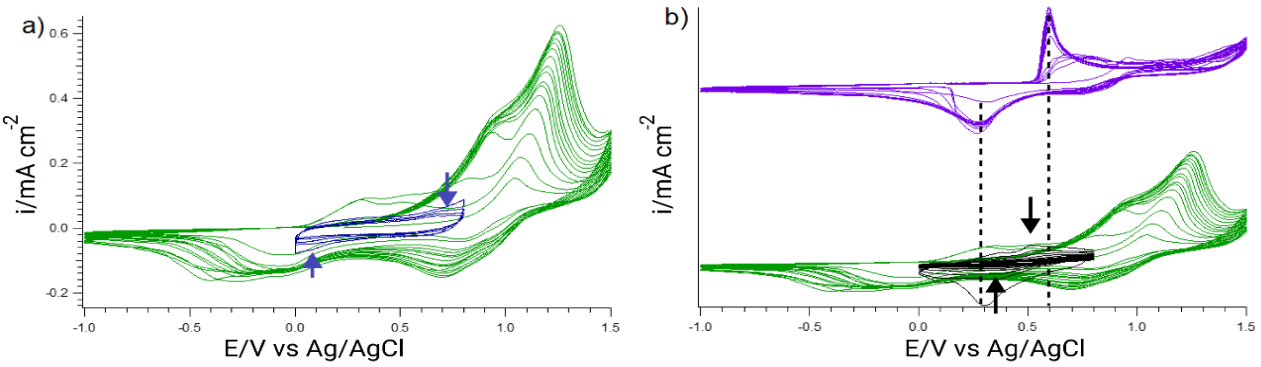

Figure 4.15 CVs measured in the operating range of a ZIB cathode, for a MnO_x film electrodeposited from a 4 mM $MnSO_4$ neutral solution. Test carried out in the following solutions: (a) blue - 0.1 M Na_2SO_4; (b) black - 0.1 M $ZnSO_4$. The inset in Panel (b) shows the CV measured during electrodeposition from the 4 mM $MnSO_4$ + 0.1 M $ZnSO_4$ solution, for comparison.

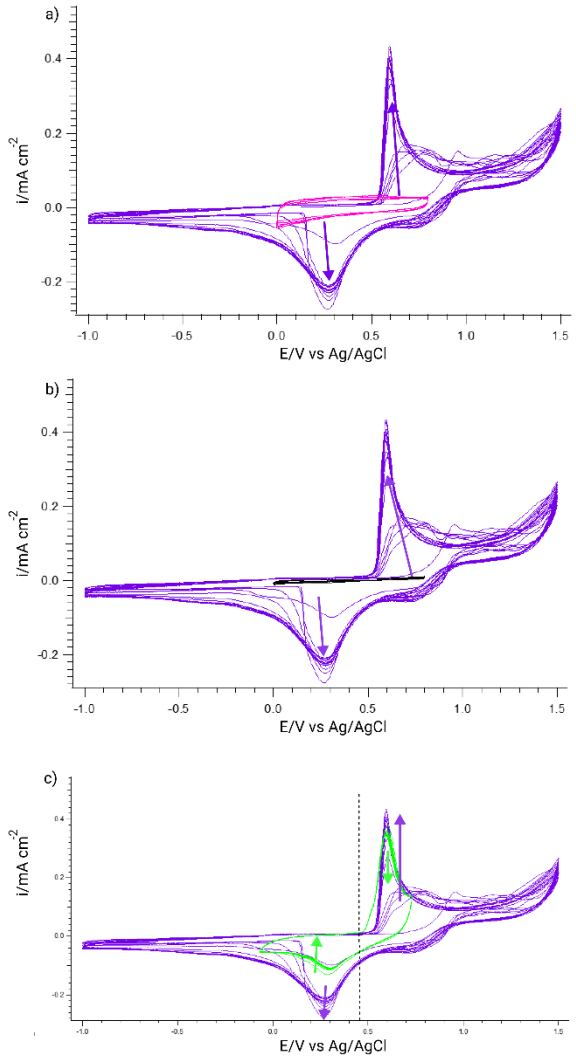

Figure 4.16 CVs measured in the operating range of a ZIB cathode, for a MnO_x film electrodeposited from a 4 mM $MnSO_4$ + 0.1 M $ZnSO_4$ neutral solution. Test carried out in the following solutions: (a) pink - 0.1 M Na_2SO_4; (b) black - 0.1 M $ZnSO_4$. (c), for comparison, we also show the CV measured in a split cell with an electrodeposited MnO_x cathode. CV (green) curve is shifted in cathodic direction (70 mV) due to CE polarization in the split cell. (for details, see Section 4.2.3.2).

4.2.3.1.2 MnO_x cycling in $MnSO_4$/$ZnSO_4$ electrolytes

In the previous subsection, we have observed a notable capacity fade in $ZnSO_4$ electrolytes, owing to an irreversible modification of the MnO_x matrix as a result of cycling in the presence of Zn^{2+}. The present subsection concentrates on the option of reactivating MnO_x in the ZIB operating range, by adding $MnSO_4$ in the electrolyte. In view of implementing electrodeposited electrodes into split cells and on the basis of the vanishing support effects highlighted in Section 4.2.2.3, we employed carbon paper electrodes. Electrodeposition as carried out from 0.2 M $MnSO_4$, 2M $ZnSO_4$ electrolytes with the galvanostatic/potentiostatic protocol detailed (See Chapter 2, Section 2.2.1.1). We run an extensive number of replicated experiments with different number of cycles (Figure 4.17,a), that yield a coherent picture. The CV patterns measured in the ZIB operating range are fully coherent with those studied in Section 4.2.1 and discussed in detail there (see Figures 4.6 and 4.16,b, for reference). The CV behaviour is dominated by features A2 and C1, corresponding to Zn(II) intercalation and deintercalation into and from MnO_2. Prolonged cycling shows a progressive capacity fade, related to some transient structural rearrangement that will have to be investigated further, till an asymptotic cycle is attained. The pristine capacity can be restored after a give cycling period, if the galvanostatic/potentiostatic protocol is repeated (for operating details, see the figure caption).

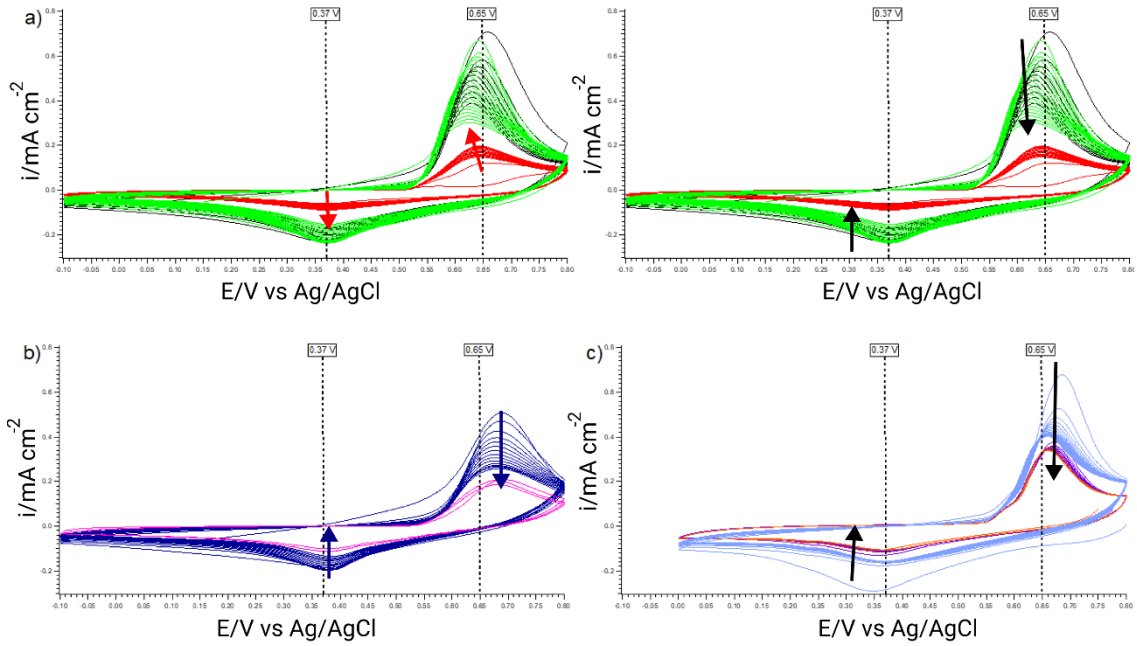

Figure 4.17 CVs measured in the operating range of a ZIB cathode, for a MnO_x film electrodeposited from and operated in a 0.2 M $MnSO_4$ + 2 M $ZnSO_4$ neutral solution. (a),(b) Carbon paper support, three electrode cell, Zn quasi-RE, Zn CE, at scan-rate 0.5 mV s^{-1}. Series of replicated tests (c) Same, but measured in a split-cell in two-electrode configuration with Zn anode, at scan-rate 2 mV s^{-1}. The lists of tests for CP0 sample: black (1st CV after 1st electrodeposition), red (2nd CV after 1st electrodeposition), and green (1st CV after 1st electrodeposition). The lists of tests for replicate CP1 sample: : blue (1st CV after 1st electrodeposition), pink (2nd CV after 1st electrodeposition). The lists of tests for replicate CP2 sample (in a split cell): purple (3rd CV after 1st electrodeposition), red (4th CV after 1st electrodeposition), and light blue (1st CV after 2nd electrodeposition).

4.2.3.1.3 Electrochemical measurements in split cells

CV experiments were finally carried out in split cells, containing MnO_x cathodes in the form of films electrodeposited from 0.2 M $MnSO_4$, 2M $ZnSO_4$ electrolytes onto carbon paper, as detailed in Chapter 3. The results are reported in Figure 4.17c. Overall, the electrochemical behaviour of this system is fully coherent with that observed in Subsection 4.2.3.1.2 and the same comments apply here. The experiments were repeated at different scan rates (Figure 4.18) and no essential impact was found, showing that intercalation/deintercalation is a fast process on the investigated timescale of cycling.

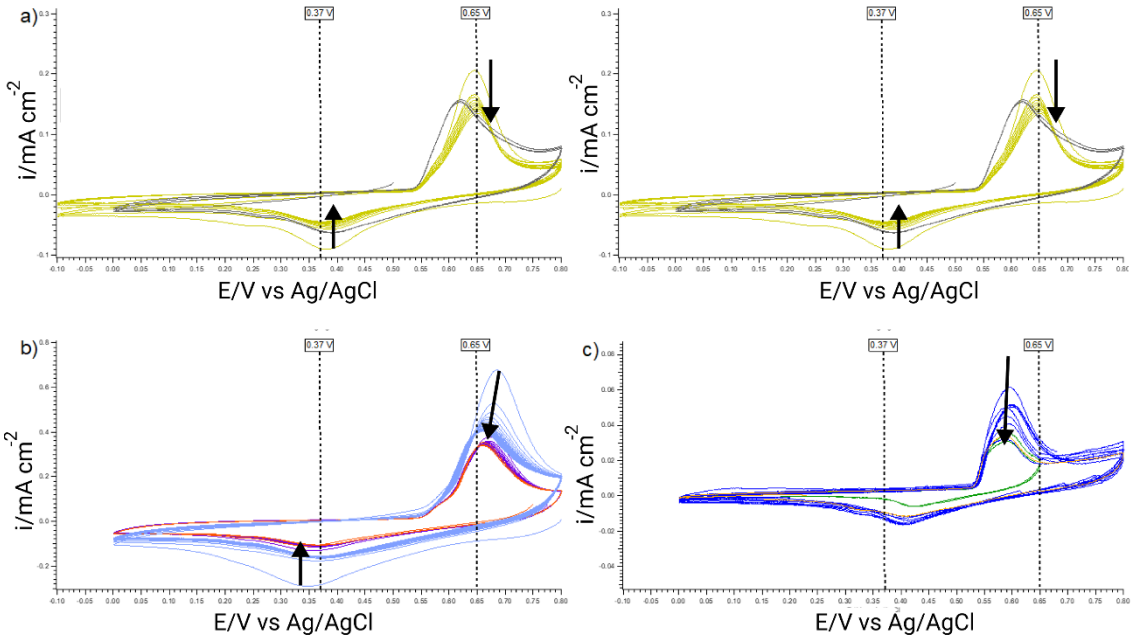

Figure 4.18 CVs measured in the operating range of a ZIB cathode, for a MnO_x film electrodeposited from and operated in a 0.2 M $MnSO_4$ + 2 M $ZnSO_4$ neutral solution in a split cell, at different scan rates 0.5 mV s^{-1}(a), 2 mV s^{-1}(b), 0.05 mV s^{-1}(c). The sequence of electrodeposition and cycling are indicated in the figures. The lists of tests for replicate CP2 sample (in a split cell): light green (1st CV after 1st electrodeposition), purple (3rd CV after 1st electrodeposition), red (4th CV after 1st electrodeposition), light blue (1st CV after 2nd electrodeposition), black (2nd CV after 2nd electrodeposition), dark green (3rd CV after 2nd electrodeposition), dark blue (4th CV after 2nd electrodeposition), orange (5th CV after 2nd electrodeposition).

In order to confirm the role of the joint presence of $MnSO_4$ and $ZnSO_4$ in the electrolyte, highlighted in Subsection 4.2.3.1.1, we carried out split-cell experiments separately in 0.1 M Na_2SO_4 and 1 M $ZnSO_4$ neutral solutions: the results are reported in Figure 4.19. In a way that is very similar to the results of Subsection 4.2.3.1.1, the pure Na_2SO_4 yields pseudocapacitive behaviour, similar to that found on the other experiments in Na_2SO_4 solutions (see Figures 4.14,a, 4.15,a and 4.16,a), while pure $ZnSO_4$ solutions do exhibit the characteristic A2/C1 peak couple, but with rapid capacity fade (see Figures 4.14,b and 4.15,b). The same comments of Subsection 4.2.3.1.1 apply also here.

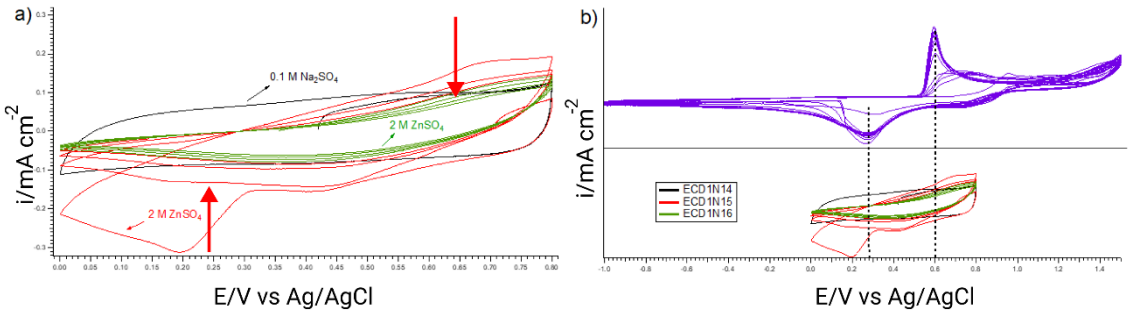

Figure 4.19 CVs measured in the operating range of a ZIB cathode, for a MnO_x film electrodeposited from a 0.2 M $MnSO_4$ + 1 M $ZnSO_4$ neutral solution on carbon paper. (a) Test CVs are carried out in the following solutions: 0.1M Na_2SO_4 (black), and 2 M ZnSO4 (red and green). In Panel (b), for comparison, we also show the CVs for electrodeposition of MnOx from 4 mM $MnSO_4$ + 0.1 M $ZnSO_4$ neutral solution (purple). The lists of tests for replicate CP3 sample: black (1st CV after 1st electrodeposition), red (2nd CV after 1st electrodeposition), and green (3rd CV after 1st electrodeposition).

4.3 Impact of Zn^{2+} on the electrochemical behaviour of hydrothermally synthesized α-MnO_2 in near-neutral aqueous solution

In this Section, we report on the electrochemical performance of drop-cast α-MnO_2 based electrodes, fabricated as detailed in (Chapter 2 - Section 2.2.2). This material is generally employed for ZAB cathodes (e.g. [74]): for this reason, as a benchmark, we studied first its CV behaviour in the 0.1 M KOH electrolyte typically used for electrocatalytic ORR tests, though here in the absence of O_2, as is the case in ZIBs. The CV in deaerated alkaline ambient (Figure 4.20,a) is compatible with the mechanisms discussed in Section 4.1.4: the complex cathodic peak encompasses proton intercalation of MnO_2 and reduction to mixed poorly reversible MnOOH/$Mn(OH)_2$ while the anodic peak is controlled by deintercalation of $HMnO_2$. In neutral 0.1 M Na_2SO_4 (Figure 4.20,b), the cathodic behaviour is controlled by the C3-type process, generating $Mn(II)_{aq,solid}$ while the initial anodic behaviour comprises the classical sequence of processes leading from $Mn(II)_{aq/solid}$ all the way to MnO_2. Reduction of the c.d. with cycling denotes progressive redox deactivation of cryptomelane, probably due to some structural rearrangements that warrant more insightful investigation. If only Zn^{2+} is present in the solution (Figure 4.20,c), a small C1-type feature is seen, followed by a sharp C2-type peak, dominate the cathodic branch in the first cycle, that disappears upon further cycling. This behaviour is similar to that of electrodeposited MnO_x from $MnSO_4$ and $Na_2SO_4/MnSO_4$ solutions, cycled in $ZnSO_4$ neutral solutions, denoting irreversible intercalation. In the case of α-MnO_2, the anodic processes are suppressed after the first cathodic-going scan. If both $ZnSO_4$ and $MnSO_4$ are present in the solution (Figure 4.20,d), again a C1-type peak is found to dominate the first cathodic scan, followed, going more cathodic, by a sequence of cathodic peaks. The results of cycling in the ZIB voltage range with Na_2SO_4, $MnSO_4$ and $ZnSO_4$ neutral electrolytes, compared with the more extended ranges, are shown in Figure 20. Owing to the specific peak positions found with α-MnO_2, the ZIB operating range lies a range of limited redox activity. In analogy with the what we observed with electrodeposited MnO_x, (Section 4.2.3), in neutral Na_2SO_4 (Figure 4.21,a) and $MnSO_4$ solutions (Figure 4.21,b), pseudocapacitive behaviour is observed, that is instead lost in the $ZnSO_4$ electrolyte (Figure 4.21,c). As expected, by slightly extending the cathodic range, the irreversible intercalation peak can be observed.

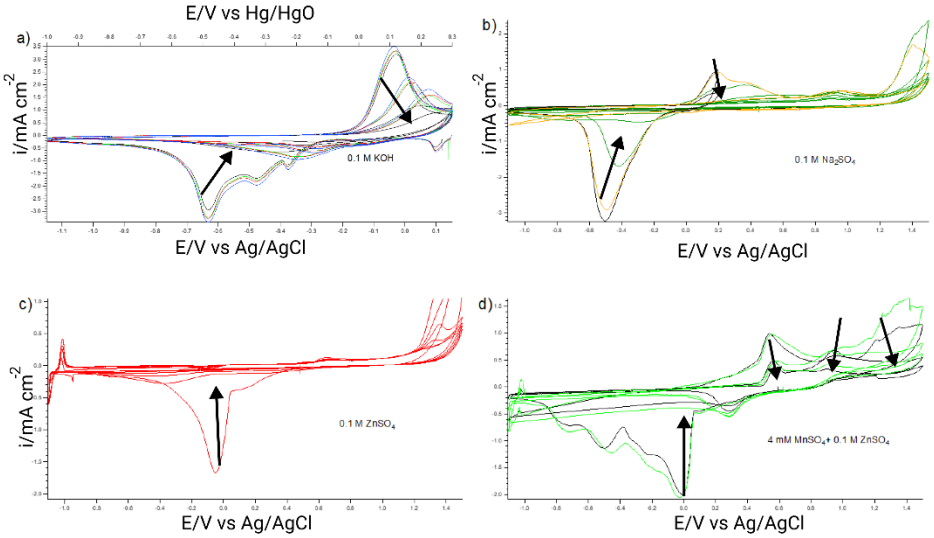

Figure 4.20 CVs of alpha-MnO_2 based electrodes in different electrolytes: (a) 0.1 M KOH (replicating first CV - black); (b) neutral 0.1 M Na_2SO_4 (replicating first CV - orange); (c) neutral 0.1 M $ZnSO_4$; (d) neutral 0.1 M $ZnSO_4$ + 4 mM $MnSO_4$ (replicating first CV - black).

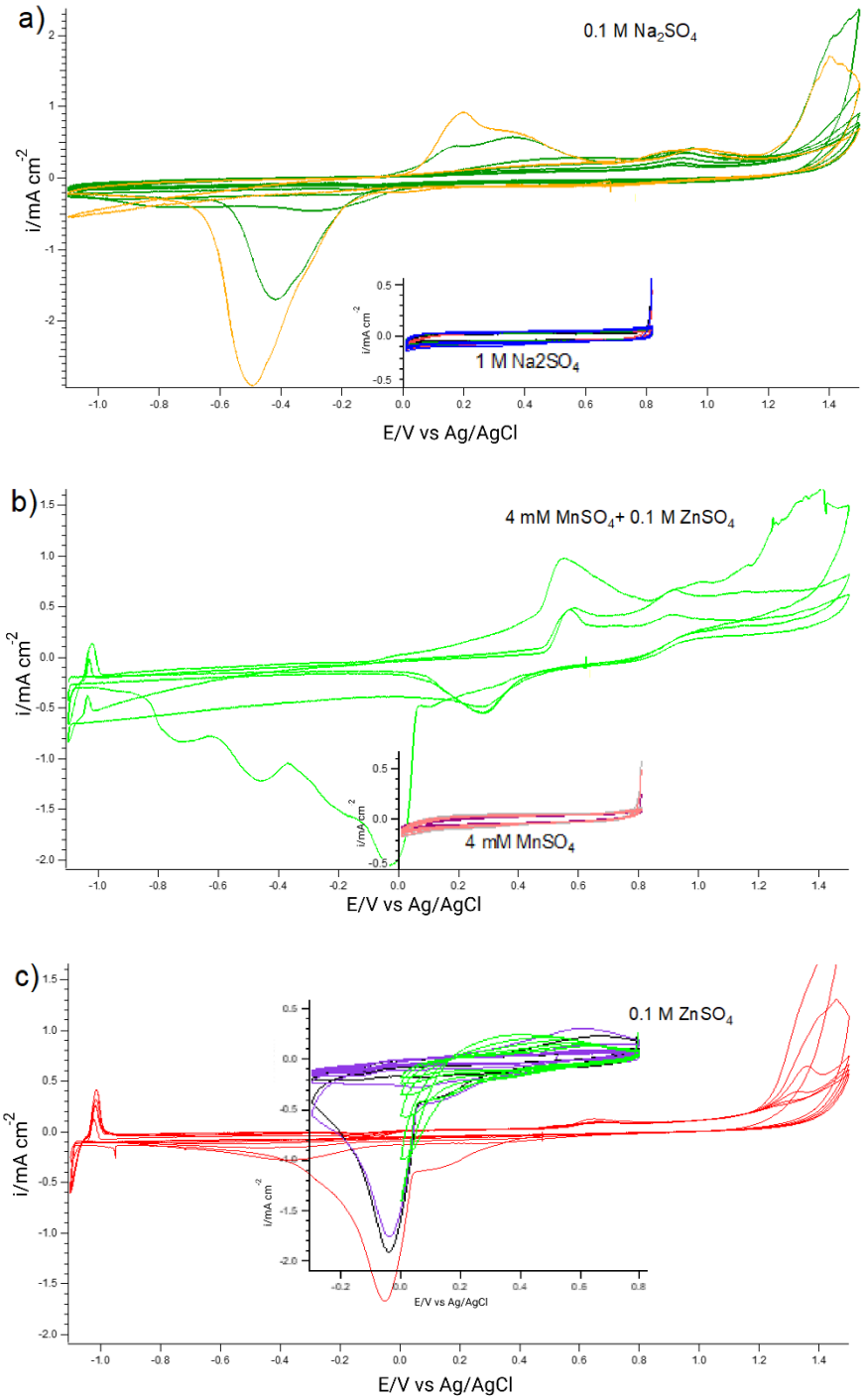

Figure 4.21 CVs in the ZIB operating range for alpha-MnO_2 based electrodes in different neutral electrolytes: 0.1 M Na_2SO_4 (a); 4 mM $MnSO_4$ (b); 0.1 M $ZnSO_4$ (c), compared with the corresponding CVs, measured in the extended voltage ranges, presented in Figure 4.20.

Though sharing some common aspects, the redox of electrodeposited MnO_x and hydrothermally grown α-MnO_2 undergo different types of processes upon voltammetric cycling in the presence of Zn^{2+}. Electrodeposited MnO_x supports, reversible intercalation of Zn^{2+} if Mn^{2+} is present in the solution, suppressing irreversible modifications leading to cathode deactivation. With α-MnO_2, the cycling behaviour is improved in Zn^{2+}/Mn^{2+} solutions with respect to pure Zn^{2+} ones, but rapid capacity loss occurs in any case.

Conclusion

The purpose of this thesis was to assess the role of the interaction of MnOx-based ZIB cathodes, electrodeposited and hydrothermally synthesized, with electrolyte components that are typical of ZIBs on their electrochemical behaviour. Specifcially, I focused on Mn^{2+}, Na^{+} and Zn^{2+}. The methodology for used techniques was prescribed and the protocols are detailed in Chapter 2, both electrochemical and physicochemical characterization results were provided in Chapter 3, and a discussion of the corresponding results were given in Chapter 4.

From the results reported in this manuscript, the following conclusions can be underlined:

The electrochemical oxidation mechanism of Mn^{2+} cations leading to the electrodeposition of birnessite-type MnO_2 films is a multistep reaction. The chemical composition of the electrodeposition solution greatly affect the electrodeposition process of MnO_2 films. H^{+}-intercalation process of features is energetically more favoured and less extensive reduction of the electrodeposit to Mn(II) takes place in electrolytes with added Na^{+}. In addition, full oxidation of the film requires higher potentials in Na^{+}-free electrolyte, possibly owing to the progressive growth of poorly conducting material. When Zn^{2+} was added to the Mn^{2+} solution, significant changes in the electrochemical behavior of Mn occurred during electrodeposition. The CVs do not tend to diminish, and the anodic and cathodic charges consumed are quite equivalent. This situation is consistent with Zn^{2+} intercalation/deintercalation without the formation of layers that would tend to inhibit the process. The influence of Na^{+} and Zn^{2+} insertion in MnO_2 films during electrodeposition process is real but limited in our experimental conditions. Further investigations are required to confirm the intercalation mechanism of the electrodeposited MnO_2 films.

To place electroanalytic work in neutral electrolytes in context, I also analyzed the acidic environment as a benchmark before the further investigation of Zn^{2+} effects. First, I found that the influence of pH on both the initiation of Mn^{2+} oxidation and subsequent redox processes is fully consistent with thermodynamics. The presence of Zn^{2+} has a negligible effect on the reduction of MnO_2 at both ambient and elevated temperatures, indicating that H^{+} intercalation is the controlling process. The effect of Zn^{2+} has been also observed on the initial stage of MnO_x electrodeposition on Pt electrode. Furthermore, the electrode material has a distinct impact on the initial stages of MnO_x electrodeposition.

We conducted cycling tests in the operating potential range to determine the effect of Na^{+} and Zn^{2+} on the electrochemical behavior of MnO_x-based ZIB cathodes. While the CV patterns measured in Na^{+} solutions yields pseudocapacitive behaviour, the ones in Zn^{2+} solutions were dominated by distinct an anodic and a cathodic current peak, corresponding to Zn(II) intercalation and deintercalation into and from MnO_2. It appears that some form of regeneration of the MnOx structure is needed, making use of solution Mn^{2+}, in order to stabilize redox cycling in the presence of Zn^{2+}. This is consistent with the view that more stable cycles could be obtained only if $ZnSO_4$ and $MnSO_4$ are simultaneously present in the solution. Instead, the interaction of the MnO_x film solution with Zn^{2+} in the absence of Mn^{2+} leads to irreversible transformations, correlated with drastic loss of the initial capacity. In the case of α-MnO_2, the anodic processes are suppressed after the first cathodic-going scan. Owing to the specific peak positions found with α-MnO_2, the ZIB operating range lies a range of limited redox activity.

Redox mechanism of manganese is highly reversible in Na^{+}-alone solution, as we observed the loss of Mn by dissolution under the form of $Mn(II)_{aq}$ and then some Mn is regained, but oxidation of

$Mn(II)_{aq}$ back to solid MnO_x, after polarization at 0.1 and 0.9 V, respectively. The EDS results highlight the potential of Na^+ intercalation/deintercalation mechanism. When the reduction potential alone is applied, as well as when the reduction and oxidation potentials are applied consecutively, after adding Zn^{2+} into Na^+ solution, the patterns of flaky/platelet phase were appearing in accordance with the SEM image observed. This flaky/platelet porous substances can be indexed to ZHS formation, which contains Zn as well as a high proportion of S. This new phase is highly irreversible, since it stays detectable after successive polarization at 0.1 and 0.9 V. Unlike in Na^+-alone solutions, lower amounts of Mn are instead found after polarizing first at 0.1 V then at 0.9V in the Na^+/Zn^{2+} solution. Together, these findings support the view that MnO_x-based ZIB cathodes suffer from rapid capacity decay in Zn^{2+} solutions.

Finally, birnessite-type MnO_2 film appear to be promising candidate as a cathode material for ZIB application, as they are showing presence of reversible intercalation of $Zn^{2+}$and high stability in a mild $ZnSO_4$ aqueous electrolyte with a $MnSO_4$ additive, which suppresses irreversible modifications leading to cathode deactivation. With hydrothermally grown cryptomelane-type α-MnO_2, the cycling behaviour is improved in Zn solutions with respect to pure Zn ones, but rapid capacity loss was still observed in any case. The structural and morphological evolution of α-MnO_2 electrodes have been comprehensively investigated by XRD, Raman and SEM-EDS mapping, which explains the electrochemical behaviour and reveals an alternative conversion reaction mechanism of ZHS, which can be attributed to cathode deactivation, other than Zn^{2+} ion intercalation into MnO_2.

Bibliography

[1] B. Scrosati, “Power sources for portable electronics and hybrid cars: Lithium batteries and fuel cells,” *Chem. Rec.*, vol. 5, no. 5, pp. 286–297, 2005, doi: 10.1002/tcr.20054.

[2] Z. Yang, J. Zhang, M. C. W. Kintner-meyer, X. Lu, D. Choi, and J. P. Lemmon, “Electrochemical Energy Storage for Green Grid: Status and Challenges,” *ECS Meet. Abstr.*, pp. 3577–3613, 2011, doi: 10.1149/ma2011-02/4/155.

[3] C. E. Sandy Thomas, “How green are electric vehicles?,” *Int. J. Hydrogen Energy*, vol. 37, no. 7, pp. 6053–6062, 2012, doi: 10.1016/j.ijhydene.2011.12.118.

[4] D. Larcher and J. M. Tarascon, “Towards greener and more sustainable batteries for electrical energy storage,” *Nat. Chem.*, vol. 7, no. 1, pp. 19–29, 2015, doi: 10.1038/nchem.2085.

[5] X. Luo, J. Wang, M. Dooner, and J. Clarke, “Overview of current development in electrical energy storage technologies and the application potential in power system operation,” *Appl. Energy*, vol. 137, pp. 511–536, 2015, doi: 10.1016/j.apenergy.2014.09.081.

[6] F. Report, “EPRI-DOE Handbook of Energy Storage for Transmission & Distribution Applications,” no. December, 2003.

[7] M. Li, J. Lu, Z. Chen, and K. Amine, “30 Years of Lithium-Ion Batteries,” vol. 1800561, pp. 1–24, 2018, doi: 10.1002/adma.201800561.

[8] H. Kim, J. Hong, K. Park, H. Kim, S. Kim, and K. Kang, “Aqueous Rechargeable Li and Na Ion Batteries,” 2014.

[9] L. H. Pan He, Yueli Quan, Xu Xu, Mengyu Yan,* Wei Yang, Qinyou An and and L. Mai, “High-Performance Aqueous Zinc–Ion Battery Based on Layered H 2 V 3 O 8 Nanowire Cathode,” vol. 1702551, pp. 1–7, 2017, doi: 10.1002/smll.201702551.

[10] A. J. Bard, “Electrochemical Methods: Fundamentals and Applications.” Wiley New York, 1980.

[11] S. K. Lower, “Electrochemistry: a Chem1 Supplement Text.”

[12] C. Xu, B. Li, H. Du, and F. Kang, “Energetic Zinc Ion Chemistry : The Rechargeable Zinc Ion Battery ** Angewandte,” no. 3, pp. 933–935, 2012, doi: 10.1002/anie.201106307.

[13] P. Yu, Y. Zeng, H. Zhang, M. Yu, Y. Tong, and X. Lu, “Flexible Zn-Ion Batteries : Recent Progresses and Challenges,” vol. 1804760, pp. 1–27, 2022, doi: 10.1002/smll.201804760.

[14] X. Zeng, J. Hao, Z. Wang, J. Mao, and Z. Guo, “Recent Progress and Perspectives on Aqueous Zn-based Rechargeable Batteries with Mild Aqueous Electrolytes,” *Energy Storage Mater.*, 2019, doi: 10.1016/j.ensm.2019.04.022.

[15] X. Jia, C. Liu, Z. G. Neale, J. Yang, and G. Cao, “Active Materials for Aqueous Zinc Ion Batteries : Synthesis , Crystal Structure , Morphology , and Electrochemistry,” 2020.

[16] J. Shin, J. K. Seo, R. Yaylian, A. Huang, and Y. S. Meng, “A Review on Mechanistic Understanding of MnO2 in Aqueous Electrolyte for Electrical Energy Storage Systems,” *Int. Mater. Rev.*, vol. 0, no. 0, pp. 1–32, 2019, doi: 10.1080/09506608.2019.1653520.

[17] G. J. Browning and S. W. Donne, “Proton diffusion in γ-manganese dioxide,” pp. 871–878, 2005, doi: 10.1007/s10800-005-4738-1.

[18] M. H. Alfaruqi *et al.*, “Electrochemically Induced Structural Transformation in a γ - MnO 2

Cathode of a High Capacity Zinc-Ion Battery System," 2015, doi: 10.1021/cm504717p.

[19] B. Lee, C. S. Yoon, H. R. Lee, K. Y. Chung, B. W. Cho, and S. H. Oh, "Electrochemically-induced reversible transition from the tunneled to layered polymorphs of manganese dioxide," vol. 2, pp. 1–8, 2014, doi: 10.1038/srep06066.

[20] W. Sun *et al.*, "Zn/MnO 2 Battery Chemistry With H + and Zn 2+ Coinsertion," pp. 13–16, 2017, doi: 10.1021/jacs.7b04471.

[21] H. Pan *et al.*, "Reversible aqueous zinc/manganese oxide energy storage from conversion reactions," vol. 1, no. April, pp. 1–7, 2016, doi: 10.1038/NENERGY.2016.39.

[22] X. Guo, J. Zhou, C. Bai, X. Li, and G. Fang, "Zn / MnO 2 battery chemistry with dissolution-deposition mechanism," *Mater. Today Energy*, vol. 16, p. 100396, 2020, doi: 10.1016/j.mtener.2020.100396.

[23] J. 0. Besenhard, *Handbook of Battery Materials*. Wiley-VCH.

[24] W. Zhou, K. Davey, and S. Qiao, "An Electrolytic Zn-MnO2 Battery Demonstrated for High-Voltage and Scalable Energy Storage," *Angew. Chemie*, doi: 10.1002/anie.201904174.

[25] M. Nakayama, Ã. S. Konishi, A. Tanaka, and K. Ogura, "A Novel Electrochemical Method for Preparation of Thin Films of Layered Manganese Oxides," vol. 33, no. 6, pp. 670–671, 2004, doi: 10.1246/cl.2004.670.

[26] M. Nakayama, A. Tanaka, Y. Sato, T. Tonosaki, and K. Ogura, "Electrodeposition of Manganese and Molybdenum Mixed Oxide Thin Films and Their Charge Storage Properties," no. 17, pp. 5907–5913, 2005.

[27] M. Nakayama, M. Fukuda, S. Konishi, and T. Tonosaki, "Effects of reaction parameters on the electrochemical formation of multilayer films composed of manganese oxides and tetra-alkylammonium ions," 2006, doi: 10.1557/JMR.2006.0385.

[28] M. Nakayama, R. Hoyashita, H. Komatsu, and E. Muneyama, "Immobilization of Methylviologen between Well-Ordered Multilayers of Manganese Oxide during Their Electrochemical Assembly," no. 12, pp. 3462–3465, 2007.

[29] N. Larabi-gruet, S. Peulon, A. Lacroix, and A. Chauss, "Electrochimica Acta Studies of electrodeposition from Mn (II) species of thin layers of birnessite onto transparent semiconductor," vol. 53, pp. 7281–7287, 2008, doi: 10.1016/j.electacta.2008.03.080.

[30] M. Barak, *Electrochemical power sources : primary and secondary batteries*. 1980.

[31] A. J. Bard, *Encyclopedia of electrochemistry of the elements, vol. 1*. 1973.

[32] S. Bodoardo and J. Brenet, "ELECTROCHEMICAL BEHAVIOUR OF MnO2 ELECTRODES IN SULPHURIC ACID SOLUTIONS," vol. 39, no. 13, 2004.

[33] S. Pang, M. A. Anderson, and T. W. Chapman, "Novel Electrode Materials for Thin-Film Ultracapacitors : Comparison of Electrochemical Properties of Sol-Gel-Derived and Electrodeposited Manganese Dioxide," vol. 147, no. 2, pp. 444–450, 2000.

[34] M. Pourbaix, "Atlas of Electrochemical Equilibria in Aqueous Solutions."

[35] R. G. . C. E. B. Compton, *Understanding Voltammetry, 3rd Edition*. Word Scientific.

[36] E. Smith and G. Dent, "Modern Raman Spectroscopy – A Practical Approach," p. 2005, 2005, doi: 10.1002/jrs.1320.

[37] W. D. Callister Jr and D. G. Rethwisch, "Fundamentals of Material Science and Engineering," 8th ed., Wiley New York.

[38] N. Birks, G. H. Meier, and F. S. Pettit, *Introduction to the High Temperature Oxidation of Metals*, 2nd ed. Cambridge University Press, 2006.

[39] N. Israelsson, "High Temperature Oxidation and Chlorination of FeCrAl Alloys," 2014.

[40] S. Karlsson, “High Temperature Corrosion of Stainless Steels,” 2011.

[41] S. Rodrigues, N. Munichandraiah, and A. K. Shukla, “A cyclic voltammetric study of the kinetics and mechanism of electrodeposition of manganese dioxide,” vol. 28, pp. 1235–1241, 1998.

[42] C. J. Clarke, G. J. Browning, and S. W. Donne, “An RDE and RRDE study into the electrodeposition of manganese dioxide,” vol. 51, no. March, pp. 5773–5784, 2006, doi: 10.1016/j.electacta.2006.03.013.

[43] M. Huynh, D. K. Bediako, Y. Liu, and D. G. Nocera, “Nucleation and Growth Mechanisms of an Electrodeposited Manganese Oxide Oxygen Evolution Catalyst,” 2014.

[44] M. F. Dupont and S. W. Donne, “Electrochimica Acta Nucleation and Growth of Electrodeposited Manganese Dioxide for Electrochemical Capacitors,” *Electrochim. Acta*, vol. 120, pp. 219–225, 2014, doi: 10.1016/j.electacta.2013.12.014.

[45] S. Nijjer, J. Thonstad, and G. M. Haarberg, “Oxidation of manganese (II) and reduction of manganese dioxide in sulphuric acid,” vol. 46, pp. 395–399, 2000.

[46] J. A. Lee, W. C. Maskell, and F. L. Tye, “J. Electroanal. Chem., 110 (1980) 145--158 ©,” vol. 110, pp. 145–158, 1980.

[47] E. S. S. A and W. C. Maskell, “Elecrroanal. Chem., 198 (1985) 127-137,” vol. 198, no. 1985, pp. 127–137, 1986.

[48] J. S. Ko, M. B. Sassin, J. F. Parker, D. R. Rolison, and J. W. Long, “Combining battery-like and pseudocapacitive charge storage in 3D MnOx@carbon electrode architectures for zinc-ion cells,” 2017, doi: 10.1039/C7SE00540G.

[49] C. M. Julien, M. Massot, and C. Poinsignon, “Lattice vibrations of manganese oxides Part I . Periodic structures,” vol. 60, pp. 689–700, 2004, doi: 10.1016/S1386-1425(03)00279-8.

[50] T. Gao, H. Fjellvåg, and P. Norby, “Analytica Chimica Acta A comparison study on Raman scattering properties of ␣ - and □ -MnO 2,” vol. 648, pp. 235–239, 2009, doi: 10.1016/j.aca.2009.06.059.

[51] T. Gao, M. Glerup, F. Krumeich, R. Nesper, H. Fjellvåg, and P. Norby, “Microstructures and Spectroscopic Properties of Cryptomelane-type Manganese Dioxide Nanofibers,” pp. 13134–13140, 2008.

[52] J. E. Post, D. A. Mckeown, and P. J. Heaney, “Raman spectroscopy study of manganese oxides : Tunnel structures,” vol. 105, no. August, pp. 1175–1190, 2020.

[53] D. Mckeown and P. J. Heaney, “Raman spectroscopy study of manganese oxides : Layer structures,” no. March, 2021, doi: 10.2138/am-2021-7666.

[54] M. Xiong, M. P. Clark, M. Labbe, and D. G. Ivey, “A horizontal zinc-air battery with physically decoupled oxygen evolution / reduction reaction electrodes,” *J. Power Sources*, vol. 393, no. April, pp. 108–118, 2018, doi: 10.1016/j.jpowsour.2018.05.004.

[55] H. Li, B. Song, W. J. Wang, and X. L. Chen, “Facile synthesis , thermal , magnetic , Raman characterizations of spinel structure ZnMn2O4,” vol. 130, pp. 39–44, 2011, doi: 10.1016/j.matchemphys.2011.04.072.

[56] Y. Xie *et al.*, “Effect of the crystal plane figure on the catalytic performance of MnO2 for the total oxidation of propane,” *CrystEngComm*, vol. 17, pp. 3005–3014, 2015, doi: 10.1039/C5CE00058K.

[57] M. Ndjeri, S. Peulon, S. Bach, and A. Chaussé, “Electrochimica Acta Studies on the reduction of birnessite thin layers : Influence of medium,” *Electrochim. Acta*, vol. 56, no. 24, pp. 8564–8570, 2011, doi: 10.1016/j.electacta.2011.07.054.

[58] J. K. Seo, J. Shin, and K. Y. Chung, “Intercalation and Conversion Reactions of Nanosized β-

MnO 2 Cathode in the Secondary Zn / MnO 2 Alkaline Battery," *Am. Chem. Soc.*, 2018, doi: 10.1021/acs.jpcc.7b11685.

[59] S. Ding *et al.*, "Progressive 'Layer to Hybrid Spinel/Layer' Phase Evolution with Proton and Zn2+ Co-intercalation to Enable High Performance of MnO2-Based Aqueous Batteries," *Am. Chem. Soc.*, 2021.

[60] J.-P. Petitpierre, C. Comninellis, and E. Plattner, "Oxydation du MnSO4 en dioxyde de manganese dans H2SO4 30%.," *Electrochim. Acta*, vol. 35, no. 1, 1990.

[61] B. L. Wu, D. Lincot, and L. T. Yu, "Voltammetric and electrogravimetric study of manganese dioxide thin film electrodes . Part 1 . Electrodeposited films," vol. 420, pp. 159–165, 1997.

[62] Z. Rogulski, H. Siwek, I. Paleska, and A. Czerwin, "Electrochemical beha v ior of manganese dioxide on a gold electrode," vol. 543, pp. 175–185, 2003, doi: 10.1016/S0022-0728(03)00045-7.

[63] Y. Chabre *et al.*, "STRUCTURAL AND ELECTROCHEMICAL PROPERTIES OF THE PROTON / y-Mn02 SYSTEM," vol. 23, no. 94, 1995.

[64] J. Mcbreen, "THE OF P-Mn02 AND ELECTROLYTE *," no. Ii, pp. 4–8.

[65] M. Minakshi *et al.*, "The Zn ? − ? MnO 2 Battery : The Influence of Aqueous LiOH and KOH Electrolytes on the Intercalation Mechanism service The Zn – MnO 2 Battery : The Influence of Aqueous LiOH and KOH Electrolytes on the Intercalation Mechanism," vol. 11, no. 8, pp. 2–7, 2008, doi: 10.1149/1.2932056.

[66] M. Minakshi, M. Blackford, and M. Ionescu, "Characterization of alkaline-earth oxide additions to the MnO 2 cathode in an aqueous secondary battery," *J. Alloys Compd.*, vol. 509, no. 20, pp. 5974–5980, 2011, doi: 10.1016/j.jallcom.2011.03.044.

[67] J. B. Leriche, L. Seguin, E. Wang, R. Moses, R. Patrice, and B. Ge, "Understanding the Second Electron Discharge Plateau in MnO 2 -Based Alkaline Cells," pp. 448–455, 2001, doi: 10.1149/1.1362539.

[68] N. D. Ingale, J. W. Gallaway, M. Nyce, A. Couzis, and S. Banerjee, "Rechargeability and economic aspects of alkaline zinc e manganese dioxide cells for electrical storage and load leveling," *J. Power Sources*, vol. 276, pp. 7–18, 2015, doi: 10.1016/j.jpowsour.2014.11.010.

[69] T. A. Kozawa and J. F. Y. Kalnoki-Kis, "Solubilities of Mn(II) and Mn(III) ions in concentrated alkaline solutions," *J. Electrochem. Soc.*, pp. 405–409, 1966.

[70] D. Boden, C. J. Venuto, D. Wisler, and R. B. Wylie, "The Alkaline Manganese Dioxide Electrode," vol. 115, no. 4, pp. 4–9.

[71] C. Mondoloni, M. Laborde, J. Rioux, E. Andoni, and C. Lévy-Clément, "Rechargeable alkaline manganese dioxide batteries," *J. Electrochem. Soc.*, vol. 139, pp. 954–959, 1992.

[72] S. J. Wang *et al.*, "As featured in : rechargeable Zn-based aqueous battery †," *Phys. Chem. Chem. Phys.*, vol. 18, pp. 26376–26382, 2016, doi: 10.1039/c6cp04566a.

[73] S. Han *et al.*, "Mechanism of Zn Insertion into Nanostructured δ -MnO 2 : A Nonaqueous Rechargeable Zn Metal Battery."

[74] S. Brimaud, E. Marini, and J. Ludwig, "Rational design of a low-cost , durable and efficient bifunctional oxygen electrode for rechargeable metal-air batteries," vol. 482, no. August 2020, 2021, doi: 10.1016/j.jpowsour.2020.228900.